

**COBALT TRIS(2,2'-BIPYRIMIDINE) REDOX MEDIATORS
GENERATE HIGH DYE-SENSITIZED SOLAR CELL
PHOTOVOLTAGES**

by

Yingqian Kitty Chen

B.Sc. Chemistry (Honours), McGill University, 2015

A THESIS SUBMITTED IN PARTIAL FULFILLMENT OF THE
REQUIREMENTS FOR THE DEGREE OF

MASTER OF SCIENCE

in

THE FACULTY OF GRADUATE AND POSTDOCTORAL STUDIES

(Chemistry)

THE UNIVERSITY OF BRITISH COLUMBIA

(Vancouver)

December 2017

© Yingqian Kitty Chen, 2017

Abstract

Dye-sensitized solar cells (DSSCs) are promising, cost-effective technologies used to harness solar energy for electricity. Previous efforts to improve the solar-to-electricity conversion efficiency have primarily focused on sensitizer engineering and photocurrent generation. Alternatively, the efficiency can be increased by tuning the redox potential of the charge mediator to maximize the photovoltage in the device. This work describes the implementation of a new cobalt mediator (**Co-bpm**) with an exceptionally positively shifted redox potential of 1.07 V vs NHE in the DSSC. The best-performing device showed one of the highest reported DSSC photovoltages. The poor solubility of **Co-bpm** in MeCN was a major obstacle that was overcome by testing a variety of electrolyte solvent systems and counterions. Notwithstanding, **Co-bpm** mediator-based devices exhibited low photocurrents and low power conversion efficiencies despite the high voltages.

A comparative study was then performed to elucidate how the positively shifted redox potential affect the photocurrent in **Co-bpm** mediator-based devices. Three cobalt analogs [**Co-(bpm-DTB)**, **Co-bpy** and **Co-(bpy-DTB)**] of varying redox potentials were studied alongside **Co-bpm** to determine the trend between redox potential, device performance, and recombination lifetime. The redox potentials of the cobalt analogs were tuned by installing *tert*-butyl substituents and varying the number of nitrogen atoms in the ligand. A positive shift in the redox potentials correlated to a linear increase in photovoltage and non-linear decrease in photocurrent in DSSCs. A low quasi-Fermi level ($E_{F,n}$) at open-circuit conditions and a short electron lifetime (T_n) in device containing **Co-bpm** indicate that a significant loss of electrons from TiO_2 via recombination pathways is one key factor that contribute to the poor photocurrent and overall device performance.

Lay Summary

The objective of the thesis is to target record-breaking voltages in dye-sensitized solar cells (DSSCs). Solar cells with high voltages are capable of producing more electricity from less sunlight. DSSCs are a promising type of low-cost solar cells that uses molecules to convert sunlight into electricity. One way to boost the voltage is by modifying the properties of the mediator compound that is responsible for moving electrical charges inside the cell. I tested a new mediator compound with suitable properties and found that the measured voltages were comparable to some of the highest voltages reported in a DSSC. The efficiency of converting sunlight to electricity in the cell, however, was less than expected. The new mediator compound was then compared with commonly-used mediator compounds to find the cause of low electricity and identify ways to make better performing DSSCs in the future.

Preface

The work presented in the thesis was performed under the supervision of Dr. Curtis P. Berlinguette. I performed the synthesis and characterization of cobalt complexes, and most of the device fabrication and analysis in chapter 2 and 3. Chuan Du constructed and measured the performance of solar devices containing electrolytes of mixed solvent systems in chapter 2. X-ray diffraction measurements and analyses of **Co-bpm** and **Co-(bpm-DTB)** were performed by Dr. Brian Patrick at the X-ray crystallography facility at University of British Columbia. Part of chapter 2 regarding the performance of devices in different solvent systems is published (Chen, K. Y.; Du, C.; Patrick, B. O.; Berlinguette, C. P. *Inorg Chem.* **2017**, 56 (5), 2383). Chapter 3 and 4 are unpublished work.

Table of Contents

Abstract.....	ii
Preface.....	iv
Table of Contents	v
List of Tables	vii
List of Figures.....	viii
List of Schemes.....	x
List of Symbols and Abbreviations	xi
Acknowledgements	xiii
Dedication	xiv
Chapter 1. Introduction	1
1.1 Solar Cell Technology	1
1.2 The Dye-Sensitized Solar Cell	2
1.3 DSSC Photovoltage	4
1.4 Redox Mediators in the DSSC	6
1.5 Cobalt Redox Mediator	7
1.6 Choice of Dye	10
1.7 Device Characterization	11
1.7.1 Power Conversion Efficiency	11
1.7.2 Dark Current	12
1.7.3 Short-Circuit Photocurrent Transient.....	13
1.7.4 Open-Circuit Voltage Decay.....	13
1.8 Thesis Objective	15
Chapter 2. Cobalt Tris(2,2'-Bipyrimidine) Complex Yields a High Open-Circuit Voltage in the Dye-Sensitized Solar Cell	16
2.1. Introduction	16
2.2. Results and Discussion	17
2.2.1 Structural, Optical, and Electrochemical Characterization	17
2.2.2 First iteration of DSSCs Tested with Co-bpm	21
2.2.3 Improving Co-bpm Device Performance with Alternative Solvent Systems ..	23
2.2.4 Improving Co-bpm Device Performance by Changing the Counterion	26
2.2.5 Discussion of the “S-shape” J-V Curve	28

2.3 Conclusion	29
Chapter 3. Elucidating the Role of Cobalt Electrolyte Redox Potential on the Performance of Dye-Sensitized Solar Cells.....	30
3.1. Introduction	30
3.2. Results and Discussion	32
3.2.1 Comparing the Properties of Co-bpy, Co-bpm, Co-(bpy-DTB), and Co-(bpm-DTB)	32
3.2.2 Redox Potential and Device Performance	37
3.2.3 Redox Potential and Electron Recombination	40
3.3 Conclusion	43
Chapter 4. Conclusion and Future Directions	45
4.1. Conclusion	45
4.2. Future Directions	45
Chapter 5. Experimental.....	48
References.....	61
Appendix.....	66

List of Tables

Table 2.1. Preliminary Device Performances of Co-bpm in MeCN.	22
Table 2.2. Device Performances of Co-bpm in 1:1 DMSO/MeCN.	25
Table 2.3. Saturation Concentration of [Co-bpm](X)₂ in MeCN.	27
Table 2.4. Device Performances of [Co-bpm](PF₆) and [Co-bpm](TFSI) with Various Electrolyte Formulation.	28
Table 3.1. Bond Lengths and Angles of Co-bpy , Co-bpm , Co-(bpy-DTB) , and Co-(bpm-DTB)	33
Table 3.2. Effective Magnetic Moments (U_{eff}), Redox Potentials (E^0), and Diffusion Coefficients (D_{bulk}) of Co(II) Species Measured in MeCN.	34
Table 3.3. Average Device Performance of Co-(bpy-DTB) , Co-bpy , Co-(bpm-DTB) , and Co-bpm in DSSC.	39
Table A.1. Crystallographic Data for [Co-bpm](PF₆)₂	66
Table A.2. Selected Bond Lengths [\AA] and Angles [$^\circ$] for [Co-bpm](PF₆)₂	67
Table A.3. Crystallographic Data for [Co-(bpm-DTB)](PF₆)₂	68
Table A.4. Selected Bond Lengths [\AA] and Angles [$^\circ$] for [Co-(bpm-DTB)](PF₆)₂	69
Table A.5. UV-vis Absorption of Co-bpy , Co-bpm , Co-(bpy-DTB) , and Co-(bpm-DTB) in MeCN.	70
Table A.6. Approximated Saturation Concentration of [Co-bpm](PF₆)₂ in Different Solvents.	71
Table A.7. DSSC Data at Different Co^{II}-bpm Concentrations and in Different Solvents.	74

List of Figures

Figure 1.1. (a) Structure of a dye-sensitized solar cell and (b) the energy diagram of the components in a functional DSSC.	4
Figure 1.2. Chemical structure of Dye-I	10
Figure 1.3. Current density-voltage curve (red) and corresponding power-voltage curve (blue) of a solar cell.	12
Figure 1.4. (a) Simulated OCVD curve and (b) the corresponding electron lifetime (T_n) vs $E_{F,n}$ curve.	14
Figure 2.1. Chemical structure of Co-bpm . $Z = +2$ or $+3$	17
Figure 2.2. Thermal ellipsoid plot of Co-bpm drawn at the 50% probability level.	18
Figure 2.3. ^1H NMR in CD_3CN of bpm ligand in (a) free solution, (b) Co^{II}-bpm and (c) Co^{III}-bpm	18
Figure 2.4. UV-Vis spectrum of Co-bpm in MeCN.	19
Figure 2.5. Cyclic voltammogram of Co-bpm in MeCN.	20
Figure 2.6. J-V curve of Co-bpm in MeCN with (solid line) and without (dash line) TBP.	22
Figure 2.7. PCE of cells at different Co-bpm concentrations and in different electrolyte solvents	24
Figure 2.8. J-V curve of devices employing Co-bpm in 1:1 DMSO/MeCN with different electrolyte formulation.	25
Figure 2.9. ^1H NMR of Co^{II}-bpm in (a) CD_3CN and (b) DMSO- d_6	26
Figure 2.10. J-V curves of devices containing [Co-bpm](TFSI) electrolytes presented in Table 2.4.	28
Figure 3.1. Chemical structure of the Co-bpm , Co-bpy , Co-(bpm-DTB) , and Co-(bpy-DTB)	31
Figure 3.2. Redox potential diagram of the four redox mediators, ground-state and excited-state level of dye, conduction band level (E_C), and the quasi-Fermi level of TiO_2 ($E_{F,n}$)..	32
Figure 3.3. UV-vis of Co-bpy (grey), Co-bpm (orange), Co-(bpy-DTB) (blue) and Co-(bpm-DTB) (red).	35
Figure 3.4. Cyclic voltammograms of Co-(bpy-DTB) (blue), Co-bpy (grey), Co-(bpm-DTB) (red), and Co-bpm (orange) in 0.1 M NBu_4PF_6 in MeCN.	36

Figure 3.5. Cyclic voltammogram of Co-bpy (grey), Co-bpm (orange), Co-(bpy-DTB) (blue), and Co-(bpm-DTB) (red) with platinum (Pt), glassy carbon (GC), and gold (Au) working electrodes.	37
Figure 3.6. Plots of PCE, J_{SC} , and V_{OC} vs. E^0 of Co-(bpy-DTB) (blue), Co-bpy (grey), Co-(bpm-DTB) (red), and Co-bpm (orange).	38
Figure 3.7. SCPT of best performing cell devices with cobalt mediator Co-(bpy-DTB) (blue), Co-bpy (grey), Co-(bpm-DTB) (red), and Co-bpm (orange).	40
Figure 3.8. Dark J-V curve of best performing cell devices with cobalt mediator Co-bpm (orange), Co-(bpm-DTB) (red), Co-bpy (grey), and Co-(bpy-DTB) (blue).	41
Figure 3.9. Electron lifetime (T_n) vs. quasi-Fermi level ($E_{F,n}$) graph derived from OCVD of the best performing cell devices with cobalt mediator Co-bpm (orange), Co-(bpm-DTB) (red), Co-bpy (grey), and Co-(bpy-DTB) (blue).	42
Figure 3.10. (a) OCVD recombination model showing electron recombination pathway from the surface states (blue) and trap states (grey) in TiO_2 and (b) a simulated semi-logarithmic electron lifetime (T_n) vs quasi-Fermi Level ($E_{F,n}$).	43
Figure 4.1 Common cobalt dopants in solid-state solar cells and the corresponding E^0	47
Figure 5.1. Rotating disk electrode submerged in electrolyte containing redox active species.	58
Figure A.1. Thermal ellipsoid plot of Co-(bpm-DTB) drawn at the 50% probability level.....	68
Figure A.2 1H NMR spectra of (a) [Co-bpy](PF ₆) ₂ , (b) [Co-bpm](PF ₆) ₂ , (c) [Co-(bpy-DTB)](PF ₆) ₂ , and (d) [Co-(bpm-DTB)](PF ₆) ₂	70
Figure A.3. Koutecky-Levich plot of Co-bpy and Co-bpm with insets showing the linear sweep voltammetry (LSV) traces.	72
Figure A.4. (top) Koutecky-Levich plot and (bottom) linear sweep voltammetry traces of Co-(bpy-DTB) , Co-bpy , and Fc.	73
Figure A.5. J-V curve of best performing cell devices with cobalt mediator (Co-bpy-DTB) (blue), Co-bpy (grey), Co-bpm-DTB (red), and Co-bpm (orange).	74
Figure A.6. OCVD decay curve measured in devices containing Co-bpm (orange), Co-bpy (grey), Co-(bpm-DTB) (red) and Co-(bpy-DTB) (blue).	75

List of Schemes

Scheme 5.1. Synthesis of 2-chloro-4- <i>tert</i> -butyl-pyrimidine.....	49
Scheme 5.2. Synthesis of 4,4'-di- <i>tert</i> -butyl-2,2'-bipyrimidine.....	50
Scheme 5.3. Synthetic route of [Co- L](PF ₆) ₂ (L = coordinating diimine ligand).....	51

List of Symbols and Abbreviations

<u>Symbols</u>	<u>Definitions</u>
Å	angstrom
Ag/AgCl	silver/silver chloride
Au	gold
bpm	2,2'-bipyrimidine
bpy	2,2'-bipyridine
°C	degree Celcius
CD ₃ CN	deuterated acetonitrile
CE	counter electrode
Co-bpy	cobalt tris(2,2'-bipyridine)
Co-bpm	cobalt tris(2,2'-bipyrimidine)
Co-(bpy-DTB)	cobalt tris(4,4'-di- <i>tert</i> -butyl-2,2'-bipyridine)
Co-(bpm-DTB)	cobalt tris(4,4'-di- <i>tert</i> -butyl-2,2'-bipyrimidine)
Co(II)	cobalt (II) species
Co(III)	cobalt (III) species
Conc.	concentration
CV	cyclic voltammetry
D	ground-state level of dye
D*	excited-state level of dye
D_{bulk}	diffusion coefficient in bulk solution
DMSO- d6	deuterated dimethyl sulfoxide
ε	molar extinction coefficient
Eq.	equation
$\Delta G^{\circ}_{\text{rec}}$	Gibbs free energy of recombination
$\Delta G^{\circ}_{\text{reg}}$	Gibbs free energy of dye regeneration
DMSO	dimethyl sulfoxide
DSSC	dye-sensitized solar cell
E_{C}	conduction band edge
$E_{\text{F,n}}$	quasi-Fermi level
E°	redox potential of mediator
EC	ethylene carbonate
FF	fill factor
FTO	fluorine-doped tin oxide
g-BL	gamma-butyrolactone
GC	glassy carbon
λ	reorganization energy
LSV-RDE	linear sweep voltammetry - rotating disk electrode
J-V	current density-voltage
J_{max}	photocurrent at maximum power
J_{SC}	short-circuit current density
k_{b}	Boltzmann constant
MeCN	acetonitrile
NBu ₄ PF ₆	tetra- <i>n</i> -butylammonium hexafluorophosphate
NHE	normal hydrogen electrode

OCVD	open-circuit voltage decay
PCE	power conversion efficiency
ϕ	bond angle of the same ligand
P_{ideal}	ideal maximum power output
P_{max}	measured maximum power output
Pt	platinum
PV	photovoltaic
RE	reference electrode
SCPT	short-circuit photocurrent transient
T	temperature
TBP	<i>tert</i> -butyl pyridine
θ	bond angle between adjacent ligands
TiO ₂	titanium dioxide
T_n	electron lifetime
TW	terawatt
V	volts
V_{max}	voltage at maximum power
V_{OC}	open-circuit voltage
U_{eff}	effective magnetic susceptibility
λ_{max}	maximum wavelength
WE	working electrode
XRD	X-ray diffraction

Acknowledgements

I want to express my gratitude to Dr. Curtis P. Berlinguette for the opportunity to work and learn in an engaging environment. Your enthusiasm and support facilitated the publication of my work and the completion of this thesis.

I would also like to thank the Berlinguette group members for their constant support. I would especially like to thank Cameron Kellett and Dr. Yang Cao for the numerous hours you have taken out of your own time to guide and discuss chemistry-related (and sometimes unrelated) concepts with me. I also want to acknowledge Valerie Chiykowski for being a fantastic desk buddy, Rebecka Forward for keeping me company during long days of device fabrication, and Alicia Koo and Paloma Prieto for encouraging me to never give up.

I want to thank my family and friends for their continual love and support.

Dedicated to my family.

奉献给我的家人

Chapter 1. Introduction

1.1 Solar Cell Technology

Energy demand is expected to rise substantially in both developing and developed nations due to population growth and higher standards of living. The rate of global energy consumption in 2014 was 12.5 TW¹, a value that is projected to increase to 27.3 TW by 2040.² Renewable energy is becoming a greater part of the electricity supply as the cost of renewable technologies continues to decrease. Energy can be collected from biomass (combustion), water (hydroelectric turbines), wind (turbines), heat beneath the earth (geothermal reservoir), and sunlight (solar photovoltaics). Among all the renewable options, the greatest expansion has been observed for photovoltaics (PV), which have reached an average annual growth of 45.5%.³ The increase in PV global capacity from 2015 to 2016 is equivalent to installing more than 31,000 new solar panels every hour.⁴

Solar PV receives considerable attention for several reasons. First, solar energy is capable of meeting global energy demand if it is collected efficiently. Installing 10% efficiency solar cells over 0.16% of earth's land area is enough to fulfill the energy demand predicted for 2040.⁵ In addition, the price of solar technology is decreasing rapidly. The average cost of solar PV has fallen by more than 80% since 2006.^{6,7} Moreover, solar energy is available anywhere on earth. In comparison, utilization of wind, geothermal, and hydroelectric technologies is limited by the geographical location of the resources.⁸

Solar energy is converted into electrical energy by the PV effect, a phenomenon first observed in an electrolytic cell experiment conducted by A. E. Becquerel in 1839.⁹ The process is initiated when the absorption of photons stimulates electron excitation and leave behind positive holes in a semiconducting material. A voltage difference formed across the cell prompts the movement of charge carriers and generates electrical current.

Solar cells are separated into three categories depending on the type of photoactive material. Crystalline silicon wafers^{10,11} are used in first-generation cells while thin films of amorphous silicon,^{12,13} cadmium telluride,¹⁴ and copper indium gallium sulfide^{15,16} are employed in second-generation solar cells. They operate on the principle of the p-n junction formed by stacking positively-doped (p-type) and negatively-doped (n-type) semiconducting materials together. The high cost and complexity in processing uniform semiconducting materials hinder widespread employment of first- and second-generation technologies. In third-generation solar cells, less expensive photoactive materials including perovskites¹⁷, quantum dots¹⁸, organic molecules¹⁹, and polymers²⁰ are utilized. These solar cells can be manufactured in a less rigorous environment and require less photoactive material to function efficiently. Dye-sensitized solar cells (DSSC) is categorized as a third-generation solar cells.²¹

1.2 The Dye-Sensitized Solar Cell

Grätzel and O'Brien reported the first DSSC in 1991.²² Prior to this seminal paper that used a mesoporous film of nanoparticles, dye-sensitized electrodes performed very poorly in photochemical cells due to the use of planar electrodes.²³⁻²⁵ The DSSC field expanded quickly over the next three decades with over 17,000 articles published in the area as of 2017 (Web of Science database). Much of the research has focused on optimizing the dye,²⁶ mediator,²⁷ and counter electrode.²⁸

The structure of a conventional DSSC is presented in Figure 1.1a. The anode of the cell is a mesoporous layer of semiconducting metal oxide nanoparticles sensitized with molecular dyes deposited on a transparent fluorine-doped tin oxide (FTO) glass. The semiconductor is often anatase titanium dioxide (TiO₂) because it is stable and has an appropriate band gap.²⁹ The cathode is a transparent FTO glass coated with a material (e.g. platinum) to catalyze charge transfer with the electrolyte. The electrodes are separated by several microns using a thermoplastic spacer. An

electrolyte solution containing a redox mediating species is injected between the electrodes to close the electrical circuit.

The DSSC reactions are described in Figure 1.1b. Upon absorption of solar energy, an electron in the dye is excited and injected into the conduction band (E_C) of TiO_2 . The resultant oxidized dye molecule is reduced by the redox mediator in the electrolyte (“dye regeneration”). The injected electron diffuses through the nanoparticle TiO_2 film, travels through an external circuit to the cathode and produces electrical current. The electron then reduces the oxidized form of the redox mediator to close the circuit. An effective DSSC must have the following properties: 1) the dye must absorb visible light (300-800 nm) effectively; 2) the excited-state level of the dye (D^*) lies above the conduction band level (E_C) of TiO_2 ; and 3) the ground-state level of the dye (D) must reside lower than the redox potential of the redox mediator (E^0) to accommodate regeneration of the oxidized dyes.

There are several competitive electron transfer pathways that negatively affect device performance. For instance, photo-injected electrons can directly reduce the oxidized dye (“back-electron transfer”) or oxidized redox mediator (“recombination”). Solar cell parameters such as photocurrent and photovoltage are dictated by the relative rates of dye regeneration, back-electron transfer, and recombination processes.³⁰

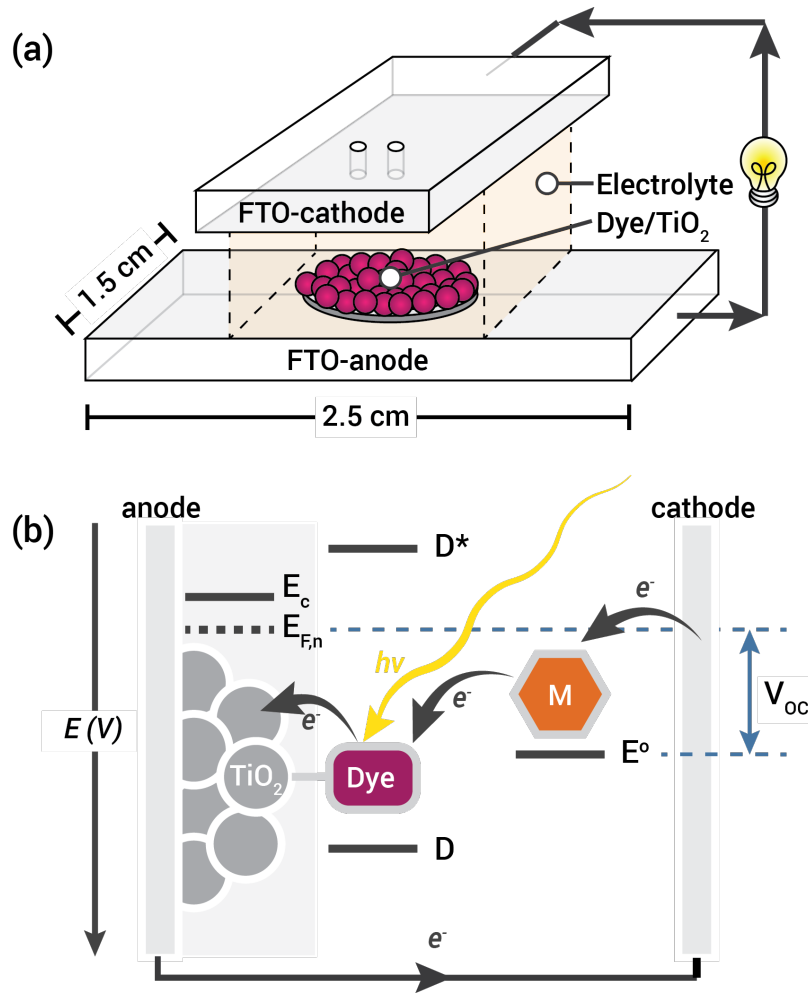


Figure 1.1. (a) Structure of a dye-sensitized solar cell and (b) the energy diagram of the components in a functional DSSC. E_c is the conduction band level and $E_{F,n}$ is quasi-Fermi level of TiO₂. D and D^* are the ground-state and the excited-state level of dye, respectively. E^o is the redox potential of the mediator and V_{oc} is the open-circuit voltage. The black arrows indicate the desired direction of electron transfer under operating conditions.

1.3 DSSC Photovoltage

Photovoltage is defined as the light-induced electric potential between two points in space per unit charge and indicates the maximum potential energy that can be converted into electrical energy per electron across the DSSC device. The maximum photovoltage is measured at open-circuit when the net current in the device is zero, and it is known as the open-circuit voltage (V_{oc}). V_{oc} is determined by the difference in the Fermi levels of the anode and cathode, which are governed by $E_{F,n}$ and the E^o , respectively (Figure 1.1b, Eq. 1.1).³¹

$$V_{OC} = E^o - E_{F,n} \quad (1.1)$$

$E_{F,n}$ is a term that describes of density of electrons in TiO_2 under a given equilibrium condition.³² It is maintained at a steady level when electrons are injected at the same rate as the movement of electrons to the external circuit. Any electron transfer pathways that add electrons to or remove electrons from the TiO_2 cause fluctuation in $E_{F,n}$ and consequently the V_{OC} .³³ Deleterious electron transfer processes such as back-electron transfer and recombination are responsible for the positive (downward) shift in $E_{F,n}$ and decrease in V_{OC} in the DSSC.³⁴ A shorter electron lifetime in the TiO_2 film reflects a significant loss of electrons through these processes.^{35–}
³⁷ Slow dye regeneration further promotes back-electron transfer because more oxidized dyes are readily available to accept electrons from TiO_2 .³⁸

E^o is a measure of the tendency for a redox mediator to lose or gain an electron. V_{OC} is anticipated to increase when E^o is positive (downward) shifted and all other parameters are held at parity (Figure 1.1b). The trend is experimentally observed for various types of redox mediators.^{39–42} It is important to note that photovoltage may be lost depending on the value of E^o due to slower dye regeneration and faster recombination kinetics. Dye regeneration is slower as E^o shifts positively because the energy difference between the ground state level of the dye and E^o is decreased.⁴³ A smaller energy difference represents less Gibbs free energy for dye regeneration (ΔG^o_{reg}) and a slower rate constant due to a lower driving force for the reaction.⁴⁴ Recombination is typically accelerated at positively shifted E^o because the Gibbs free energy for recombination (ΔG^o_{rec}) increases with greater difference between the E_C of TiO_2 and E^o . The trend between the driving force and E^o is less clear when E^o is shifted to highly positive value.⁴⁵ Nonetheless, the most direct method to enhance the photovoltage and possibly the overall performance of the DSSC is to maximize the E^o . Therefore, the motivation for this study is to utilize a new, highly positive E^o redox mediator to push the limit of photovoltage.

1.4 Redox Mediators in the DSSC

The redox mediator is vital to the shuttling of electrons between the electrodes. In the conventional DSSC, the reduced and oxidized forms of the mediator are dissolved in an electrolyte solution consisting of a solvent and additives. A good redox mediator should be stable and unreactive with other cell components, regenerate oxidized dyes, and cycle between the oxidized and reduced forms efficiently.^{27,30} Organic mediators are small molecules that can be acquired from common reagents in the form of sodium and potassium salts while inorganic mediators are more tunable but require one or more steps to synthesize.

The mediator used in the seminal Grätzel paper was based on the iodide/triiodide (I^-/I_3^-).²² The advantages of an I^-/I_3^- redox shuttle are fast diffusion rates, low cost, and high solubility. Importantly, recombination is low because of a higher energy barrier for the reverse two-electron reduction of I_3^- to I^- . The disadvantages are that iodide corrodes the conductive silver contact in the device, competes with photon absorption by the dye, and reacts to form iodine during electron transfer that then evaporate from the electrolyte. Furthermore, V_{OC} is capped at 0.8 V because the E° of I^-/I_3^- couple is 0.3 V vs NHE⁴⁶ and the conduction band level of TiO_2 is at -0.5 V vs NHE.¹⁸ This V_{OC} limit was experimentally observed in high efficiency iodide electrolyte-based devices.^{47,48} Other organic redox mediators have also been investigated,^{27,49,50} but the drawback remains that E° is fixed to a specific value.

Inorganic metal-based mediators such as ferrocene/ferrocenium,⁵¹ $Ni(III)/Ni(IV)$,⁵² $Cu(I)/Cu(II)$,⁵³ and $Co(II)/Co(III)$ ⁵⁴ couples have demonstrated equal or better performance in the DSSC than the organic mediators. The highest recorded efficiencies are held by $Co(II)/Co(III)$ mediator at 14.3%⁵⁴ under solar irradiation and $Cu(I)/Cu(II)$ mediator at 28.9%⁵⁵ under ambient fluorescent light. These metal complexes typically have low molar absorptivities which minimize competitive light absorption with the dyes. The most appealing feature of inorganic redox mediators is that the E° can be altered based on the structure, coordination geometry, and electron-

withdrawing or -donating ability of the ligand.⁴⁵ One notable problem is that inorganic redox couples undergo one-electron transfer, which proceeds faster than two-electron transfer. Dye regeneration by reduced mediator species occurs quickly, but recombination with oxidized mediators is also accelerated up to 2-3 orders of magnitude faster than I^-/I_3^- .⁵⁶

1.5 Cobalt Redox Mediator

The most attractive inorganic mediator is Co(III)/Co(II) redox couple because recombination proceeds much slower than what is expected in a one-electron transfer. This feature is attributed to the fact that octahedral Co(II) and Co(III) species have different ground-state electron configurations in the *d*-orbitals. The spin change between high and low Co(II) spin states creates an energy barrier to slow down recombination while retaining efficient dye regeneration.⁵⁷

Many types of ligands are available in coordination chemistry, but very few can form energetically suitable cobalt complexes for the DSSC. It is highly desirable that E^0 matches closely to the redox potential of ground state dye (~ 0.9 - 1.3 V vs NHE⁵⁸) to maximize V_{OC} . Polypyridine ligands have shown great versatility and success because E^0 of polypyridyl cobalt complexes typically lie between 0.3 to 1.0 V vs NHE.⁴⁵ In addition, polydentate ligands are preferred because metal-ligand bonds in first-row transition metal complexes are labile. Mediators formed with chelating ligands have greater thermodynamic stability and can be used to produce more durable devices.^{59,60} Chart 1.1 summarizes previously reported bidentate,⁶¹⁻⁶⁶ tridentate,^{57,67-71} tetradentate,⁷² pentadentate,⁷³ and hexadentate^{59,60} ligand-based cobalt mediators in the DSSC.

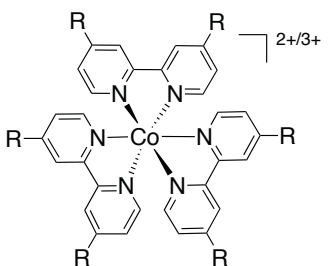
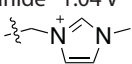
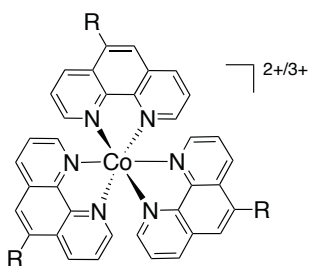
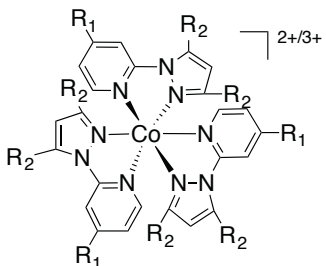
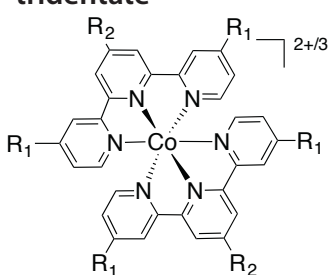
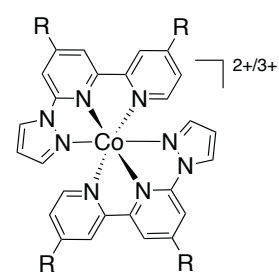
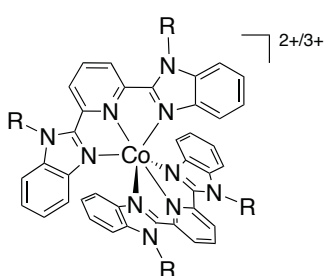
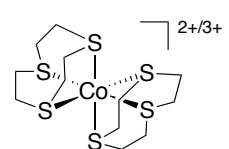
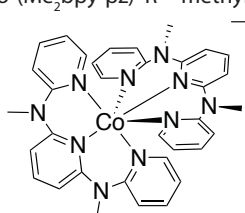
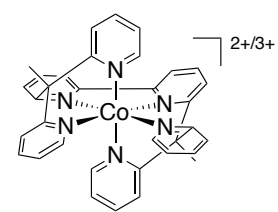
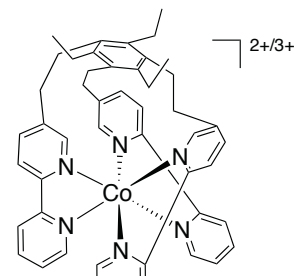
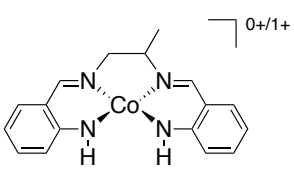
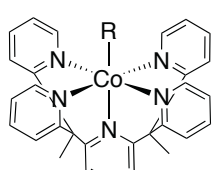
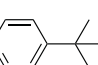
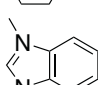
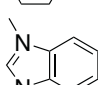
<div>  <p>Co-bpy R = H 0.56 V Co-(bpy-DM) R = methyl 0.42 V Co-(bpy-DTB) R = tert-butyl 0.42 V Co-(OMe₂-bpy) R = methoxy 0.37 V Co-(Cl₂bpy) R = Cl 0.81 V Co-(CN-bpy) R = cyanide 1.04 V Co-(OMe-bpy) R =  0.52 V</p> </div>		
<div>  <p>Co-phen R = H 0.61 V Co-(Me-phen) R = methyl 0.57 V Co-(Cl-phen) R = Cl 0.72 V Co-(NO₂-phen) R = NO₂ 0.85 V</p> </div>		
<div>  <p>Co-(py-pz) R₁ = R₂ = H 0.96 V Co-(Mepy-pz) R₁ = methyl, R₂ = H 0.92 V Co-(py-Me₂pz) R₁ = H, R₂ = methyl 0.98 V</p> </div>		
<div> <p>bidentate</p> </div>		
<div>  <p>Co-tpy R₁ = R₂ = H 0.51 V Co-(Cl-tpy) R₁ = H, R₂ = Cl 0.63 V Co-(Clphen-tpy) R₁ = H, R₂ = Cl-phen 0.47 V</p> </div>		
<div>  <p>Co-(bpy-pz) R = H 0.86 V Co-(Me₂bpy-pz) R = methyl 0.76 V</p> </div>		
<div>  <p>Co-dmbip R = methyl 0.65 V Co-dbbip R = butyl 0.59 V</p> </div>		
<div>  <p>Co-ttcn 0.69 V</p> </div>		
<div>  <p>Co-ddpd 0.47 V</p> </div>		
<div> <p>hexadentate</p>  <p>Co-bpyPY4 0.47 V</p>  <p>Co-ttb 0.47 V</p> </div>		
<div> <p>tetradentate</p>  <p>Co-abpn 0.41 V</p> </div>		
<div> <p>pentadentate</p>  <p>Co-(PY5Me₂)(TBP) R =  0.78 V</p>  <p>Co-(PY5Me₂)(NMBI) R =  0.71 V</p> </div>		

Chart 1.1. Chemical structures, abbreviated names, and E^0 's (V vs NHE) of previously studied cobalt mediators organized by ligand denticity and type. Bolded texts highlight the complex structure with no substituent for each type of ligand.

Nusbaumer *et al.* reported the first successful cobalt mediator **Co-dbbip** that displayed comparable dye regeneration kinetics to the iodide mediator in 2001.⁶⁷ In the following year, Sapp *et al.* found that devices containing **Co-(bpy-DTB)** showed the best efficiency of 1.3% among the fourteen surveyed cobalt complexes.⁶¹ Nonetheless, the performances of devices containing cobalt electrolyte were worse than those containing iodide electrolyte when champion ruthenium dyes were employed.^{61,74,75} Feldt *et al.* was able to demonstrate that a cobalt mediator-based device could outperform an iodide mediator-based device by using an organic dye.⁷⁶ Yella *et al.* reached 11% efficiency using **Co-bpy** and a porphyrin dye,⁷⁷ and later reported 13% efficiency with an optimized panchromatic dye.⁷⁸ Kakiage *et al.* recently achieved a record-breaking 14.3% efficiency with **Co-phen** and co-sensitized organic dyes.⁵⁴

The success of cobalt electrolytes in the DSSC is mainly due to high photovoltages because the V_{OC} of DSSCs using cobalt electrolytes are consistently higher than those using iodide electrolytes under similar cell conditions.^{54,79–81} In fact, the majority of high photovoltage DSSCs (i.e. $V_{OC} > 1$ V) reported in literature are based on cobalt mediators.^{43,63,82} The highest V_{OC} achieved in the cobalt electrolyte-based DSSC is 1.1 V using **Co-(bpy-pz)**.⁸³

The first step toward surpassing the previous photovoltage record is to design a new cobalt mediator. Three important properties are considered when designing a new mediator: E^0 ; the size of the complex; and the spin state of Co(II) and Co(III). These properties influence the rate of recombination and consequently the photovoltage in the DSSC. It is clear that a highly positive E^0 is advantageous for high photovoltage generation based on the definition of V_{OC} (Eq. 1.1). It is also preferable to design small mediators since the diffusion of a molecule is size-dependent.^{43,57,76,84} A slower diffusion rate can result in the accumulation of Co(III) species near TiO_2 under operating conditions. This high local concentration of Co(III) increases the probability of recombination and lead to lower V_{OC} .⁸⁵ A cobalt redox couple with different Co(II) and Co(III) spin states is able to better suppress recombination and boost V_{OC} .^{69,86,87} The origin of the

difference is attributed to a higher reorganization energy (λ) needed to relocate electrons in a low-spin Co(II) species to high-spin configuration in a process known as spin crossover.⁸⁸ Reorganization energy describes the total energy expended to change the geometry of a molecule (inner λ) and to arrange the nearby solvent molecules (outer λ) before and after electron transfer according to Marcus theory.⁸⁹ In summary, the desired mediator traits to produce high photovoltage DSSCs are high E° , small size, and dissimilar Co(II) and Co(III) spin states.

1.6 Choice of Dye

Dye design is an active area of research in the DSSC field. Many strategies have been developed to extend the range of light absorption and maintaining adequate driving force for dye regeneration.^{90,91} In this study, an organic triphenylamine-based dye known as **Dye-I** was chosen, the structure of which is shown in Figure 1.2. The primary reason for this choice is that the redox potential of the ground-state dye at 1.27 V vs NHE is suited to accommodate dye regeneration by cobalt redox mediators with highly positive E° .⁹² In addition, **Dye-I** is readily available in the Berlinguette lab and has been previously reported to function well in cobalt electrolyte-based DSSCs.

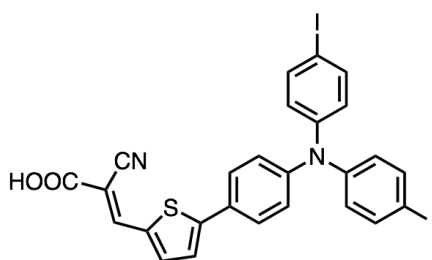


Figure 1.2. Chemical structure of **Dye-I**.

1.7 Device Characterization

1.7.1 Power Conversion Efficiency

The key figure of merit is the power conversion efficiency (PCE). PCE is the percent of solar energy that is converted into electrical energy. It is obtained from the current density-voltage (J-V) curve shown in Figure 1.3. The J-V curve of a photovoltaic device is typically collected under AM 1.5 irradiation where the input power (P_{in}) is 1000 W/m^2 . This input power is denoted as 1 sun irradiation. For low-intensity irradiation measurements in this study, the input power is approximately 700 W/m^2 , or 0.7 sun.

PCE is proportional to short-circuit current density (J_{sc}), open-circuit voltage (V_{oc}), and fill factor (FF) (Eq. 1.2). V_{oc} is described in section 1.3. J_{sc} is the maximum current density measured across the device when the voltage is zero. FF represents the ratio of the maximum measured power output (P_{max}) to the ideal maximum power output (P_{ideal}) (Figure 1.3). Deviation from the ideal J-V curve shape is caused by series and shunt resistance from undesirable recombination pathways, contact resistance, and defects in the device.²¹ Series resistance is the loss of energy through resistive elements along the favored electron transport pathway such as diffusion resistance in electrolyte, charge-transfer resistance during dye regeneration, and heterogeneous electron transfer resistance at the cathode. On the other hand, shunt resistance is affected by parallel pathways from which electrons can be lost such as low recombination resistance at the anode. Ideally, FF reaches unity when shunt resistance is infinite and series resistance is zero.

$$PCE = \frac{V_{oc} \times J_{sc} \times FF}{P_{in}} \quad (1.2)$$

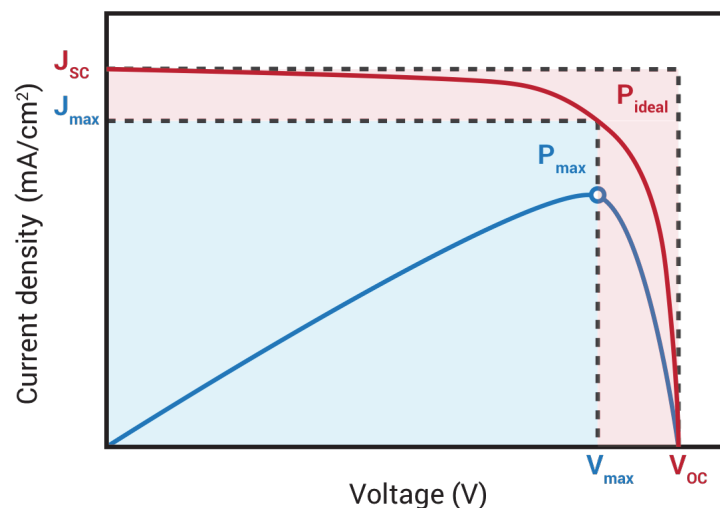


Figure 1.3. Current density-voltage curve (red) and corresponding power-voltage curve (blue) of a solar cell. V_{\max} and J_{\max} are voltage and current density associated with P_{\max} , the maximum power generated in the cell. V_{oc} and J_{sc} , and P_{ideal} are open-circuit voltage, short-circuit current density, and ideal maximum power output, respectively. The ratio of P_{\max} (blue area) to P_{ideal} (blue and red area) is the fill factor.

1.7.2 Dark Current

Dark current measurement is a measure of the current generated when a positive voltage bias is applied to an anode relative to cathode in the dark. Current flows in the reverse direction of the current under illuminated condition and is represented as a negative value. The electrochemically generated electrons in the FTO anode at positive voltage bias can either undergo direct recombination at exposed surfaces in contact with oxidized mediator species or populate the TiO_2 and recombine from the TiO_2 surface.⁹³ The former pathway is negligible because the exposed FTO surface is passivated by TiO_2 . $E_{\text{F,n}}$ shifts upward (more negatively in voltage) as electrons populate the unfilled states in TiO_2 . When $E_{\text{F,n}}$ is sufficiently negative, fast reduction of oxidized Co(III) species at the TiO_2 /electrolyte interface yields substantial dark current. The onset voltage and dark current value reveal the resistivity toward recombination at a given applied bias.

1.7.3 Short-Circuit Photocurrent Transient

Short-circuit photocurrent transient (SCPT) is a qualitative method used to detect the impact of the mediator diffusion on the photocurrent in the DSSC.^{74,76,84,94,95} J_{SC} is monitored versus time at set intervals of on-off irradiation. If diffusion limits current flow in the circuit, a spike in J_{SC} is observed, followed by decay to a steady value under irradiation.⁸⁴ This effect is explained by a change in concentration of the reduced mediator species near the dye. Initially, a large photocurrent is measured because photo-oxidized dyes are regenerated quickly by a high concentration of reduced mediators near the anode. Over time, reduced mediator species are not sufficiently replenished near the dye due to slow mediator diffusion and photo-oxidized dyes cannot regenerate as efficiently. Consequently, diffusion limitation is most evident in devices under high-intensity light, but negligible under low-intensity light because less photo-oxidized dyes are generated. Therefore, low-intensity SCPT measurements are taken to compare the photocurrents of different devices in the absence of diffusion limitation.

1.7.4 Open-Circuit Voltage Decay

Open-circuit voltage decay (OCVD) is a fast and simple technique used to examine photo-injected electron recombination with mediator in the electrolyte. The device is placed under light for several seconds prior to turning off the light source. Throughout the process, V_{OC} decay is monitored at open-circuit conditions. A faster decay is related to greater degree of electron recombination. Back-electron transfer process occurs in a microsecond timescale and is not detected because OCVD is measured on a millisecond to second timescale.⁹³

OCVD curves are difficult to compare because decay slopes are steep and often do not decay to zero (Figure 1.4a). Bisquert *et al.* derived the lifetime of electrons in TiO_2 (T_n) as a function of the reciprocal of the first derivative of V_{OC} to provide meaningful interpretation of OCVD curves. (Eq. 1.3).^{32,96} k_b is Boltzmann constant, T is temperature, e is elementary charge, and t is time. Qualitative recombination trends in different devices are observed by plotting the

curves of T_n versus $E_{F,n}$ (Figure 1.4b) and comparing the magnitude of T_n . A larger T_n value at a given $E_{F,n}$ indicates slower recombination. $E_{F,n}$ is obtained by rearranging Eq. 1.1 to form Eq. 1.4.

$$T_n = -\frac{k_b T}{e} \left(\frac{dV_{OC}}{dt} \right)^{-1} \quad (1.3)$$

$$E_{F,n} = E^o - V_{OC} \quad (1.4)$$

A typical electron lifetime plot contains three regions associated with different channels of recombination (Figure 1.4b).³² In region 1, recombination of free electrons in the conduction band of TiO₂ to the redox mediator dominates and T_n is independent of $E_{F,n}$. This region is not observed under illumination and indicates that this recombination pathway is negligible in the DSSC. At intermediate $E_{F,n}$, electrons occupy the trap states below the conduction band. Additional energy and time are required to promote electrons into the conduction band for recombination. This process is reflected in region 2 where T_n increases exponentially with respect to $E_{F,n}$. At low $E_{F,n}$, electrons not only recombine through the conduction band, but also occupy the surface states of TiO₂ and undergo direct electron transfer with the oxidized mediator species. A parabolic curve in region 3 of the logarithmic T_n versus $E_{F,n}$ plot reveals that surface-state recombination is dominant. Region 2 and 3 are of interest in the analysis of recombination processes for different cobalt mediators presented in this thesis.

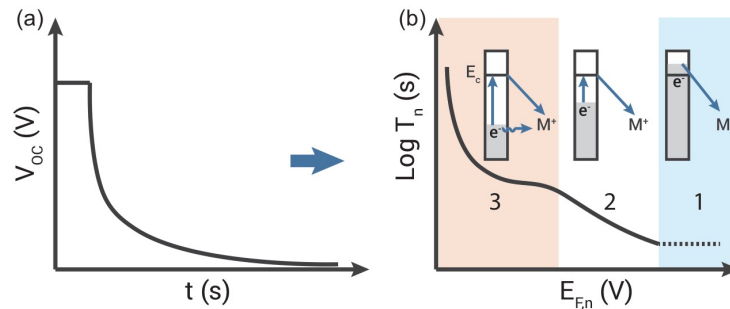


Figure 1.4. (a) Simulated OCVD curve and (b) the corresponding electron lifetime (T_n) vs $E_{F,n}$ curve. The three regions represent 1) recombination of free electrons in conduction band, 2) detrapping of electrons below conduction band followed by conduction band electron recombination, and 3) a combination of conduction band and surface-state recombination. M^+ is the oxidized mediator species.

1.8 Thesis Objective

The objective of the study is to introduce a new high E° cobalt mediator, cobalt tris(2,2'-bipyrimidine) (**Co-bpm**), to improve V_{OC} and cell efficiency in the DSSC. **Co-bpm** is regarded as a promising candidate because it is small and can achieve fast diffusion. Very high V_{OC} values are anticipated in devices using **Co-bpm** because the complex is characterized by an E° of over 1 V vs NHE.⁹⁵ The aim of chapter 2 is to establish that **Co-bpm** can indeed mediate charge in the DSSC and produce high photovoltages.

In chapter 3, the device performance of **Co-bpm** was compared to the analog cobalt tris(2,2'-bipyridine) (**Co-bpy**) to investigate the role of E° on photocurrent and electron recombination. A second bipyrimidine-based mediator, cobalt tris(4,4'-di-*tert*-butyl-2,2'-bipyrimidine) (**Co-(bpm-DTB)**), was introduced with structural analog cobalt tris(4,4'-di-*tert*-butyl-2,2'-bipyridine) (**Co-(bpy-DTB)**) to expand the scope of the comparison. The coordination geometry, diffusion coefficient, and spin states of Co(III) and Co(II) species were determined to ensure the properties of each analogous cobalt mediator are comparable for the study. The devices containing each of the four cobalt complexes were characterized by current density-voltage (J-V) curves in the dark and under illumination, short-circuit photocurrent transient (SCPT), and open-circuit voltage decay (OCVD). Chapter 4 summarizes key findings and provides suggestions for future

Chapter 2. Cobalt Tris(2,2'-Bipyrimidine) Complex Yields a High Open-Circuit Voltage in the Dye-Sensitized Solar Cell

Part of chapter 2 is published in the paper High-Voltage Dye-Sensitized Solar Cells Mediated by $[\text{Co}(2,2'\text{-bipyrimidine})_3]^z$ (*Inorg Chem.* **2017**, 56 (5), 2383).

2.1. Introduction

Polypyridyl cobalt complexes are highly attractive mediators because E° can be easily shifted by changing the structure of the coordinating ligands. Two modification strategies have been utilized to increase the E° of the cobalt complexes. The first method involves functionalizing polypyridyl ligands with electron-withdrawing substituents such as chloride, nitro, methyl ester, and cyanide.^{43,57,64,88} Chemical instability, low solubility, and slow ion diffusion due to the bulky structure pose as potential problems in functionalized cobalt complexes. Kirner *et al.* designed a cyano-substituted cobalt complex **Co-(CN-bpy)** with an E° of 0.92 V vs NHE, but low solubility and precipitation in the presence of electrolyte additives prevented the use of the complex in actual devices.⁶⁶ Alternatively, E° can be elevated by replacing the on pyridine ring of polypyridyl ligands with other nitrogen-containing heterocycles such as pyrazole.^{63,64} A computational study reported by Sun *et al.* further showed that inserting nitrogen atoms in terpyridine to form various pyrimidine-containing ligands also positively shifted the E° of cobalt complexes.⁹⁸ No experimental work has been performed to test those complexes in actual devices, but the study highlighted the importance of nitrogen atoms in tuning E° without increasing the size of cobalt complexes.

In this chapter, a new bipyrimidine-based cobalt mediator **Co-bpm** in the dye-sensitized solar cell is reported. The ligand choice was inspired by the modulation of E° found in polypyrimidyl ruthenium complexes^{99,100} and the promising high E° values calculated for

tridentate polypyrimidyl cobalt complexes.⁹⁸ **Co-bpm** is composed of three bidentate 2,2'-bipyrimidine (**bpm**) ligands coordinated in an octahedral geometry (Figure 2.1). It was first reported by Ruminski *et al.* as a mediator candidate in batteries and has not been studied in any area of research for the past three decades.⁹⁷ The E° of **Co-bpm** was found to positively shift by +0.5 V to 1.07 V vs NHE compared to the widely used **Co-bpy** with a E° of 0.57 V vs NHE.¹⁰¹ This value is the highest E° obtained by a cobalt complex that can still regenerate many organic sensitizers in the DSSC to the best of our knowledge. Physical, optical, and electrochemical characterizations were performed to corroborate with previously reported results and determine the compatibility and the capacity for **Co-bpm** to function as a redox mediator in the DSSC. A preliminary electrolyte containing limited concentration of **Co-bpm** was first tested in fully-assembled devices to demonstrate that the complex can mediate charge and operate in the devices. Two methods were then implemented to improve the solubility of **Co-bpm** in order to optimize the electrolyte formulation and target record high V_{OC} . **Co-bpm** represents the Co(III)/Co(II) redox couple balanced by hexafluorophosphate anions (PF_6^-) unless otherwise stated.

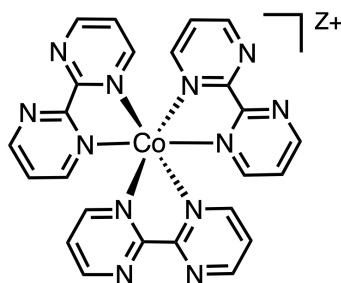


Figure 2.1. Chemical structure of **Co-bpm**. $Z = +2$ or $+3$

2.2. Results and Discussion

2.2.1 Structural, Optical, and Electrochemical Characterization

The structure of the Co(II) form of **Co-bpm** was determined by single crystal X-ray diffraction techniques (Figure 2.2). The complex exhibited a distorted octahedral geometry with

cobalt-nitrogen bond distances of ca. 2.1 Å. ^1H NMR in CD_3CN revealed three signals in the 20–110 ppm range for Co(II) species. The chemical shifts of the signals are consistent with the values produced by the deshielding effects from a paramagnetic Co(II) metal center (Figure 2.3b). The three proton peaks of the diamagnetic low-spin Co(III) species were present in the aromatic region from 7–9 ppm and differed from free **bpm** ligands in solution (Figure 2.3a,c). The Co(II) and Co(III) forms of **Co-bpm** were both stable in MeCN and only monometallic complexes were formed as indicated by the correct number of peaks in the characteristic chemical shift ranges for the paramagnetic and diamagnetic species.

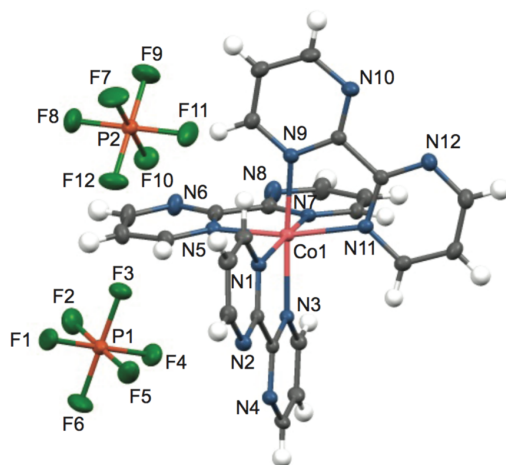


Figure 2.2. Thermal ellipsoid plot of **Co-bpm** drawn at the 50% probability level.

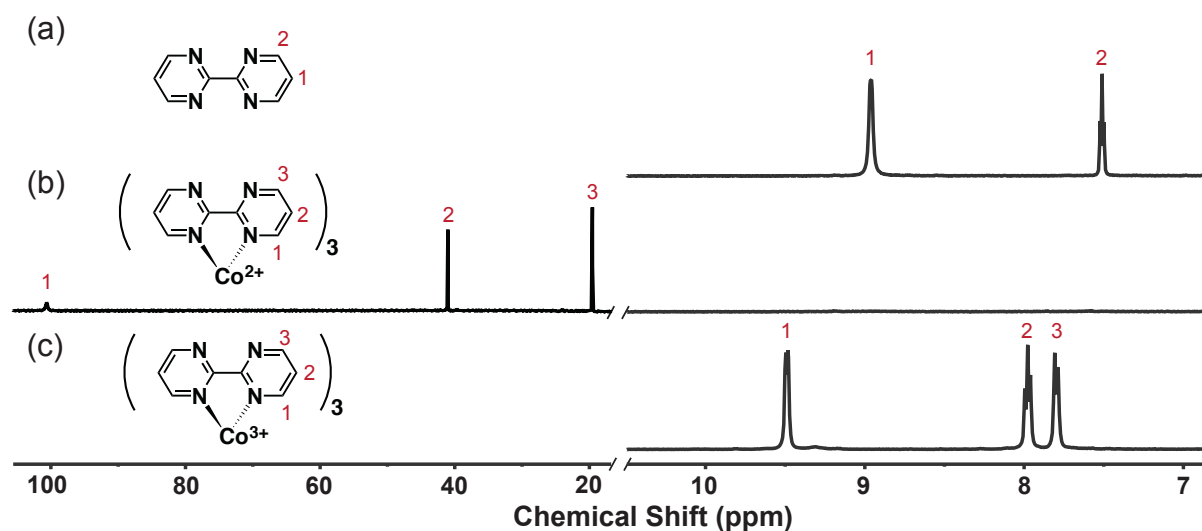


Figure 2.3. ^1H NMR in CD_3CN of **bpm** ligand in (a) free solution, (b) Co^{II} -**bpm** and (c) Co^{III} -**bpm**.

UV-vis absorption spectrum of the Co(II) form of **Co-bpm** recorded in MeCN showed one resolved absorption band at low energy and two overlapping bands at higher energies. In accordance with the spectroscopic analyses performed on other high spin d^7 octahedral cobalt complexes,¹⁰² intraligand $\pi\text{-}\pi^*$ transition and orbital forbidden $d\text{-}d$ transitions $^4T_1(F) \rightarrow ^4T_2(F)$ are assigned to bands with maxima at 243 and 935 nm, respectively, and $^4T_1(F) \rightarrow ^4T_1(P)$ is assigned to the shoulder at 465 nm (Figure 2.4). **Co-bpm** demonstrated exceptionally low molar extinction coefficient in the visible range. This property ensures minimal competitive absorption of light with the sensitizers when **Co-bpm** is used in the solar cell.

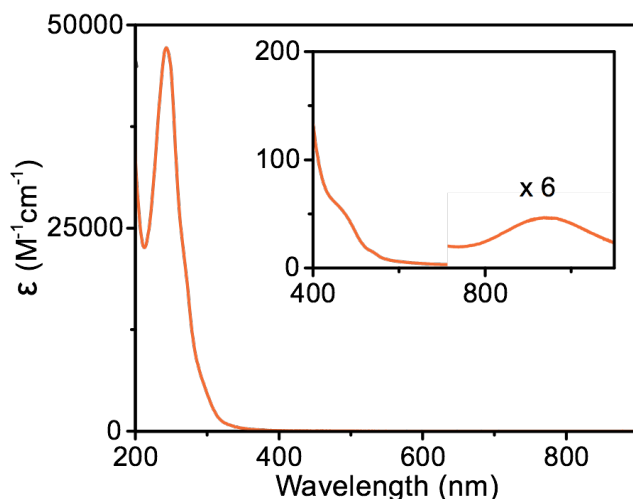


Figure 2.4. UV-Vis spectrum of **Co-bpm** in MeCN. The inset focuses on absorbance from 400-1100 nm with the curve from 700-1100 nm enlarged by 6-fold.

The cyclic voltammogram (CV) of **Co-bpm** recorded in MeCN displayed a quasi-reversible redox profile with a redox potential at 1.07 V vs NHE (0.86 V vs Ag/AgCl, Figure 2.5). The value was in close agreement with the previously reported value of 1.03 V.⁹⁷ A peak separation of greater than 59 mV is an indication of sluggish electron transfer kinetics at the electrode surface. The electron-withdrawing effect of uncoordinated nitrogen atoms on **bpm** is thought to decrease the basicity and electron donating ability of the coordinating nitrogen atoms compared to those in **bpy** which renders the **Co-bpm** harder to oxidize. The nitrogen atoms are

clearly operative in affecting the electron density at the cobalt center as the redox potential shifted by +500 mV compared to equivalent **Co-bpy** species.¹⁰¹

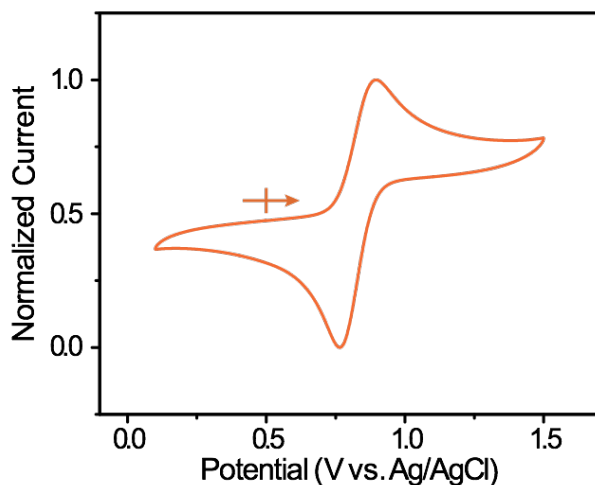


Figure 2.5. Cyclic voltammogram of **Co-bpm** in MeCN. Scan rate = 100 mV/s; WE: Au; RE: Ag/AgCl; CE: Pt wire. Arrow indicates the V_{OC} and the direction of the scan. Ferrocene was used as the internal standard (0.64 V vs NHE)¹⁰³.

Co-bpm was found to have three key qualities for a redox mediator. It was stable in MeCN, the most commonly used solvent in the liquid-DSSC electrolyte. A low absorption in the visible range was observed in **Co-bpm** which helps minimize interference with dye absorption. Most notably, E^0 of **Co-bpm** was positioned positive enough to realize very high V_{OC} and still ensure thermodynamically favorable dye regeneration so long as the redox potential of the dye is more positive than 1 V. Subsequently, the choice of dye is important for **Co-bpm** to function properly in the DSSC. The redox potential of **Dye-I**, an organic dye introduced in chapter 1, has a sufficiently positive redox potential at 1.27 V vs NHE to accommodate regeneration by **Co-bpm**. Every device presented in this chapter and the following chapter were sensitized with **Dye-I**.

2.2.2 First iteration of DSSCs Tested with Co-bpm

Electrolyte containing **Co-bpm** was tested in the DSSC. The intended electrolyte formulation optimized for cobalt mediator electrolytes consists of 0.2 M Co(II), 1:10 mole ratio of Co(III)/Co(II), 0.2 M *tert*-butylpyridine (TBP), and 0.1 M lithium perchlorate (LiClO₄) in MeCN. TBP and lithium ions are useful additives because they are found to affect the E_C of the TiO₂ and passivate the anode surface to inhibit recombination between the electron injected in the TiO₂ conduction band and the oxidized mediator species.^{70,72,104}

The solubility of [**Co-bpm**](PF₆)₂ at 0.026 M was an order of magnitude lower than the required Co(II) concentration of 0.2 M. It was also apparent that the addition of LiClO₄ considerably lowered the solubility of **Co-bpm** and initiated precipitation in MeCN due to the exchange of PF₆⁻ in [**Co-bpm**](PF₆)₂ with ClO₄⁻ anion. Considering the restrictions presented, the preliminary electrolyte formulation for **Co-bpm** was changed to 0.02 M Co(II), 0.002M Co(III), and 0.2 M TBP in MeCN. Devices without TBP were also tested for comparison.

An average PCE of 0.08% was obtained in devices without TBP compared to the 0.41% found in devices with TBP. The origin of the improved PCE in TBP-containing devices was a 5-fold increase in J_{SC} (Table 2.1). A slight increase in V_{OC} in the presence of TBP is rationalized by a negatively shifted TiO₂ conduction band due to TBP adsorption on anode surface.¹⁰⁵ Surface-adsorbed TBP is also speculated to create a physical barrier against direct contact of TiO₂ with mediator species, which likely contribute to reduced recombination and higher V_{OC} and J_{SC} .¹⁰⁴ All devices demonstrated FF under 0.4, which deviated significantly from 0.7-0.8 found in high efficiency cells. Although the average FF measured in additive-free and TBP-containing devices were the same, a tailing effect near V_{OC} was seen only for TBP-containing devices (Figure 2.6). A potential cause of the effect is briefly discussed later in the chapter.

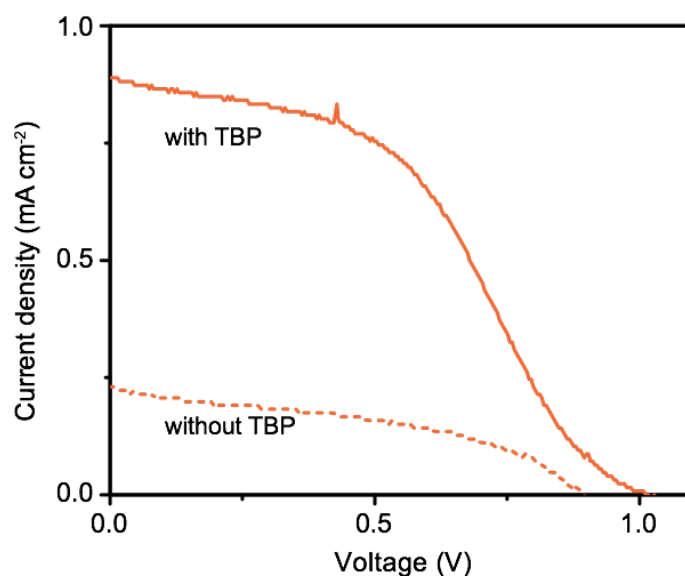


Figure 2.6. J-V curve of **Co-bpm** in MeCN with (solid line) and without (dash line) TBP. All electrolyte contains 0.02 M Co(II) and 0.002 M Co(III) in MeCN.

Table 2.1. Preliminary Device Performances of **Co-bpm** in MeCN.^a

Additives	PCE	V_{oc}	J_{sc}	FF
	%	V	mA cm^{-2}	
none	0.079 (± 0.009)	0.90 (± 0.07)	0.22 (± 0.02)	0.390 (± 0.009)
0.2 M TBP	0.41 (± 0.05)	0.99 (± 0.02)	1.1 (± 0.2)	0.39 (± 0.03)

^aElectrolytes contain 0.022 M Co(II) and 0.002 M nitrosonium hexafluorophosphate (NOPF₆). Values shown indicate mean value (and standard deviations in parentheses) for at least three devices.

The best preliminary cell exhibited PCE under 0.5% and was considerably lower than previously achieved 5% efficiency using **Dye-I** and the **Co-bpy** mediator.¹⁰⁶ The inconsistency in device fabrication was unlikely the main cause of this performance difference because the same electrode materials and assembly protocols were employed in both studies. Instead, the most apparent discrepancy between the electrolytes is the mediator concentration. At low concentrations, less mediator species is available to quickly regenerate dye molecules and transport charge in the electrolyte. Mediator concentrations were reported to be proportional to dye regeneration rates for several cobalt species with higher concentrations typically offering

better performances.^{45,67,68} Two effective methods to increase the solubility of **Co-bpm** and obtain superior device performance were to change the solvent composition of the electrolyte and to change the counterion of the mediator.

2.2.3 Improving Co-bpm Device Performance with Alternative Solvent Systems

The initial target was to identify an alternative solvent that offers the best cell performance and high **Co-bpm** solubility. Of the sixteen single and binary solvent system tested (see Table A.6 in appendix), the five most soluble systems were used in fully assembled cells. The concentration of Co(II) species was varied from 0.05 to 0.2 M depending on the maximum solubility in each solvent. Co(III) species and additives were excluded to reduce the number of variables. The PCE of devices prepared with any of the five solvent systems were higher than the device with MeCN, but the increase did not correspond to mediator concentration (Figure 2.7). Solvent viscosity did correlate to the PCE at the same **Co-bpm** concentration, presumably because higher solvent viscosity is linked to decreased ion mobility and lower J_{SC} .^{107–109} Based on these results, the best solvent system was 1:1 DMSO/MeCN, which yielded the highest PCE of 0.28% at a relatively high **Co-bpm** concentration of 0.15 M. Therefore, 1:1 DMSO/MeCN was used in the new electrolyte formulation consisting of the Co(III)/Co(II) redox couple at 0.15 M.

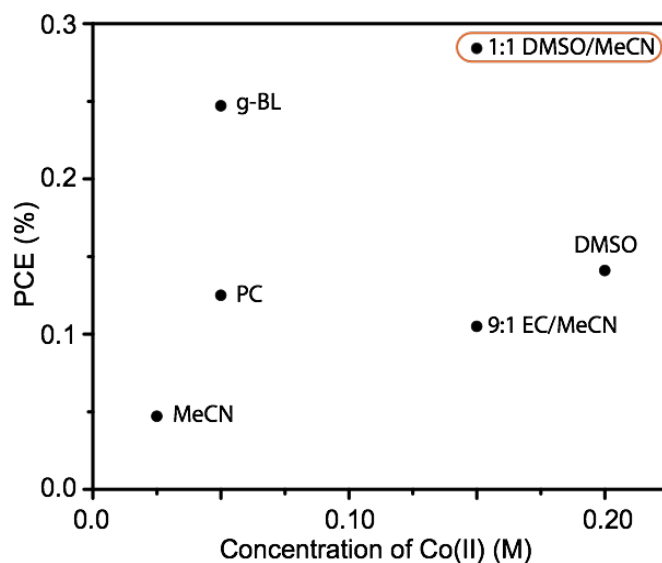


Figure 2.7. PCE of cells at different **Co-bpm** concentrations and in different electrolyte solvents [propylene carbonate (PC), γ -butyrolactone (g-BL), and ethylene carbonate (EC), and dimethyl sulfoxide (DMSO)].

The J-V curves of the best performing devices are presented in Figure 2.8. The average PCE of four cells was 1.04% and the average V_{OC} was >1 V (Table 2.2). The devices with 0.15 M of **Co-bpm** in 1:1 DMSO/MeCN outperformed devices containing 0.02 M of **Co-bpm** in the same solvent system and in MeCN by 2-folds. The 1:1 DMSO/MeCN solvent system was found to facilitate physical and chemical degradation in the cell despite the improved PCE performance. Dye desorption from the anode was visually observed after the electrolyte was injected in the devices. The partial degradation of **Co-bpm** in 1:1 DMSO/MeCN was also observed based on the presence of aromatic peaks associated with the free **bpm** ligand in DMSO- d_6 and the absence of these peaks in CD_3CN (Figure 2.9).

Table 2.2. Device Performances of **Co-bpm** in 1:1 DMSO/MeCN.^a

[Co ^{II} -bpm]	Additives	PCE	V_{oc}	J_{sc}	FF
		%	V	mA cm ⁻²	
0.02 M	none	0.35	1.08	0.91	0.35
0.15 M	none	1.0 (±0.1)	1.007 (±0.007)	2.3 (±0.4)	0.44 (±0.02)
	0.2 M TBP	0.57 (±0.02)	0.980 (±0.008)	2.2 (±0.2)	0.26 (±0.01)

^aAll electrolytes contained 1:10 ratio of Co(III)/Co(II). NOPF₆ was used to generate Co(III) *in-situ*. Values shown indicate mean values (and standard deviations in parentheses) for at least three devices. Values with no parentheses indicate performance of only one device.

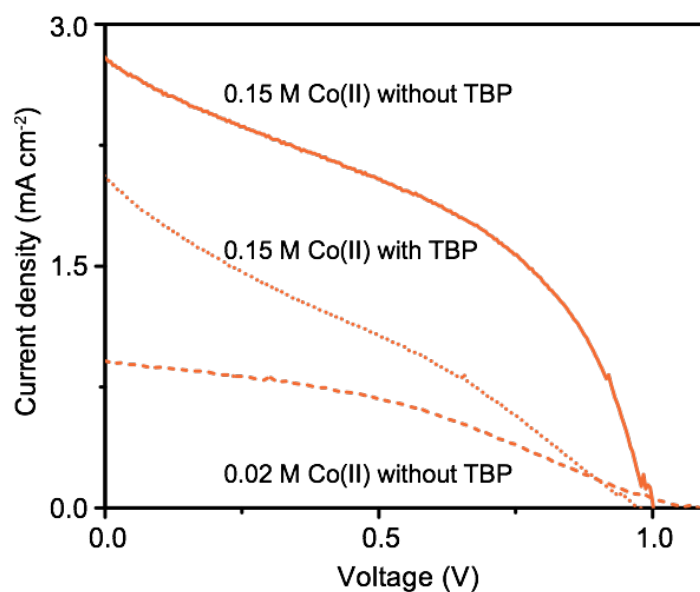


Figure 2.8. J-V curve of devices employing **Co-bpm** in 1:1 DMSO/MeCN with different electrolyte formulation. Electrolytes contain 0.02 M Co(II) without TBP (dash line), 0.15 M Co(II) without TBP (solid line), and 0.15 M Co(II) with TBP (dotted lined).

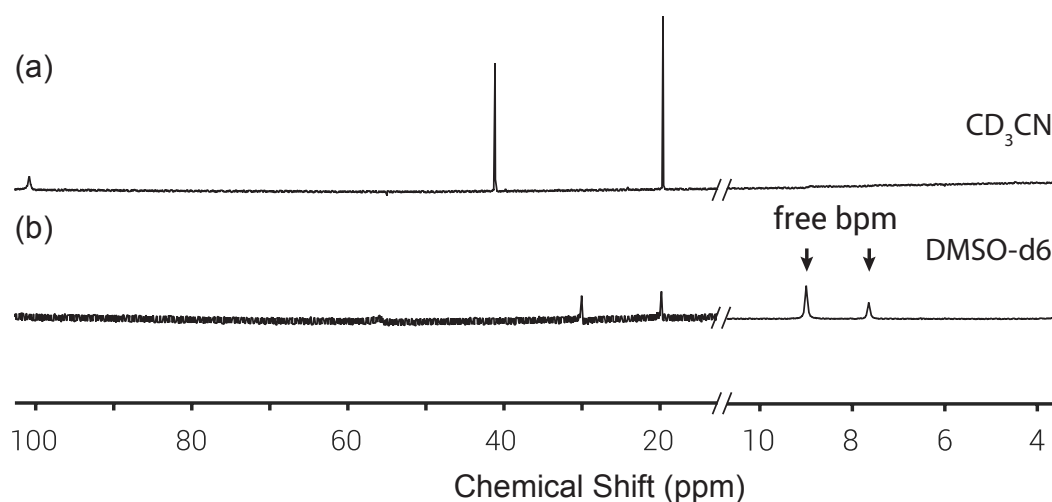


Figure 2.9. ^1H NMR of $\text{Co}^{\text{II}}\text{-bpm}$ in (a) CD_3CN and (b) DMSO-d_6 . Arrow indicates free bpm ligand peaks.

Moreover, the solvent system was incompatible with TBP. The PCE was improved by 5-fold when TBP was added in MeCN electrolyte, but PCE was reduced by half when it was added in 1:1 DMSO/MeCN electrolyte (Table 2.2). FF decreased from 0.44 to 0.26 and the J-V curve severely deviated from ideality (Figure 2.8). One proposed reason is that DMSO acts as both a solvent and an additive that can tune the conduction band of TiO_2 in the same way as TBP.¹⁰⁷ The addition of TBP does not improve V_{OC} but instead increases the viscosity of the electrolyte which leads to a higher series resistance and lower FF .

2.2.4 Improving Co-bpm Device Performance by Changing the Counterion

An effort to increase the **Co-bpm** concentration was made by pairing the complex with various counterions to identify the most soluble **Co-bpm** salt in MeCN. The lipophilicity and size matching of the counterion with **Co-bpm** are important to facilitate greater dissolution in organic solvents.^{110,111} In addition to PF_6^- , five other counterions were surveyed including perchlorate (ClO_4^-), tetrafluoroborate (BF_4^-), tetraphenylborate ($\text{B}(\text{C}_6\text{H}_5)_4^-$), triflate (OTf), and bistriflimide (TFSI^-). The solubility of the complex increases from $\text{ClO}_4^- < \text{BF}_4^- < \text{B}(\text{C}_6\text{H}_5)_4^- < \text{OTf}^- < \text{PF}_6^- < \text{TFSI}^-$ (Table 2.3). Therefore, $[\text{Co-bpm}](\text{TFSI})_2$ salt was chosen for device testing.

Table 2.3. Saturation Concentration of [Co-bpm](X)₂ in MeCN.

Counterion (X)	g/mL	mM
BF ₄ ⁻	0.002	3
ClO ₄ ⁻	0.003	4
B(C ₆ H ₅) ₄ ⁻	0.014	12
OTf ⁻	0.022	27
PF ₆ ⁻	0.022	27
TFSI ⁻	0.203	186

[Co-bpm](TFSI)₂ concentration saturated at approximately 0.18 M in MeCN. A slightly lower concentration at 0.15 M was used in the electrolyte to ensure that solvent evaporation during cell fabrication would not cause precipitation. Lithium bistriflimide did not interfere with Co-bpm solubility and was successfully employed as an additive. The J-V curves of cells under different electrolyte conditions are presented in Figure 2.10. No difference in PCE was found between devices containing TFSI or PF₆ counterions at 0.02 M of Co-bpm (Figure 2.10a). The result indicates that the counterion does not affect the cell performance. PCE increased by 200% when the concentration of [Co-bpm](TFSI)₂ increased from 0.02 M to 0.15 M (Figure 2.10b, Table 2.4). The addition of Li⁺ in the electrolyte offered a slight improvement in J_{SC} (Figure 2.10c). The best performing device exhibited PCE of 1.04% and a remarkably high V_{OC} of 1.1 V. The results confirmed that high Co-bpm concentration is crucial in enhancing device performance, but this study also revealed that other factors are limiting the PCE to 1%.

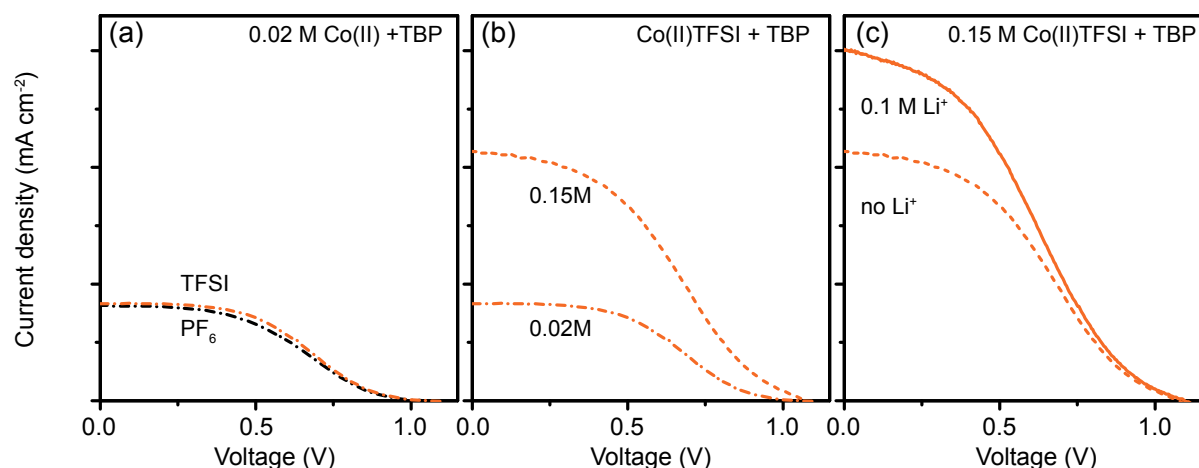


Figure 2.10. J-V curves of devices containing **[Co-bpm](TFSI)** electrolytes presented in Table 2.4. Comparisons are made between three different conditions: (a) TFSI (orange dash dot line) and PF₆ (black dash dot line) counterion; (b) 0.02 M (dash dot line) and 0.15 M (dashed line) Co(II) concentration; and (c) with (solid line) and without (dashed line) lithium additive. All electrolytes contain 0.2 M TBP and 1:10 ratio of Co(III)/Co(II) in MeCN.

Table 2.4. Device Performances of **[Co-bpm](PF₆)** and **[Co-bpm](TFSI)** with Various Electrolyte Formulation.^a

Compound	Conc.	Additives	PCE	V_{oc}	J_{sc}	FF
	M		%	V	mA cm ⁻²	
[Co-bpm] (PF ₆)	0.02	TBP	0.33	1.04	0.82	0.39
	0.02	TBP	0.34 (±0.02)	1.04 (±0.02)	0.85 (±0.02)	0.39 (±0.02)
[Co-bpm] (TFSI)	0.15	TBP	0.79 (±0.08)	1.07 (±0.02)	2.0 (±0.1)	0.36 (±0.01)
	0.15	TPB + LiTFSI	0.9 (±0.1)	1.07 (±0.02)	2.7 (±0.3)	0.33 (±0.03)

^aAll electrolytes contained 1:10 ratio of Co(III)/Co(II). Solid Co(III) was used. Values shown indicate mean value (and standard deviations in parentheses) of two or more devices. Values with no parentheses indicate performance of only one device.

2.2.5 Discussion of the “S-shape” J-V Curve

One recurring characteristic in the J-V curve is the tailing effect near V_{oc} . No clear explanation can be drawn solely from device performance. The “S-shaped” curve is rarely seen in DSSC with liquid electrolyte,^{112,113} but has been noted in solid-state solar cell devices. In solid-state solar cells, the shape is often attributed to charge mobility imbalance^{114,115} or charge

accumulation.^{116,117} Charge mobility imbalance is not applicable in liquid-DSSC because the mechanism and medium for charge mediation is different. Charge mobility can be severely hindered by the presence of grain boundaries in a solid whereas it is only limited by mediator diffusion in liquid-based devices.

There may be an equivalent effect to charge accumulation in the DSSC. In solid-state devices, electrons are accumulated at the anode when there is an insufficient population of holes at the cathode. The equivalent scenario in the DSSC is an accumulation of electrons at the anode where the reduction reaction between the mediator and the cathode is slow. Ashbrook *et al.* noted the S-shaped curves in the liquid DSSC in their study and attributed the effect to rate-limiting electron transfer at the Au cathode at high voltage.¹¹³ A similar reason may apply for **Co-bpm**.

2.3 Conclusion

Co-bpm was characterized and tested in fully-assembled DSSC. The low solubility of **Co-bpm** in MeCN was overcome by changing the solvent composition to 1:1 DMSO/MeCN and by employing the TFSI salt, but DMSO was found to cause degradation in the devices. J_{SC} doubled when the concentration of **Co-bpm** increased from 0.02 M to 0.15 M. The highest V_{OC} achieved in **Co-bpm** mediator-based devices was 1.1 V. This value matches to the benchmark V_{OC} of 1.1 V found in highly optimized **Co-(bpy-pz)** devices. It was demonstrated that the high E^0 of mediators indeed correlate to high V_{OC} in the device.

Chapter 3. Elucidating the Role of Cobalt Electrolyte Redox Potential on the Performance of Dye-Sensitized Solar Cells

3.1. Introduction

In chapter 2, it was demonstrated that a high V_{OC} of 1.1 V can be achieved in devices containing **Co-bpm**. The PCE, however, was limited to 1% because the J_{SC} was only 2.7 mA cm⁻². The maximum possible J_{SC} for a DSSC containing **Dye-I**, which absorbs light at wavelengths < 600 nm, is 14 mA cm⁻².^{30,106} This is a large discrepancy because less than 20% of the maximum accessible photocurrent is measured in **Co-bpm** mediator-based devices.

A survey of the literature reveals that the V_{OC} and J_{SC} are closely intertwined to the E^0 .^{43,56,62,74,118} The link has been rationalized by a smaller ΔG^0_{reg} and a larger ΔG^0_{rec} as E^0 approaches the redox potential of the ground-state dye. A smaller ΔG^0_{reg} and a larger ΔG^0_{rec} typically correspond to slower regeneration, faster recombination, and lower J_{SC} in the DSSC.^{44,45} The highly positive E^0 of **Co-bpm** is suspected to be a key reason for low J_{SC} caused by greater recombination. A slightly negative shift in E^0 from 1.07 V vs NHE is predicted to reduce recombination and produce higher J_{SC} in the DSSC. This chapter aims to test these two hypotheses by performing a comparative study across mediators of varying E^0 . A new *tert*-butyl substituted cobalt complex **Co-(bpm-DTB)** with the same ligand core structure as **Co-bpm** is introduced because alkyl substituents are known to negatively shift the E^0 of transition metal complexes and hinder interfacial recombination (Figure 3.1).⁷⁶ An added benefit is that the alkyl substituents on **Co-(bpm-DTB)** promote higher solubility in organic solvent than **Co-bpm**.

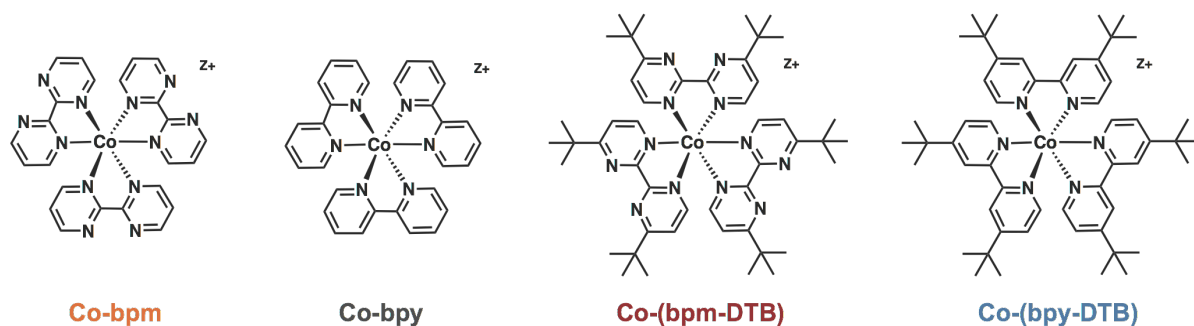


Figure 3.1. Chemical structure of the **Co-bpm**, **Co-bpy**, **Co-(bpm-DTB)**, and **Co-(bpy-DTB)**. $Z = +2$ or $+3$.

It is difficult to elucidate the effect of E° on device performance and recombination kinetics based solely on **Co-bpm** and **Co-(bpm-DTB)** because the molecular size of the two complexes are different. The recombination rate is influenced by reorganization energy (λ) and diffusion coefficients (D_{bulk}) which are sensitive to the size of the mediator.^{84,89,119,120} Two reference mediators, **Co-bpy** and **Co-(bpy-DTB)**, are included in the comparative study in an attempt to eliminate these size-dependent factors (Figure 3.1). **Co-bpy** and **Co-(bpy-DTB)** are two well-studied mediators with near-identical structure but have considerably lower E° than their **bpm**-based counterpart (Figure 3.2). The comparison between **Co-bpm**, **Co-bpy**, **Co-(bpy-DTB)**, and **Co-(bpm-DTB)** provides an unprecedented platform to examine the effect of E° on recombination kinetics in DSSC using structurally analogous cobalt mediators.

Various characterization methods were used to confirm and compared the sizes, diffusion coefficients, spin states, and E° s of the four complexes. It is anticipated that the device performances for the two pairs of structurally analogous complexes are predominantly affected by the E° in the absence of size and spin state differences. Fully assembled devices containing the four cobalt mediators were constructed and examined using an illuminated J-V curve. Recombination kinetics was qualitatively assessed by dark current density-voltage (J-V) and open-circuit voltage decay (OCVD) measurements.

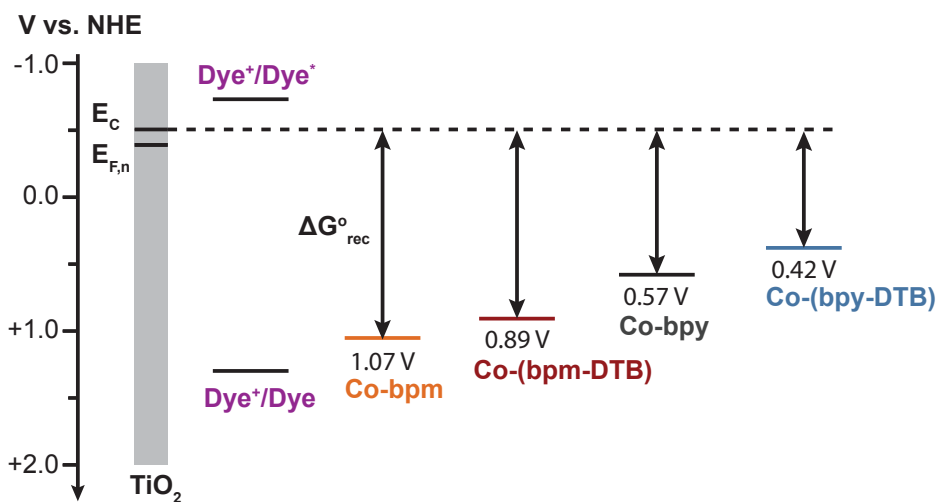


Figure 3.2. Redox potential diagram of the four redox mediators, ground-state and excited-state level of dye, conduction band level (E_C), and the quasi-Fermi level of TiO_2 ($E_{F,n}$). The Gibbs free energy of recombination ($\Delta G^\circ_{\text{rec}}$) is also indicated.

3.2. Results and Discussion

3.2.1 Comparing the Properties of Co-bpy, Co-bpm, Co-(bpy-DTB), and Co-(bpm-DTB)

Single-crystal XRD of $[\text{Co-bpm}](\text{PF}_6)_2$ and $[\text{Co-(bpm-DTB)}](\text{PF}_6)_2$ were compared to the literature XRD of $[\text{Co-bpy}](\text{PF}_6)_2$ ¹²¹ and $[\text{Co-(bpy-DTB)}](\text{PF}_6)_2$ ¹²². The Co-N bond length and N-Co-N angles (ϕ and θ) are summarized in Table 3.1. ϕ represents the N-Co-N angle of the same ligand and θ is the N-Co-N angle between adjacent ligands.

All four cobalt complexes exhibit octahedral geometries corresponding to the chemical structure shown in Figure 3.1. The Co-N bond lengths vary minimally from 2.10-2.16 Å, and ϕ lie within 76-78° in all complexes (Table 3.1). The observed Co-N bond lengths are characteristic of high-spin d^7 cobalt complexes.¹²² The radii of the cobalt complexes were estimated by averaging the distances between the Co atom and the center of the most peripheral hydrogen atom on each ligand. The average radius of **Co-bpm** and **Co-bpy** is the same at 5.8 Å. Both **Co-(bpm-DTB)** and **Co-(bpy-DTB)** have average radii of 8.0 Å. **Co-bpm** and **Co-(bpm-DTB)** have a slightly longer Co-N bond length and smaller ϕ than their **bpy**-based analogs. The slightly larger

θ values found in **Co-(bpm-DTB)** and **Co-(bpy-DTB)** compared to **Co-bpm** and **Co-bpy** are explained by steric repulsion of *tert*-butyl substituents on adjacent ligands. Otherwise, two pairs of the structural analogs have very similar geometric parameters.

Table 3.1. Bond Lengths and Angles of **Co-bpy**, **Co-bpm**, **Co-(bpy-DTB)**, and **Co-(bpm-DTB)**.

XRD parameters ^a	Co-bpm	Co-bpy ¹²¹	Co-(bpm-DTB)	Co-(bpy-DTB) ¹²²
Co-N bond length (Å)	2.1210(18)- 2.1494(18)	2.117(4)- 2.146(4)	2.126(3)- 2.158(3)	2.095- 2.133
N-Co-N bond angle ϕ^b (°)	76.46(7)- 76.86(7)	77.02(15)- 77.66 (14)	76.46(10)- 76.49(10)	77.22- 77.43
N-Co-N bond angle θ^c (°)	90.42(7)- 98.29(7)	90.63(15)- 96.86(15)	92.00(10)- 99.64(10)	93.16- 99.37

^aAll parameters are reported as a range. ^b ϕ = N-Co-N angle of the same ligand. ^c θ = N-Co-N angle between adjacent ligands.

The diffusion coefficients (D_{bulk}) of the four cobalt complexes were quantified by performing linear sweep voltammetry using a rotating disk electrode (LSV-RDE) and applying the Koutecky-Levich equation to the acquired data (see chapter 5). Only one measurement was taken for each complex. D_{bulk} of ferrocene was measured to evaluate the accuracy of the measurement, which agreed with literature values of $2.43 \times 10^{-5} \text{ cm}^2 \text{ s}^{-1}$.¹²³ There is a discrepancy observed in the D_{bulk} value of **Co-bpy** measured using Au and GC electrode, but the origin is not known. Nonetheless, the same D_{bulk} of $1.2 \times 10^{-5} \text{ cm}^2 \text{ s}^{-1}$ was obtained for **Co-bpy** and **Co-bpm** using a GC electrode (Table 3.1). This result indicates that the diffusivity of structural analogs is the same as in *tert*-butyl substituted complexes. D_{bulk} was not successfully obtained for **Co-(bpm-DTB)**, but the value is presumably close to D_{bulk} of **Co-(bpy-DTB)** due to a comparable molecular size. A smaller D_{bulk} measured for **Co-(bpy-DTB)** compared to **Co-bpy** is consistent with bulkier complexes experiencing slower mass transport in solution (Table 3.1).^{76,84}

Table 3.2. Effective Magnetic Moments (U_{eff}), Redox Potentials (E°), and Diffusion Coefficients (D_{bulk}) of Co(II) Species Measured in MeCN.

Compound	D_{bulk}	U_{eff}^a	$E^{\circ b}$
	$\times 10^{-5} \text{ cm}^2 \text{ s}^{-1}$	Bohr magneton	V vs NHE
Co-bpy	1.01 ^c , 1.21 ^d	4.72	0.57
Co-(bpy-DTB)	0.83 ^c	4.42	0.42
Co-bpm	1.20 ^d	4.86	1.07
Co-(bpm-DTB)	-	4.66	0.89
Fc	2.48 ^c	-	0.64

^a Obtained by Evans Method (see chapter 5). ^bCV in 0.1M NBu₄PF₆, WE: Au. ^cLSV-RDE in 0.1 M NBu₄PF₆, WE: Au. ^dLSV-RDE in 0.1 M NBu₄PF₆, WE: GC

The spin states of the Co(II) and Co(III) species were determined by NMR. The effective magnetic moments (U_{eff}) for all four Co(II) species were measured by Evans method and fall between 4.4-4.8 Bohr magnetons, the characteristic range for paramagnetic high-spin Co(II).¹²⁴ The result is consistent with the characteristic Co-N bond length found in XRD. The proton peaks of all Co(III) species situate within the chemical shift range of 0-13 ppm and exhibit the predicted splitting pattern. The presence of proton coupling at low chemical shift values is indicative of diamagnetic low-spin Co(III).

The four complexes are expected to undergo spin crossover during electron transfer due to their preferential high-spin Co(II) and low-spin Co(III) configuration. Spin crossover is known to impact the inner reorganization energy, but the extent of the effect was not experimentally or computationally determined here. The inner reorganization energy is anticipated to be fairly similar across the four cobalt complexes because it was previously reported that the inner reorganization energy is insensitive to the donor strength of bidentate ligands on high-spin Co(II) complexes despite significant shifts in E° .⁸⁶ Furthermore, Sun *et al.* have calculated that the number of nitrogen have negligible effect on the inner reorganization energy of several structural

analogs of **Co-tpy**.⁹⁸ The outer reorganization energy, which depends on the mediator radii, is also not expected to vary greatly between **Co-bpm** and **Co-bpy** or **Co-(bpm-DTB)** and **Co-(bpy-DTB)** due to their comparable sizes.¹²⁰

The UV-vis profiles of the four complexes were examined to ensure minimal absorption of light in the visible region (Figure 3.3). The presence of *tert*-butyl substituents has no significant effect on the absorption profiles. The octahedral ligand-field splitting energy between the two sets of *d*-orbitals is nearly the same across the four complexes. This claim is supported by the UV-Vis absorption spectra where the lowest energy *d-d* transition bands for the four Co(II) complexes lie at approximately the same value of ~ 900 nm (Figure 3.3 inset). The absorption peaks of all four complexes overlap from 400 to 800 nm with low molar extinction coefficients (ϵ) under $200 \text{ M}^{-1} \text{ cm}^{-1}$ (Figure 3.3 inset). This result indicates that cobalt complexes have negligible interference with light absorption of **Dye-I**.

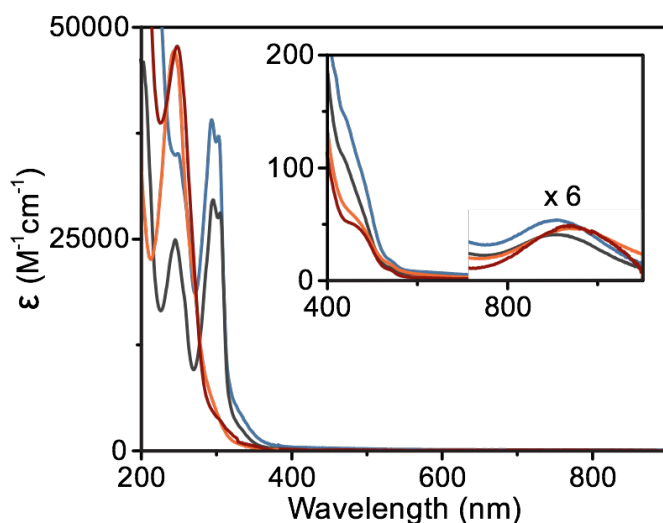


Figure 3.3. UV-vis of **Co-bpy** (grey), **Co-bpm** (orange), **Co-(bpy-DTB)** (blue) and **Co-(bpm-DTB)** (red). Inset shows zoomed spectrum in 400-1100 nm.

The E° for each cobalt complex was determined by cyclic voltammetry (CV). The E° of **Co-bpm** is anodically shifted by 0.5 V compared to **Co-bpy**, and **Co-(bpm-DTB)** is anodically shifted by 0.47 V compared to **Co-(bpy-DTB)** (Table 3.2). These shifts are consistent with the anodic shift of 0.4-0.5 V shift found in nickel, iron¹²⁵ and ruthenium⁹⁹ complexes coordinated to

bpy and **bpm** ligands. The order of cobalt complexes in ascending order of E^0 is **Co-(bpy-DTB)** < **Co-bpy** < **Co-(bpm-DTB)** < **Co-bpm** (Figure 3.4). Inductive effects are thought to be the key reason for the observed trends because uncoordinated nitrogen atoms in **bpm**-based ligands pull electron density away from the coordinating nitrogen atoms. Consequently, the lowest-unoccupied molecular orbital of Co(III) complex is stabilized, which makes the complex easier to reduce. *Tert*-butyl substituents partially negate the electron-withdrawing effect by providing electron density to the system.

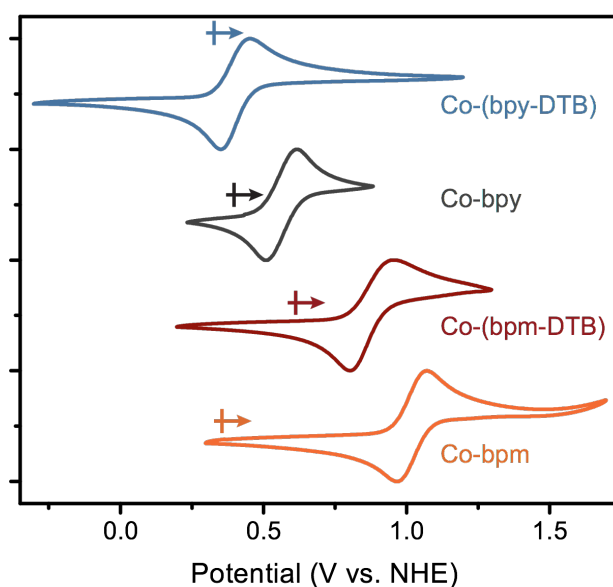


Figure 3.4. Cyclic voltammograms of **Co-(bpy-DTB)** (blue), **Co-bpy** (grey), **Co-(bpm-DTB)** (red), and **Co-bpm** (orange) in 0.1 M NBu_4PF_6 in MeCN. Scan rate = 100 mV/s; WE: Au; RE: Ag/AgCl; CE: Pt wire. Arrow indicates the V_{OC} and the direction of the scan.

Different electrochemical behaviors were observed for the complexes on gold (Au), Pt, and glassy carbon (GC) working electrode surfaces (Figure 3.5). The CV profile of **Co-(bpm-DTB)** was completely irreversible on Pt and GC electrodes, whereas that of **Co-(bpy-DTB)** showed a clear oxidation peak. These differences in redox reversibility may have implications on mediator regeneration kinetics at the cathode for different cobalt complexes in the DSSC, but it is not elaborated here. The electrochemistry of all four cobalt complexes were reversible on Au surfaces, but Pt was selected because of its use as the catalytic cathode material for the DSSC.

Moreover, Pt cathodes can be easily fabricated and have been shown to produce high performing devices with the **Co-(bpy-DTB)** mediator. The electrochemical behavior in CV does not necessarily correspond to the performance in devices because the morphology of the deposited Pt catalyst on the cathode is different from bulk Pt electrodes. Finally, the reproducibility of DSSC with gold cathodes is low, due to TBP adsorption.¹¹³

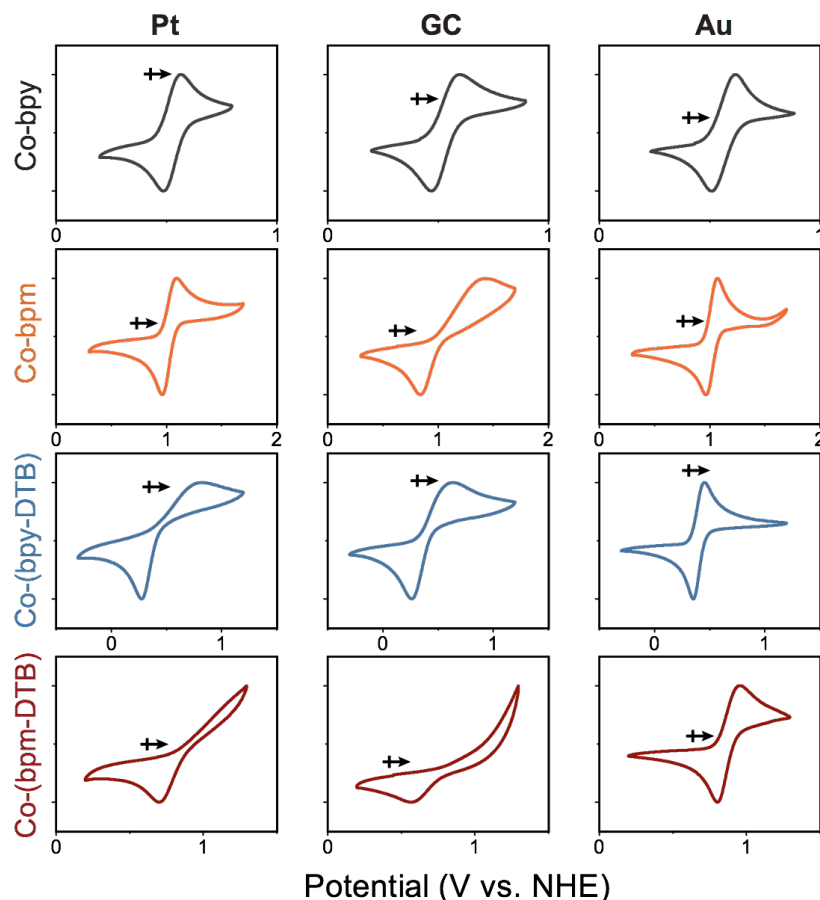


Figure 3.5. Cyclic voltammogram of **Co-bpy** (grey), **Co-bpm** (orange), **Co-(bpy-DTB)** (blue), and **Co-(bpm-DTB)** (red) with platinum (Pt), glassy carbon (GC), and gold (Au) working electrodes. Scan rate = 100 mV/s; WE: Au; RE: Ag/AgCl; CE: Pt wire. Arrow indicates the V_{oc} and the direction of the scan.

3.2.2 Redox Potential and Device Performance

The performance of the four mediators in the DSSC were examined by J-V curve, IPCE, and SCPT. The electrolyte contained 0.1 M LiTFSI, 0.2 M TBP, 0.2 M Co(II), and 0.02 M Co(II)

in MeCN. Only the soluble portion of the **Co-bpm** electrolyte was injected into the device which is estimated to contain approximately 0.18 M of Co(II) based on the maximum solubility of [**Co-bpm**](TFSI)₂. The PCE of **Co-bpm** mediator-based devices reported in this chapter is slightly lower than the values found in chapter 2 because anodes with thinner TiO₂ films and larger active areas were used. A thinner, larger film can result in less dye loading per area and higher probability for film defects, which lowers device performance.¹²⁶ Nonetheless, the devices containing **Co-bpy**, **Co-bpm**, **Co-(bpy-DTB)**, and **Co-(bpm-DTB)** were constructed with the same batch of printed anodes and consistent for comparison.

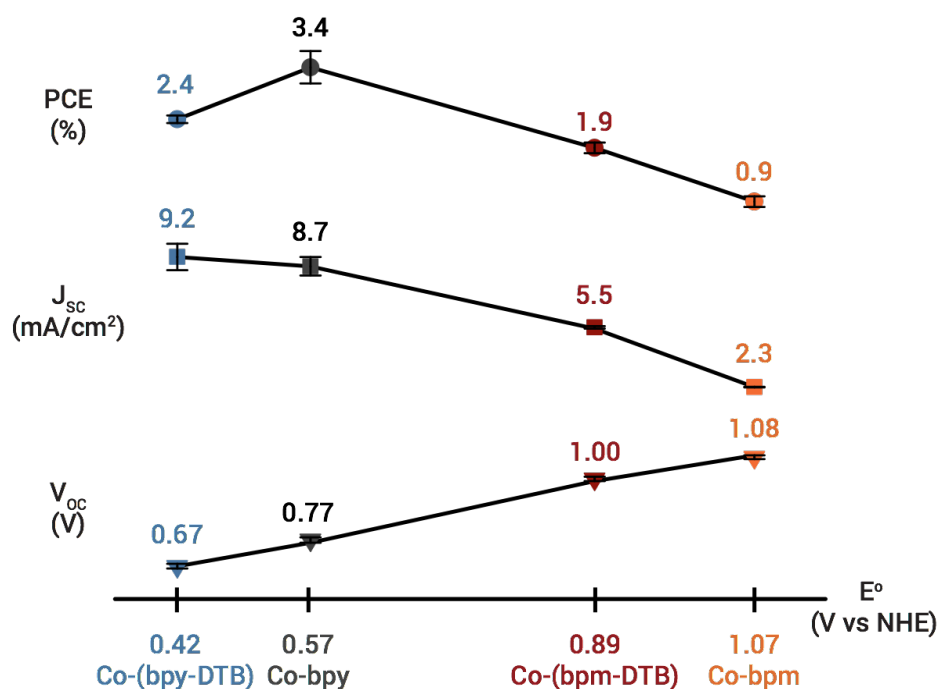


Figure 3.6. Plots of PCE, J_{sc} , and V_{oc} vs. E° of **Co-(bpy-DTB)** (blue), **Co-bpy** (grey), **Co-(bpm-DTB)** (red), and **Co-bpm** (orange).

Table 3.3. Average Device Performance of **Co-(bpy-DTB)**, **Co-bpy**, **Co-(bpm-DTB)**, and **Co-bpm** in DSSC.^a

Mediator ^b	PCE	V_{OC}	$E_{F,n}$ ^d	J_{SC}	FF
	%	V	V vs NHE	mA cm ⁻²	
Co-(bpy-DTB)	2.43 (±0.07)	0.672 (±0.009)	-0.252	9.2 (±0.7)	0.41 (±0.01)
Co-bpy	3.4 (±0.3)	0.77 (±0.01)	-0.20	8.7 (±0.5)	0.45 (±0.09)
Co-(bpm-DTB)	1.9 (±0.1)	0.997 (±0.008)	-0.107	5.45 (±0.07)	0.37 (±0.02)
Co-bpm^c	0.9 (±0.1)	1.078 (±0.007)	-0.008	2.27 (±0.02)	0.37 (±0.04)

^aTwo replicates were measured for each mediator condition. ^bThe electrolytes contained 0.2 M Co(II), 0.02 M Co(II), 0.1 M LiTFSI, 0.2 M TBP in MeCN. ^cOnly the fully dissolved portion of the electrolyte was used. ^dCalculated using Eq.1.4.

The device parameters obtained from J-V measurements are tabulated in Table 3.3 and presented graphically in Figure 3.6. Devices containing **Co-(bpm-DTB)** showed a 2-fold increase in J_{SC} and less than 10 mV decrease in V_{OC} compared to devices containing **Co-bpm**. A strong positive correlation near unity was calculated between E^0 and V_{OC} . V_{OC} increased linearly with E^0 , but J_{SC} was found to decline at a faster rate at more positive E^0 (Figure 3.6). Devices containing **Co-bpy** benefited from this disproportionate decrease in J_{SC} with respect to linear increase in V_{OC} to produce the highest PCE.

V_{OC} increases linearly with E^0 , but only +63 mV in V_{OC} is gained for every +100 mV shift in E^0 (the slope of the line in Figure 3.6). The ratio is expected to be 1:1 if the quasi-Fermi level of TiO₂ ($E_{F,n}$) is unchanged. Experimentally determined $E_{F,n}$, however, was found to shift positively by as much as +0.25 V between devices containing **Co-(bpy-DTB)** and **Co-bpm** (Table 3.3). The values were calculated by subtracting the E^0 of the cobalt mediator from measured V_{OC} . A downward (positive) shift in $E_{F,n}$ may be attributed to enhanced back-electron transfer and recombination as described in chapter 1.3.

The influence of mediator size on device performance was probed using short-circuit photocurrent transient (SCPT) measurements. An initial peak followed by steady-state

photocurrent under high intensity illumination for all cobalt mediators indicates that the steady-state J_{SC} is limited by the diffusion of the mediator (Figure 3.7). The peak is more prominent in devices with **Co-(bpy-DTB)** and **Co-(bpm-DTB)**, which is consistent with slower diffusion of bulkier complexes. The absence of the spike at low intensity illumination indicates that J_{SC} is no longer limited by diffusion. Nonetheless, the relative value of J_{SC} at steady state still correlates to E° of the cobalt species where mediators with higher E° value yield lower J_{SC} . Therefore, it is implied that J_{SC} is predominantly influenced by E° and not by the size of the cobalt mediator.

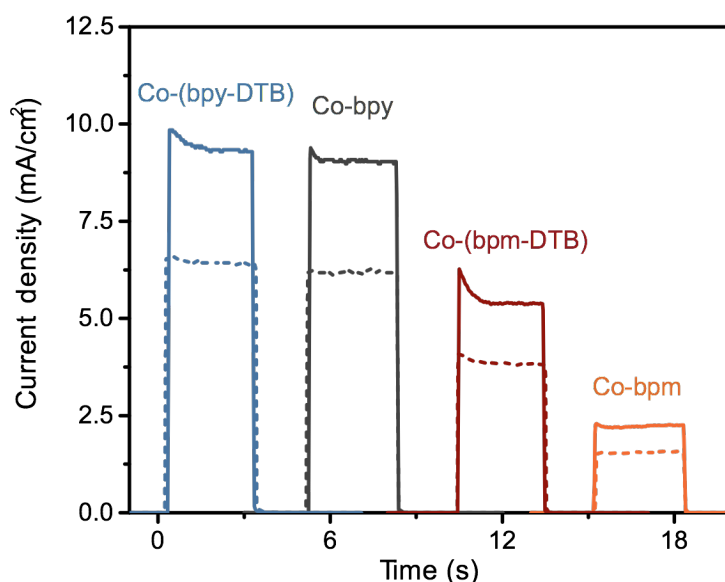


Figure 3.7. SCPT of best performing cell devices with cobalt mediator **Co-(bpy-DTB)** (blue), **Co-bpy** (grey), **Co-(bpm-DTB)** (red), and **Co-bpm** (orange). Solid line is high intensity (1 sun) and dash line is low intensity (0.7 sun) irradiation.

3.2.3 Redox Potential and Electron Recombination

Dark J-V measurements were collected to analyze electron recombination in the dark. A forward voltage bias was applied in the dark to populate the TiO_2 with electrons and raise the $E_{F,n}$. The generation of dark current at a specific $E_{F,n}$ signals significant electron recombination from TiO_2 to the redox mediator. Analysis of the dark J-V curves revealed that onset of dark current occurred at a more positive $E_{F,n}$ in devices containing mediators of more positive E° . This trend

is consistent with the results reported by Kirner *et al.* in substituted **Co-bpy** mediators.⁶⁶ The earliest $E_{F,n}$ onset at 0.6 V vs NHE was measured in devices containing **Co-bpm** and indicates the greatest recombination at the TiO_2 (Figure 3.8).

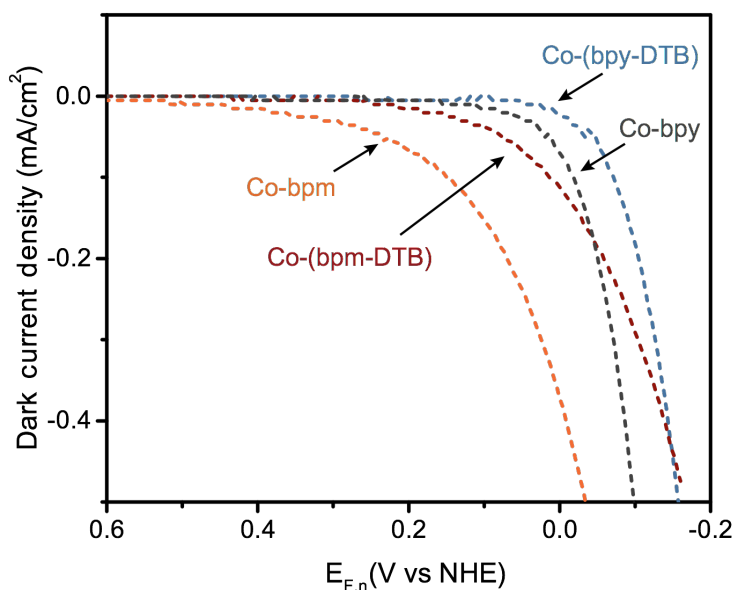


Figure 3.8. Dark J-V curve of best performing cell devices with cobalt mediator **Co-bpm** (orange), **Co-(bpm-DTB)** (red), **Co-bpy** (grey), and **Co-(bpy-DTB)** (blue).

Open-circuit voltage decay (OCVD) measurements were taken to examine electron recombination under illuminated conditions. OCVD operates in the reverse of dark current measurement; a drop in V_{OC} and a downward shift in $E_{F,n}$ is assessed after populating the TiO_2 with photo-injected electrons under illumination and turning off the light. The small electron lifetime (T_n) derived from the V_{OC} decay corresponds to fast recombination. T_n was found to decrease for cobalt mediators with positively shifted E^0 from **Co-(bpy-DTB)** > **Co-bpy** > **Co-(bpm-DTB)** > **Co-bpm**. The same trend was previously reported for substituted **Co-phen** complexes.⁶² At 0.2 V vs NHE, the T_n measured in devices containing **Co-bpm** is more than an order of magnitude greater than the value found in devices containing **Co-bpy** and **Co-bpm-DTB** (Figure 3.9). Recombination proceeded the fastest when **Co-bpm** is utilized which agreed with the results from the dark current measurements.

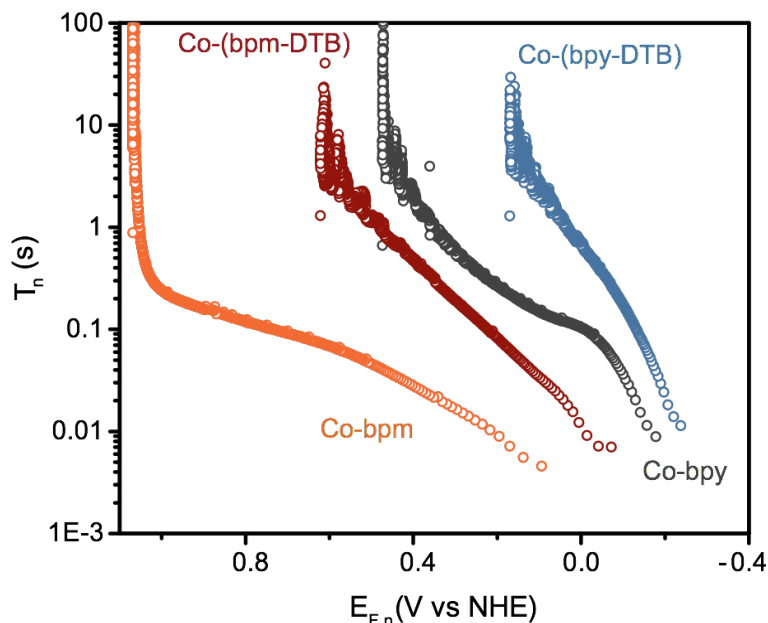


Figure 3.9. Electron lifetime (T_n) vs. quasi-Fermi level ($E_{F,n}$) graph derived from OCVD of the best performing cell devices with cobalt mediator **Co-bpm** (orange), **Co-(bpm-DTB)** (red), **Co-bpy** (grey), and **Co-(bpy-DTB)** (blue).

The shape of the semi-logarithmic electron lifetime curves in Figure 3.9 indicates that different recombination mechanisms are dominant at different $E_{F,n}$. T_n first increases linearly (in semi-logarithmic graph) with $E_{F,n}$ due to recombination of electrons from the trap states (Figure 3.10). At sufficiently positive $E_{F,n}$, surface state recombination dominates and T_n proceeds in a parabolic form.³² In the T_n plots for **Co-bpy** and **Co-bpm**, there are apparent non-linear regions which indicate surface-state recombination (Figure 3.9). The plots for **Co-(bpy-DTB)** and **Co-(bpm-DTB)** do not show obvious curvature, suggesting that surface-state recombination is not operative for these bulky complexes. It is reasonable to assume that *tert*-butyl groups may be shielding the metal centers, distancing the mediators from the surfaces, and preventing effective interaction for surface-state recombination.

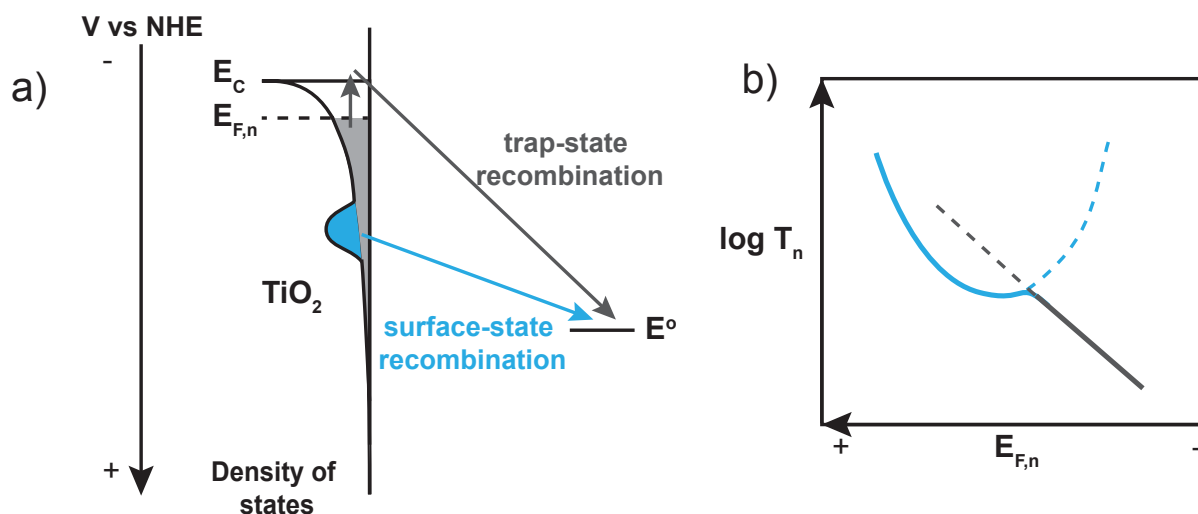


Figure 3.10. (a) OCVD recombination model showing electron recombination pathway from the surface states (blue) and trap states (grey) in TiO₂ and (b) a simulated semi-logarithmic electron lifetime (T_n) vs quasi-Fermi Level ($E_{F,n}$). The parabolic curve pertains to surface-state recombination (blue solid and dash line), and the linear line is associated with trap-state recombination (grey solid and dash line). The presence of both recombination mechanism yields a merge of the two curves (blue and grey solid line).

3.3 Conclusion

Co-bpy, **Co-bpm**, **Co-(bpy-DTB)**, and **Co-(bpm-DTB)** were synthesized and characterized by various experimental methods. The spin states of Co(II) and Co(III) species for the four complexes were the same, and similar optical properties were observed. The size and diffusion coefficient of structurally analogous cobalt complexes were found to be identical by XRD and LSV-RDE. The E° of the four complexes varied from 0.42 V to 1.07 V vs NHE. The electrochemical properties were dependent on the working electrode material. Comparison between device performance of the four cobalt mediators revealed a clear correlation between E° , J_{SC} , and V_{OC} . Devices containing **Co-(bpm-DTB)** showed a 2-fold difference in J_{SC} and very little difference in V_{OC} compared to devices containing **Co-bpm**, showing that a small negative shift in E° is beneficial to improve device performance. Earlier dark current onset and shorter T_n in devices containing **Co-bpm** are ascribed to greater recombination. *Tert*-butyl substituents on **Co-(bpm-DTB)** and **Co-(bpy-DTB)** also appeared to block surface-state recombination compared to

their unsubstituted counterpart. It is concluded that a substantial drop in J_{SC} is driven by fast recombination with **Co-bpm** and can be improved by devising strategies to reduce surface state TiO_2 interaction such as adding a thin layer of metal oxide above the TiO_2 .^{82,127–129}

Chapter 4. Conclusion and Future Directions

4.1. Conclusion

The first implementation of **Co-bpm** as a redox mediator in the DSSC was presented and achieved remarkably high V_{OC} of 1.1 V. This value is equal to the highest V_{OC} reported in a highly-optimized cobalt mediator-based device.⁸³ **Co-bpm** was found to have desirable electrochemical and optical traits to function well as a redox mediator. Poor **Co-bpm** solubility was overcome by changing the electrolyte solvent from MeCN to 1:1 DMSO/MeCN or by utilizing a TFSI⁻ counterion. The electrolyte containing 1:1 DMSO/MeCN was unsuitable in the DSSC due to chemical degradation of the mediator and dye desorption on the anode in the presence of DMSO. Mediator concentration was found to impact device performance to a lesser extent than expected. The source of the tailing “S-shaped” J-V curve was speculated to arise from charge accumulation due to slow mediator regeneration near open-circuit condition.

It was identified that J_{SC} was a limiting factor in the performance of **Co-bpm** mediator-based devices. The origin of low J_{SC} was investigated by conducting a comparative study with structural analog **Co-bpy** and two *tert*-butyl substituted complexes, **Co-bpm-DTB** and **Co-bpy-DTB**. A clear empirical relationship was observed in the device parameters of different cobalt mediators whereby V_{OC} increased linearly and J_{SC} decayed nonlinearly with positive shifts in E° . Devices containing **Co-bpm** exhibited the shortest electron lifetime in TiO₂ and lowest $E_{F,n}$ at open-circuit condition due to greater surface-state recombination. It is one of the primary reasons for the inferior performance in **Co-bpm** mediator-based DSSC.

4.2. Future Directions

Since greater surface-state and trap-state recombination contribute to the low photocurrent found in **Co-bpm** mediator-based devices, recommended future works can be directed toward

reducing the interaction between **Co-bpm** and the TiO₂ surface to improve device performance. The next step would be to create a physical barrier at the anode interface by sensitizing bulkier dye and depositing metal oxide blocking layer above the TiO₂ surface. Kakiage *et al.* recently reported decent PCE and extremely high photovoltage in bromide mediator-based devices by sensitizing high redox potential silyl-anchored dyes and doping TiO₂ with magnesium.¹³⁰ The utilization of these design strategies in the **Co-bpm** mediator-based devices can potentially enhance the photovoltage above 1.1 V and facilitate faster photocurrent generation.

Recombination was evidently an important factor in the limited performance of **Co-bpm** mediator-based devices, but dye and mediator regeneration are known to also have profound effects on device performance.^{41,131,132} In this study, the effect of E° on dye regeneration at the anode or mediator regeneration at the cathode cannot be resolved using the presented techniques. Therefore, it is of interest to determine the contribution of dye and mediator regeneration by transient absorption and electrochemical impedance measurements because the elucidation of these electron transfer processes can provide further insights on the limitations of **Co-bpm**.^{133–136} The result is also informative in the selection of dye and cathode catalysts for future device optimization.

Finally, **Co-bpm** may find application in solid-state solar cell devices. Cobalt dopants have been successfully implemented in the hole transport materials (HTM) for solid-state DSSC^{137–139} and perovskites solar cells.^{140–143} HTM typically consists of charge conducting organic polymers or small molecules. Dopants such as Co(III) complexes are added to generate additional charge carriers and enable fast hole transport across devices by oxidizing the HTM. **Co-bpm** has a comparable E° to two commercially available cobalt dopants FK102 and FK209 and can sufficiently oxidize many HTM materials (Figure 4.1).¹⁴⁴ With a gradual shift toward solid-state DSSC in our lab, **Co-bpm** has potential use in improving HTM conductivity.

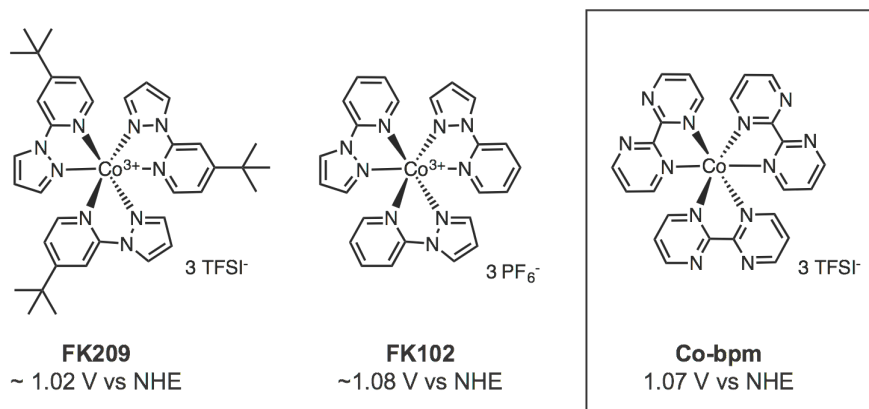


Figure 4.1 Common cobalt dopants in solid-state solar cells and the corresponding E° .¹⁴⁴ **Co-bpm** is presented for comparison.

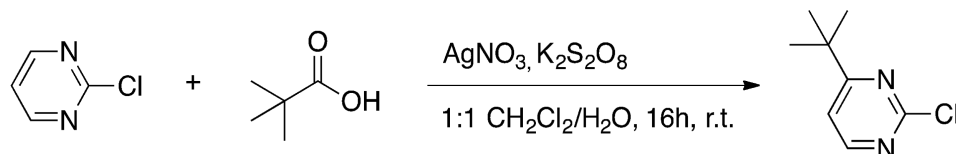
Chapter 5. Experimental

Materials. All chemicals were used as received. 2,2'-bipyrimidine (**bpm**) was purchased from Ark Pharm. Inc. 5-(4-(bis-(4-iododiphenyl)amino)phenyl)thiophene-2- cyanoacrylic acid (**Dye-I**) was synthesized according to previous literature.⁹² 2,2'-bipyridine (**bpy**), 4,4'-di-*tert*-butyl-2,2'-bipyridine (**bpy-DTB**), lithium bis(trifluoromethane)sulfonamide, 2-chloropyrimidine, silver nitrate, lithium trifluoromethanesulfonate, sodium perchlorate, sodium tetrafluoroborate, triphenylphosphine, potassium persulfate and potassium hydroxide were purchased from Sigma Aldrich. Nitrosonium hexafluorophosphate, potassium hexafluorophosphate, sodium tetraphenylborate, tetra-*n*-butylammonium hexafluorophosphate (NBu₄PF₆), titanium(IV) tetrachloride (TiCl₄), chloroplatinic acid hydrate (H₂PtCl₆), ferrocene (Fc) and chenodeoxycholic acid were purchased from Alfa Aesar. Nickel(II) chloride hexahydrate (Strem Chemicals), zinc powder (Fischer Scientific), pivalic acid (Eastman Chemical Company) were used to synthesize 4,4'-di-*tert*-butyl-2,2'-bipyrimidine (**bpm-DTB**). Silica gel was purchased from Silicycle. Dry MeOH and MeCN were obtained from solvent purification system (MBRAUN MB-SPS-800). All solvents in the solubility test were obtained from commercial sources and used as received.

Compound Characterization. NMR spectra were recorded on Bruker AV III HD 400 MHz or Bruker Avance 400dir spectrometer in deuterated solvent at 298 K. UV-Vis absorption spectra were recorded using Varian Cary 60 UV-vis spectrophotometer with a slit width of 1 nm. Measurements were carried out in MeCN in a 1 cm quartz cuvette at room temperature. Single-crystal X-ray diffraction was collected in the X-ray Crystallography facility at University of British Columbia on the Bruker X8 APEX II diffractometer using graphite monochromated MoK α ($\lambda = 0.71073$ Å) radiation. Cyclic voltammograms (CV) were collected using CHI660D

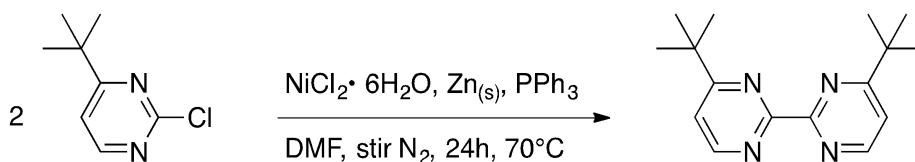
potentiostat. Measurements were taken in a solution of 0.1M (NBu₄PF₆) dissolved in dry, N₂-bubbled MeCN with Pt wire counter electrode and aqueous Ag/AgCl reference electrode. Depending on the experiment, 2 mm Pt, 2mm Au, or 3mm glassy carbon (CH Instruments, Inc.) working electrodes was used. Diffusion measurements were taken with Model AFMSRCE rotator coupled with rotating disk electrodes (Pine Research Instrumentation) and CHI920C potentiostat. Electrolyte solution was composed of 0.1M NBu₄PF₆ and a known concentration of cobalt(II) species dissolved in MeCN. Linear sweep voltammetry was performed during rotation using Pt and Au working disk electrode of 5 mm diameter (Pine Research Instrumentation), Ag/AgCl or Pt wire reference electrode, and Pt wire counter electrode.

Preparation of Compounds. The synthesis of **bpm-DTB** precursors and various complexes are described.



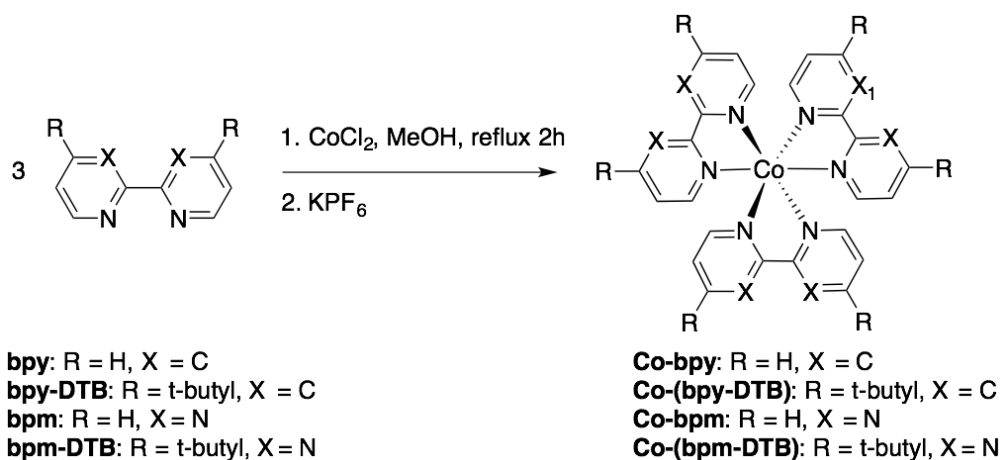
Scheme 5.1. Synthesis of 2-chloro-4-*tert*-butyl-pyrimidine.

2-chloro-4-*tert*-butyl-pyrimidine. Following a previously reported procedure,¹⁴⁵ 2-chloropyrimidine (0.67 g, 5.9 mmol), pivalic acid (0.60 g, 5.9 mmol), potassium persulfate (1.6 g, 5.9 mmol) and silver nitrate (0.20 g, 1.2 mmol) were mixed for 16h in 1:1 DCM/H₂O at room temperature in the dark. The solvent was evaporated and the residue was dissolved in ethyl acetate. The insoluble grey silver flakes were removed by washing the residue with H₂O (3 × 10 mL) via extraction, and the remaining aqueous layer further extracted with ethyl acetate (3 × 10 mL). The combined organic layer was dried with NaSO₄, and solvent was evaporated in vacuo. Purification using silica column (1:4 ethyl acetate/petroleum ether) yielded a pale yellow oil (0.48 g, 48 %). ¹H NMR (400 MHz, CD₃CN) δ 8.55 (d, *J* = 5.3 Hz, 1H), 7.43 (d, *J* = 5.3 Hz, 1H), 1.32 (s, 9H).



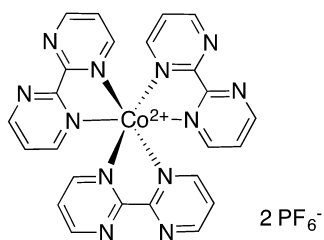
Scheme 5.2. Synthesis of 4,4'-di-*tert*-butyl-2,2'-bipyrimidine.

4,4'-di-*tert*-butyl-2,2'-bipyrimidine (bpm-DTB). Using a literature-adapted procedure,¹⁴⁶ a mixture of $\text{NiCl}_2 \cdot 6\text{H}_2\text{O}$ (1.4 g, 11 mmol), triphenylphosphine (11 g, 42 mmol), and zinc powder (1.0 g, 16 mmol) in DMF (40 mL) was degassed by performing three cycles of freeze-pump-thaw cycles and heated to 70°C under N_2 . 2-chloro-4-*tert*-butylpyrimidine was bubbled with N_2 for 1h prior to the addition to the nickel containing solution. The mixture changed from brown to black and was left to react overnight. The reaction was quenched with NH_4OH (100 mL, 4 M) for 30 min. After removing excess zinc powder from the mixture, DMF was evaporated *in vacuo*. The crude product was extracted with diethyl ether (100 mL) and washed with H_2O (1 L) to remove remaining DMF. Purification using two silica columns and 1:4 ethyl acetate/petroleum ether followed by diethyl ether removed most of the triphenylphosphine. Recrystallization in hexane yielded white crystalline product (0.82 g, 60 %) ^1H NMR (400 MHz, CDCl_3) δ 8.85 (d, $J = 5.3$ Hz, 2H), 7.40 (d, $J = 5.3$ Hz, 2H), 1.45 (s, 18H). HRMS m/z (+AP, calcd for $\text{C}_{16}\text{H}_{23}\text{N}_4^+$ m/z : 271.1923): 271.1924 $[(\text{M}+\text{H})^+]$

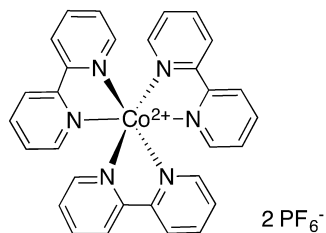


Scheme 5.3. Synthetic route of $[\text{Co-L}](\text{PF}_6)_2$ (L = coordinating diimine ligand).

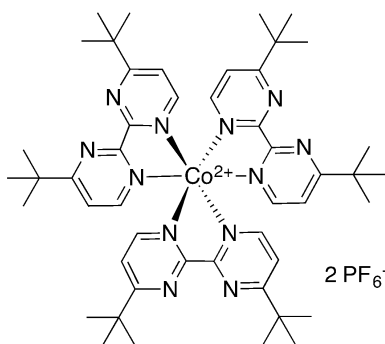
General Preparation for cobalt(II) tris(2,2'-diimine) salts. The procedure was adapted from published methods.^{43,97} Anhydrous CoCl_2 (1 equiv) and substituted 2,2'-diimine ligand (L, 3.3 equiv) were dissolved separately in dry MeOH under inert nitrogen. CoCl_2 solution was added into ligand solution dropwise, upon which the mixture slowly underwent color transition. The mixture was vigorously stirred and refluxed for 2h. Unless otherwise specified, precipitating salt (3 equiv) was added after cooling the mixture. The precipitate was isolated through vacuum filtration, rinsed minimally with cold MeOH, and dissolved in MeCN. After filtering the solution through glass frit, the solvent was removed *in vacuo* to yield the product.



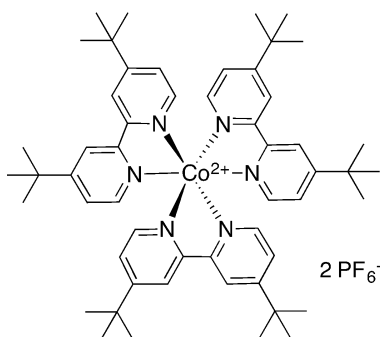
Cobalt(II) tris(2,2'-bipyrimidine) hexafluorophosphate $[\text{Co-bpm}](\text{PF}_6)_2$. Anhydrous CoCl_2 (0.027 g, 0.21 mmol) and **bpm** (0.13 g, 0.83 mmol) were reacted and precipitated with KPF_6 (0.13 g, 0.69 mmol) to yield 0.16 mg (92 %) as an orange powder. ^1H NMR (400 MHz, CD_3CN): 100.63(s, 6H), 41.02 (s, 6H), 19.55 (s, 6H).



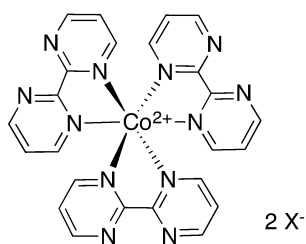
Cobalt(II) tris(2,2'-bipyridine) hexafluorophosphate [Co-bpy](PF₆)₂. Anhydrous CoCl₂ (0.16 g, 1.3 mmol) and **bpy** (0.63 g, 4.0 mmol) were reacted and precipitated with KPF₆ (1.1 g, 5.8 mmol) to yield 0.19 g (19 %) as a brown powder. ¹H NMR (400 MHz, CD₃CN): 87.80 (s, 6H), 83.80 (s, 6H), 46.00 (s, 6H), 14.50 (s, 6H).



Cobalt(II) tris(4,4'-di-*tert*-butyl-2,2'-bipyrimidine) hexafluorophosphate [Co-(bpm-DTB)](PF₆)₂. Anhydrous CoCl₂ (0.045 g, 0.35 mmol) and **bpy-DTB** (0.40 g, 1.5 mmol) were reacted in MeOH (50 mL) followed by the addition of KPF₆ (0.51 g, 2.7 mmol). The solvent was evaporated and the crude was dissolved in minimal amount of dichloromethane. The solid was precipitated upon addition of hexane, and filtered through frit. The solid was rinsed with copious amount of hexane, dissolved in dichloromethane and filtered through frit. The dried product was obtained as a pale orange powder (0.36 g, 90 % yield). ¹H NMR (400 MHz, CD₃CN) δ 90.35 (s, 6H), 80.91 (s, 6H), 43.07 (s, 6H), 3.51 (s, 54H).

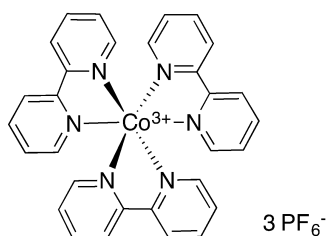


Cobalt(II) tris(4,4'-di-*tert*-butyl-2,2'-bipyridine) hexafluorophosphate [Co-(bpy-DTB)](PF₆)₂. Anhydrous CoCl₂ (0.37 g, 0.29 mmol) and **bpm-DTB** (0.25 g, 0.92 mmol) were reacted in MeOH followed by the addition of KPF₆. The crude was washed with water and diethyl ether, dissolved in MeCN and filtered through frit, and dried to yield brown powder (0.32 g, 96%). ¹H NMR (400 MHz, CD₃CN) δ 108.50 (s, 6H), 37.08 (s, 6H), 3.17 (s, 54H).

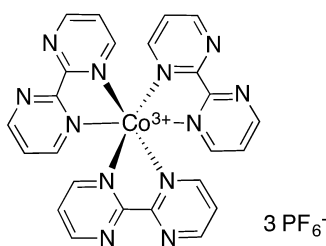


Cobalt(II) tris(2,2'-bipyrimidine) salts ([Co-bpm](X)₂), (X = ClO₄⁻, BF₄⁻, B(C₆H₅)₄⁻, OTf, TFSI⁻). The same synthetic procedure was followed as described with PF₆ salt, but the precipitating salt was replaced by NaClO₄, NaBF₄, NaB(C₆H₅)₄, or LiTFSI to obtain the corresponding [Co-bpm](X)₂. The products were orange (X = ClO₄⁻, BF₄⁻, TFSI⁻) and brown (X = B(C₆H₅)₄⁻) powders. ¹H NMR spectra is identical to that of [Co-bpm](PF₆)₂.

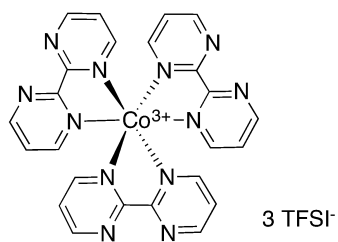
General Preparation for cobalt(III) tris(2,2'-diimine) salts. Excess NOPF_6 was dissolved in dry MeCN and corresponding tris(2,2'-diimine) cobalt(II) salt was added. The solution immediately underwent color change. Salt metathesis was performed if target compound contained a different counterion. Solid was precipitated by dropwise addition of reaction mixture into distilled water to form powder. The compound was isolated, dissolved in MeCN and filtered. The solvent was evaporated to obtain the product.



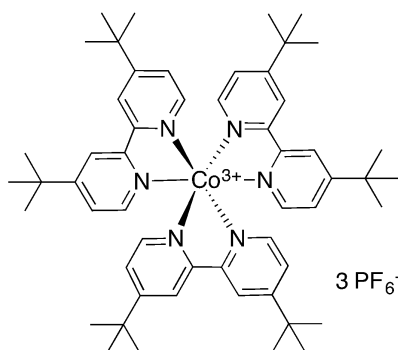
Cobalt(III) tris(2,2'-bipyridine) hexafluorophosphate $[\text{Co-bpy}](\text{PF}_6)_3$. Reaction with NOPF_6 and $[\text{Co-bpy}](\text{PF}_6)_2$ yielded yellow powder. ^1H NMR (400 MHz, CD_3CN) δ 8.73 – 8.66 (m, 6H), 8.51 – 8.43 (m, 6H), 7.73 (t, $J = 6.6$ Hz, 6H), 7.27 (d, $J = 5.7$, 6H).



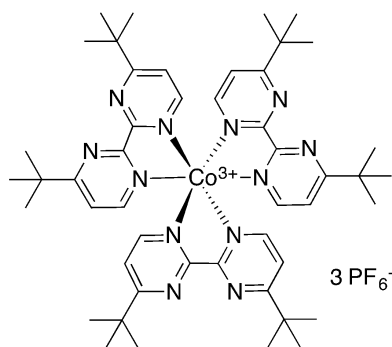
Cobalt(III) tris(2,2'-bipyrimidine) hexafluorophosphate $[\text{Co-bpm}](\text{PF}_6)_3$. Reaction with NOPF_6 and $[\text{Co-bpm}](\text{PF}_6)_2$ yielded dark orange powder. ^1H NMR (400 MHz, CD_3CN): 9.49 (dd, 6H, $J = 4.8, 1.7$ Hz, H1), 7.98 (t, 6H, $J = 5.4$ Hz, H2), 7.80 (d, 6H, $J = 6.2$ Hz, H3).



Cobalt(III) tris(2,2'-bipyrimidine) trifluoromethanesulfonimide [Co-bpm](TFSI)₃. Reaction with NOPF₆ and [Co-bpm](PF₆)₂, followed by salt metathesis with excess LiTFSI yielded orange powder. ¹H NMR (400 MHz, CD₃CN) δ 9.48 (dd, 6H, *J* = 4.8, 1.6 Hz), 7.98 – 7.91 (m, 6H), 7.76 (dd, 6H, *J* = 6.1, 1.6 Hz).



Cobalt(III) tris(4,4'-di-*tert*-butyl-2,2'-bipyridine) hexafluorophosphate [Co-(bpy-DTB)](PF₆)₃. Reaction with NOPF₆ and [Co-(bpy-DTB)](PF₆)₂ yielded yellow powder. ¹H NMR (400 MHz, CD₃CN) δ 8.63(d, *J* = 2.1 Hz, 6H), 7.67 (dd, *J* = 6.4, 2.2 Hz, 6H), 7.05 (d, *J* = 6.4 Hz, 6H), 1.45 (s, 54H).



Cobalt(III) tris(4,4'-di-*tert*-butyl-2,2'-bipyrimidine) hexafluorophosphate [Co-(bpm-DTB)](PF₆)₃. Reaction with NOPF₆ and [Co-(bpm-DTB)](PF₆)₂ yielded orange powder. ¹H NMR (400 MHz, CD₃CN) δ 7.91 (d, *J* = 6.5 Hz, 6H), 7.59 (d, *J* = 6.5 Hz, 6H), 1.50 (s, 54H).

Magnetic Susceptibility Measurements. Magnetic susceptibility was measured by the Evans method.¹⁴⁷ A sealed capillary tube filled with reference solvent was inserted into an NMR tube containing the same reference solvent and 10 mM of the Co(II) complex. The reference solvent was composed of a drop of dioxane dissolved in CD₃CN. The magnitude of dioxane signal away from 3.15 ppm indicated magnetic effect attributed to Co(II) complexes, and the frequency difference (Δf) was used to calculate the magnetic susceptibility (X_m) by simplified Evans equation (Eq. 5.1) where f is the frequency of the NMR instrument which is 400×10^6 Hz and c is the concentration of the paramagnetic complex in mol/L. Since X_m represents total magnetic susceptibility, the diamagnetic contribution (X_d) must be removed to isolate the paramagnetic component (X_p). X_d is estimated from the sum of Pascal's constant for bonds and atoms reported in literature of a paramagnetic complex.¹⁴⁸ The values are estimated to be 2.96×10^{-4} emu mol⁻¹, 5.80×10^{-4} emu mol⁻¹, 2.32×10^{-4} emu mol⁻¹, and 3.90×10^{-4} emu mol⁻¹ for **Co-bpy**, **Co-(bpy-DTB)**, **Co-bpm**, and **Co-(bpm-DTB)**, respectively.

$$X_p = X_m - X_d = \frac{3000\Delta f}{4\pi f c} - X_d \quad (5.1)$$

The effective magnetic moment (U_{eff}) is obtained using Eq. 5.2.¹⁴⁹ k_b is Boltzmann constant, N is Avogadro constant, u_B is the Bohr magneton, and T is the temperature in Kelvin.

$$U_{\text{eff}} = \sqrt{\frac{3k_b}{Nu_B^2}} \times \sqrt{TX_p} \approx \sqrt{8 \cdot TX_p} \quad (5.2)$$

The number of unpaired electrons (n) is approximated from Eq. 5.3. Experimental values of n deviate from expected value because Co(II) undergoes spin-orbit coupling and the equation only accounts for the spin magnetic moment. Low- and high-spin Co(II) typically yield U_{eff} of 1.8 and 4.4-5.2 Bohr magneton, respectively.¹²⁴ The four Co(II) complexes presented in this thesis have U_{eff} values from 4.42-4.86 Bohr magneton corresponding to high-spin configuration.

$$U_{\text{eff}} = \sqrt{n(n+2)} \quad (5.3)$$

Diffusion Measurements. Rotating disk electrode experiment is a simple and direct technique to create a diffusion-controlled environment for electron transfer. The basic principle works similarly to other potential sweeping methods where an observable current arises from oxidation or reduction of electroactive species in solution. In a stationary set-up, however, the reduced or oxidized species remain close to the electrode surface in the timescale of the measurement and therefore the current declines as more electroactive species are consumed. The measured current has dependence not only on molecular diffusion, but also random convection and migration. Rotation disk electrode controls convection and migration effects by generating a constant and predictable convection in the solution. Electroactive species are constantly replenished, and oxidized species are propelled from the surface. The result is a diffusion-limited current dependent on the rotation of the electrode (Figure 5.1). A thin layer of solution near the

electrode surface, also known as the hydrodynamic boundary layer, rotates along with electrode and appears stationary in the frame of reference. Diffusion of electroactive species through the layer is proportional the layer thickness which is related to the square-root of angular frequency of rotation (ω).

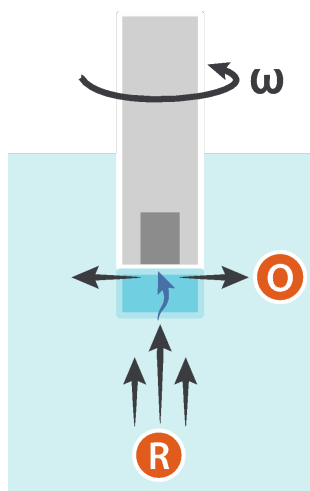


Figure 5.1. Rotating disk electrode submerged in electrolyte containing redox active species. Reduced species (R) travels toward the electrode via convection, diffuses through the hydrodynamic boundary layer (dark blue rectangle), oxidizes at the rotating electrode (dark grey) to form the oxidized species (O), and propels away by centrifugal force. The electrode rotates at a specific angular frequency of rotation (ω).

Experimentally, linear sweep voltammetry was performed while the rotation rate of the electrode varied from 100, 225, 400, 625, 900, 1225, 1600, 2025, and 2500 rpm. Measurements were performed using glassy carbon electrode on **Co-bpy** and **Co-bpm** whereas gold electrode was used for **Co-(bpy-DTB)** and Fc. The scan rate was 100 mV/s. The current increased linearly with square-root of the rotation rate. Diffusion coefficient was calculated using Koutecky-Levich equation by plotting reciprocal current versus reciprocal square-root of ω at a selected voltage. The slope is related to the diffusion coefficient by Eq. 5.4. i_k is the current from electron-transfer kinetic, n is number of electrons involved in the redox reaction, F is Faraday constant, D_{bulk} is the diffusion coefficient, ν is the kinematic viscosity of the solvent, and C is the concentration of electroactive species in solution. The kinematic viscosity in MeCN is $4.54 \times 10^{-3} \text{ cm}^2 \text{ s}^{-1}$.¹⁰³ This

equation is useful when limited-current could not be reached due to sluggish electron-transfer kinetics because the slope remains the same at voltages below the limited-current.

$$\frac{1}{i} = \frac{1}{i_k} + \left(\frac{1}{0.620nFAD_{bulk}^{2/3} \nu^{-1/6} C} \right) \omega^{-1/2} \quad (5.4)$$

Cell Fabrication. Photoanodes were prepared by screen printing a nanoparticle TiO₂ paste (18 nm nanoparticle layer using 18-NRT paste and scattering layer using WER4-O paste, Dyesol) on conductive glass coated with fluorinated tin oxide (FTO). The TiO₂ was sintered at 500 °C in the oven. The anodes of the devices presented in chapter 2 were composed of two nanoparticle layer and one scattering layer with total active area of 0.126 cm² and thickness between 12-16 μm. The anodes of the devices presented in chapter 3 were printed with one nanoparticle layer and one scattering layer with total active area of 0.196 cm² and thickness between 10-12 μm. The TiO₂ substrates were treated TiCl_{4(aq)} bath at 70 °C for 30 min, and rinsed with H₂O and EtOH. After gradual heating to 500 °C for 35 min in ambient atmosphere, the photoanodes were cooled to 80 °C and immersed in **Dye-I** (~0.1 mM) dissolved with ~1 mM chenodeoxycholic acid in MeCN for 24 h. The stained films were rinsed and immersed in MeCN for 30 min before drying in the desiccator. Cathodes were prepared by coating FTO-glass with H₂PtCl₆ (~2 mM, dissolved in ethanol), heated to 400 °C for 22 min, and maintained at 100 °C. Prior to cell fabrication, the temperature was lowered to 70 °C. The cells were assembled in home-made dry box purged with dry air. Electrodes were sealed together with 30 μm surlyn gasket (Dupont) by resistive heating. The various electrolyte formulations used in the study are described in the results and discussion section of chapter 2 and 3. The electrolyte was injected into the sandwiched electrodes through a hole in the cathode. The hole was sealed via thin surlyn film

(Dupont) and microscope coverslip (18 x 18 mm). Silver paint was coated on the electrode edges to increase conductivity for the measurements.

Cell Characterization. Photovoltaic measurements were recorded with a TriSOL solar simulator (SS1012) equipped with a class A 300 W xenon light source powered by a Newport power supply (model 69911). The light output (area = 52 mm × 52 mm) was calibrated to AM 1.5 using a Newport Oriel correction filter to reduce the spectral mismatch in the region of 350-700 nm to less than 1.5%. The power output of the lamp was measured to 1 sun (1000 Wm^{-2}) using a certified Newport Oriel Si reference cell (Model SN 679). The J-V characteristic of each cell was obtained by applying an external potential bias to the cell and measuring the generated photocurrent with a Keithley digital source meter (model 2400). SCPT was measured by applying zero bias voltage with the source meter and measure the generated photocurrent upon illumination at 1 and 0.7 sun. Acquisition time was controlled by Keithley Kickstart software under I-V characterization with the following set parameters: bias voltage = 0 V; delay = 0.01 s; NLPC = 0.1; and number of data = 500. Illumination sequence was controlled manually by starting measurement in the dark for 2s, turn on lamp for 3s, and turn off lamp for the remaining duration. OCVD was similarly measured by applying zero current bias with the source meter and measuring the decay of photovoltage in the dark following illumination at 1 and 0.7 sun. Acquisition time was controlled by Keithley Kickstart software with following set parameters: bias current = 0 A; delay = 0.0005s; NLPC = 0.1; and number of data = 2500. Illumination sequence was controlled manually by illuminating the cell for 10s and turning off the lamp for the duration of the measurement. Data acquisition initiates 2s before the lamp was turned off. All cells were placed and fixed with cellophane tape on a lab jack covered with aluminum foil, before attaching to the Keithley digital source meter.

References

- (1) IEA. *Key World Energy Statistics 2016*; OECD Publishing, 2016.
- (2) EIA - International Energy Outlook 2017 <https://www.eia.gov/outlooks/ieo/> (accessed Nov 13, 2017).
- (3) IEA. *Renewables Information 2017*; Renewables Information; OECD Publishing, 2017.
- (4) REN21. *Renewables 2017 Global Status Report*; REN21, 2017.
- (5) NOAA. Energy On a Sphere <https://sos.noaa.gov/datasets/energy-on-a-sphere/>.
- (6) IEA. *Next Generation Wind and Solar Power*; IEA, 2016.
- (7) IEA-PVPS. *PVPS Annual Report 2016*; PVPS Annual Report; IEA, 2017.
- (8) Azarpour, A.; Suhaimi, S.; Zahedi, G.; Bahadori, A. *Arab. J. Sci. Eng.* **2013**, 38 (2), 317–328.
- (9) Becquerel, A.-E. *C. R. Acad. Sci* **1839**, 9, 145–149.
- (10) Saga, T. *NPG Asia Materials* **2010**, 2 (3), 96–102.
- (11) Battaglia, C.; Cuevas, A.; De Wolf, S. *Energy Environ. Sci.* **2016**, 9 (5), 1552–1576.
- (12) Shah, A. V.; Schade, H.; Vanecek, M.; Meier, J.; Vallat-Sauvain, E.; Wyrsh, N.; Kroll, U.; Droz, C.; Bailat, J. *Prog. Photovoltaics Res. Appl.* **2004**, 12 (2-3), 113–142.
- (13) Konagai, M. *Jpn. J. Appl. Phys.* **2011**, 50 (3R), 030001.
- (14) Romeo, N.; Bosio, A.; Canevari, V.; Podestà, A. *Solar Energy* **2004**, 77 (6), 795–801.
- (15) Romeo, A.; Terheggen, M.; Abou-Ras, D.; Bätzner, D. L.; Haug, F.-J.; Kälin, M.; Rudmann, D.; Tiwari, A. N. *Prog. Photovoltaics Res. Appl.* **2004**, 12 (2-3), 93–111.
- (16) Panthani, M. G.; Akhavan, V.; Goodfellow, B.; Schmidtke, J. P.; Dunn, L.; Dodabalapur, A.; Barbara, P. F.; Korgel, B. A. *J. Am. Chem. Soc.* **2008**, 130 (49), 16770–16777.
- (17) Yang, S.; Fu, W.; Zhang, Z.; Chen, H.; Li, C.-Z. *J. Mater. Chem. A Mater. Energy Sustain.* **2017**, 5 (23), 11462–11482.
- (18) Carey, G. H.; Abdelhady, A. L.; Ning, Z.; Thon, S. M.; Bakr, O. M.; Sargent, E. H. *Chem. Rev.* **2015**, 115 (23), 12732–12763.
- (19) Hedley, G. J.; Ruseckas, A.; Samuel, I. D. W. *Chem. Rev.* **2017**, 117 (2), 796–837.
- (20) Lu, L.; Zheng, T.; Wu, Q.; Schneider, A. M.; Zhao, D.; Yu, L. *Chem. Rev.* **2015**, 115 (23), 12666–12731.
- (21) Rasheduzzaman, M.; Pillai, P. B.; Mendoza, A. N. C.; De Souza, M. M. In *Proceedings of the 10th International Symposium on Communication Systems, Networks and Digital Signal Processing*; IEEE, 2016.
- (22) O'Regan, B.; Grätzel, M. *Nature* **1991**, 353 (6346), 737–740.
- (23) Tsubomura, H.; Matsumura, M.; Nomura, Y.; Amamiya, T. *Nature* **1976**, 261 (5559), 402–403.
- (24) Matsumura, M.; Mitsuda, K.; Yoshizawa, N.; Tsubomura, H. *Bull. Chem. Soc. Jpn.* **1981**, 54 (3), 692–695.
- (25) Vlachopoulos, N.; Liska, P.; Augustynski, J.; Grätzel, M. *J. Am. Chem. Soc.* **1988**, 110 (4), 1216–1220.
- (26) Shalini, S.; Balasundaraprabhu, R.; Kumar, T. S.; Prabavathy, N.; Senthilarasu, S.; Prasanna, S. *Int. J. Energy Res.* **2016**, 40 (10), 1303–1320.
- (27) Wu, J.; Lan, Z.; Lin, J.; Huang, M.; Huang, Y.; Fan, L.; Luo, G. *Chem. Rev.* **2015**, 115 (5), 2136–2173.
- (28) Wu, J.; Lan, Z.; Lin, J.; Huang, M.; Huang, Y.; Fan, L.; Luo, G.; Lin, Y.; Xie, Y.; Wei, Y. *Chem. Soc. Rev.* **2017**, 46 (19), 5975–6023.
- (29) Jose, R.; Thavasi, V.; Ramakrishna, S. *J. Am. Ceram. Soc.* **2009**, 92 (2), 289–301.
- (30) Hagfeldt, A.; Boschloo, G.; Sun, L.; Kloo, L.; Pettersson, H. *Chem. Rev.* **2010**, 110 (11), 6595–6663.
- (31) Grätzel, M. *J. Photochem. Photobiol. C: Photochem. Rev.* **2003**, 4 (2), 145–153.
- (32) Bisquert, J.; Zaban, A.; Greenshtein, M.; Mora-Seró, I. *J. Am. Chem. Soc.* **2004**, 126 (41), 13550–13559.
- (33) O'Regan, B. C.; Durrant, J. R. *Acc. Chem. Res.* **2009**, 42 (11), 1799–1808.
- (34) Clifford, J. N.; Martínez-Ferrero, E.; Palomares, E. *J. Mater. Chem.* **2012**, 22 (25), 12415–12422.

- (35) Fisher, A. C.; Peter, L. M.; Ponomarev, E. A.; Walker, A. B.; Wijayantha, K. G. U. *J. Phys. Chem. B* **2000**, *104* (5), 949–958.
- (36) Hara, K.; Miyamoto, K.; Abe, Y.; Yanagida, M. *J. Phys. Chem. B* **2005**, *109* (50), 23776–23778.
- (37) Wang, H.; Nicholson, P. G.; Peter, L.; Zakeeruddin, S. M.; Grätzel, M. *J. Phys. Chem. C* **2010**, *114* (33), 14300–14306.
- (38) Ondersma, J. W.; Hamann, T. W. *Coord. Chem. Rev.* **2013**, *257* (9–10), 1533–1543.
- (39) Teng, C.; Yang, X.; Yuan, C.; Li, C.; Chen, R.; Tian, H.; Li, S.; Hagfeldt, A.; Sun, L. *Org. Lett.* **2009**, *11* (23), 5542–5545.
- (40) Zong, X.; Liang, M.; Chen, T.; Jia, J.; Wang, L.; Sun, Z.; Xue, S. *Chem. Commun.* **2012**, *48* (53), 6645.
- (41) Robson, K. C. D.; Hu, K.; Meyer, G. J.; Berlinguette, C. P. *J. Am. Chem. Soc.* **2013**, *135* (5), 1961–1971.
- (42) Freitag, M.; Giordano, F.; Yang, W.; Pazoki, M.; Hao, Y.; Zietz, B.; Grätzel, M.; Hagfeldt, A.; Boschloo, G. *J. Phys. Chem. C* **2016**, *120* (18), 9595–9603.
- (43) Feldt, S. M.; Wang, G.; Boschloo, G.; Hagfeldt, A. *J. Phys. Chem. C* **2011**, *115* (43), 21500–21507.
- (44) Bisquert, J.; Marcus, R. A. *Top. Curr. Chem.* **2014**, *352*, 325–395.
- (45) Feldt, S. M.; Lohse, P. W.; Kessler, F.; Nazeeruddin, M. K.; Grätzel, M.; Boschloo, G.; Hagfeldt, A. *Phys. Chem. Chem. Phys.* **2013**, *15* (19), 7087–7097.
- (46) Boschloo, G.; Hagfeldt, A. *Acc. Chem. Res.* **2009**, *42* (11), 1819–1826.
- (47) Chiba, Y.; Islam, A.; Watanabe, Y.; Komiya, R.; Koide, N.; Han, L. *Jpn. J. Appl. Phys.* **2006**, *45* (25), L638–L640.
- (48) Joly, D.; Pellejà, L.; Narbey, S.; Oswald, F.; Chiron, J.; Clifford, J. N.; Palomares, E.; Demadrille, R. *Sci. Rep.* **2015**, *4* (1).
- (49) Hamann, T. W.; Ondersma, J. W. *Energy Environ. Sci.* **2011**, *4* (2), 370–381.
- (50) Yu, Z.; Vlachopoulos, N.; Gorlov, M.; Kloo, L. *Dalton Trans. J. Inorg. Chem.* **2011**, *40* (40), 10289.
- (51) Daeneke, T.; Kwon, T.-H.; Holmes, A. B.; Duffy, N. W.; Bach, U.; Spiccia, L. *Nat. Chem.* **2011**, *3* (3), 213–217.
- (52) Rutkowska, I. A.; Andrearczyk, A.; Zoladek, S.; Goral, M.; Darowicki, K.; Kulesza, P. J. *J. Solid State Electrochem.* **2011**, *15* (11–12), 2545–2552.
- (53) Saygili, Y.; Söderberg, M.; Pellet, N.; Giordano, F.; Cao, Y.; Muñoz-García, A. B.; Zakeeruddin, S. M.; Vlachopoulos, N.; Pavone, M.; Boschloo, G.; Kavan, L.; Moser, J.-E.; Grätzel, M.; Hagfeldt, A.; Freitag, M. *J. Am. Chem. Soc.* **2016**, *138* (45), 15087–15096.
- (54) Kakiage, K.; Aoyama, Y.; Yano, T.; Oya, K.; Fujisawa, J.-I.; Hanaya, M. *Chem. Commun.* **2015**, *51* (88), 15894–15897.
- (55) Freitag, M.; Teuscher, J.; Saygili, Y.; Zhang, X.; Giordano, F.; Liska, P.; Hua, J.; Zakeeruddin, S. M.; Moser, J.-E.; Grätzel, M.; Hagfeldt, A. *Nat. Photonics* **2017**, *11* (6), 372–378.
- (56) Sun, Z.; Liang, M.; Chen, J. *Acc. Chem. Res.* **2015**, *48* (6), 1541–1550.
- (57) Aribia, K. B.; Moehl, T.; Zakeeruddin, S. M.; Grätzel, M. *Chem. Sci.* **2013**, *4* (1), 454–459.
- (58) Hagberg, D. P.; Marinado, T.; Karlsson, K. M.; Nonomura, K.; Qin, P.; Boschloo, G.; Brinck, T.; Hagfeldt, A.; Sun, L. *J. Org. Chem.* **2007**, *72* (25), 9550–9556.
- (59) Kashif, M. K.; Nippe, M.; Duffy, N. W.; Forsyth, C. M.; Chang, C. J.; Long, J. R.; Spiccia, L.; Bach, U. *Angew. Chem. Int. Ed.* **2013**, *52* (21), 5527–5531.
- (60) Freitag, M.; Yang, W.; Fredin, L. A.; D’Amario, L.; Karlsson, K. M.; Hagfeldt, A.; Boschloo, G. *Chemphyschem* **2016**, *17* (23), 3845–3852.
- (61) Sapp, S. A.; Elliott, C. M.; Contado, C.; Caramori, S.; Bignozzi, C. A. *J. Am. Chem. Soc.* **2002**, *124* (37), 11215–11222.
- (62) DeVries, M. J.; Pellin, M. J.; Hupp, J. T. *Langmuir* **2010**, *26* (11), 9082–9087.
- (63) Yum, J.-H.; Baranoff, E.; Kessler, F.; Moehl, T.; Ahmad, S.; Bessho, T.; Marchioro, A.; Ghadiri, E.; Moser, J.-E.; Yi, C.; Nazeeruddin, M. K.; Grätzel, M. *Nat. Commun.* **2012**, *3*, 631.
- (64) Ahmad, S.; Bessho, T.; Kessler, F.; Baranoff, E.; Frey, J.; Yi, C.; Grätzel, M.; Nazeeruddin, M. K. *Phys. Chem. Chem. Phys.* **2012**, *14* (30), 10631–10639.
- (65) Xu, D.; Zhang, H.; Chen, X.; Yan, F. *J. Mater. Chem. A* **2013**, *1* (38), 11933–11941.
- (66) Kirner, J. T.; Elliott, C. M. *J. Phys. Chem. C* **2015**, *119* (31), 17502–17514.

- (67) Nusbaumer, H.; Moser, J.-E.; Zakeeruddin, S. M.; Nazeeruddin, M. K.; Grätzel, M. *J. Phys. Chem. B* **2001**, *105* (43), 10461–10464.
- (68) Nusbaumer, H.; Zakeeruddin, S. M.; Moser, J.-E.; Grätzel, M. *Chem. Eur. J.* **2003**, *9* (16), 3756–3763.
- (69) Xie, Y.; Hamann, T. W. *J. Phys. Chem. Lett.* **2013**, *4* (2), 328–332.
- (70) Mengel, A. K. C.; Cho, W.; Breivogel, A.; Char, K.; Soo Kang, Y.; Heinze, K. *Eur. J. Inorg. Chem.* **2015**, *2015* (20), 3299–3306.
- (71) Lee, N. A.; Frenzel, B. A.; Rochford, J.; Hightower, S. E. *Eur. J. Inorg. Chem.* **2015**, *2015* (23), 3843–3849.
- (72) Nakade, S.; Makimoto, Y.; Kubo, W.; Kitamura, T.; Wada, Y.; Yanagida, S. *J. Phys. Chem. B* **2005**, *109* (8), 3488–3493.
- (73) Kashif, M. K.; Axelson, J. C.; Duffy, N. W.; Forsyth, C. M.; Chang, C. J.; Long, J. R.; Spiccia, L.; Bach, U. *J. Am. Chem. Soc.* **2012**, *134* (40), 16646–16653.
- (74) Klahr, B. M.; Hamann, T. W. *J. Phys. Chem. C* **2009**, *113* (31), 14040–14045.
- (75) Liu, Y.; Jennings, J. R.; Huang, Y.; Wang, Q.; Zakeeruddin, S. M.; Grätzel, M. *J. Phys. Chem. C* **2011**, *115* (38), 18847–18855.
- (76) Feldt, S. M.; Gibson, E. A.; Gabrielsson, E.; Sun, L.; Boschloo, G.; Hagfeldt, A. *J. Am. Chem. Soc.* **2010**, *132* (46), 16714–16724.
- (77) Yella, A.; Lee, H.-W.; Tsao, H. N.; Yi, C.; Chandiran, A. K.; Nazeeruddin, M. K.; Diau, E. W.-G.; Yeh, C.-Y.; Zakeeruddin, S. M.; Grätzel, M. *Science* **2011**, *334* (6056), 629–634.
- (78) Mathew, S.; Yella, A.; Gao, P.; Humphry-Baker, R.; Curchod, B. F. E.; Ashari-Astani, N.; Tavernelli, I.; Rothlisberger, U.; Nazeeruddin, M. K.; Grätzel, M. *Nat. Chem.* **2014**, *6* (3), 242–247.
- (79) Zong, X.; Liang, M.; Fan, C.; Tang, K.; Li, G.; Sun, Z.; Xue, S. *J. Phys. Chem. C* **2012**, *116* (20), 11241–11250.
- (80) Chen, C.; Yang, X.; Cheng, M.; Zhang, F.; Zhao, J.; Sun, L. *ACS Appl. Mater. Interfaces* **2013**, *5* (21), 10960–10965.
- (81) Wu, K.-L.; Huckaba, A. J.; Clifford, J. N.; Yang, Y.-W.; Yella, A.; Palomares, E.; Grätzel, M.; Chi, Y.; Nazeeruddin, M. K. *Inorg. Chem.* **2016**, *55* (15), 7388–7395.
- (82) Yum, J.-H.; Moehl, T.; Yoon, J.; Chandiran, A. K.; Kessler, F.; Gratia, P.; Grätzel, M. *J. Phys. Chem. C* **2014**, *118* (30), 16799–16805.
- (83) Chandiran, A. K.; Tetreault, N.; Humphry-Baker, R.; Kessler, F.; Baranoff, E.; Yi, C.; Nazeeruddin, M. K.; Grätzel, M. *Nano Lett.* **2012**, *12* (8), 3941–3947.
- (84) Nelson, J. J.; Amick, T. J.; Elliott, C. M. *J. Phys. Chem. C* **2008**, *112* (46), 18255–18263.
- (85) Trang Pham, T. T.; Koh, T. M.; Nonomura, K.; Lam, Y. M.; Mathews, N.; Mhaisalkar, S. *Chemphyschem* **2014**, *15* (6), 1216–1221.
- (86) Mosconi, E.; Yum, J.-H.; Kessler, F.; Gómez García, C. J.; Zuccaccia, C.; Cinti, A.; Nazeeruddin, M. K.; Grätzel, M.; De Angelis, F. *J. Am. Chem. Soc.* **2012**, *134* (47), 19438–19453.
- (87) Xie, Y.; Baillargeon, J.; Hamann, T. W. *J. Phys. Chem. C* **2015**, *119* (50), 28155–28166.
- (88) Salvatori, P.; Marotta, G.; Cinti, A.; Mosconi, E.; Panigrahi, M.; Giribabu, L.; Nazeeruddin, M. K.; De Angelis, F. *Inorg. Chim. Acta* **2013**, *406*, 106–112.
- (89) Marcus, R. A. *J. Chem. Phys.* **1956**, *24* (5), 966–978.
- (90) Mishra, A.; Fischer, M. K. R.; Bäuerle, P. *Angew. Chem. Int. Ed.* **2009**, *48* (14), 2474–2499.
- (91) Clifford, J. N.; Martínez-Ferrero, E.; Viterisi, A.; Palomares, E. *Chem. Soc. Rev.* **2011**, *40* (3), 1635–1646.
- (92) Swords, W. B.; Simon, S. J. C.; Parlange, F. G. L.; Dean, R. K.; Kellett, C. W.; Hu, K.; Meyer, G. J.; Berlinguette, C. P. *Angew. Chem. Int. Ed.* **2016**, *55* (20), 5956–5960.
- (93) Gregg, B. A.; Pichot, F.; Ferrere, S.; Fields, C. L. *J. Phys. Chem. B* **2001**, *105* (7), 1422–1429.
- (94) Kim, J.-Y.; Lee, K. J.; Kang, S. H.; Shin, J.; Sung, Y.-E. *J. Phys. Chem. C* **2011**, *115* (40), 19979–19985.
- (95) Yella, A.; Mathew, S.; Aghazada, S.; Comte, P.; Grätzel, M.; Nazeeruddin, M. K. *J. Mater. Chem.* **2017**, *5* (11), 2833–2843.
- (96) Zaban, A.; Greenshtein, M.; Bisquert, J. *Chemphyschem* **2003**, *4* (8), 859–864.
- (97) Ruminski, R. R.; Petersen, J. D. *Inorg. Chim. Acta* **1984**, *88* (1), 63–66.
- (98) Sun, Z.-Z.; Zheng, K.-M.; Li, Q.-S.; Li, Z.-S. *RSC Adv.* **2014**, *4* (60), 31544–31551.

- (99) Rillema, D. P.; Allen, G.; Meyer, T. J.; Conrad, D. *Inorg. Chem.* **1983**, 22 (11), 1617–1622.
- (100) Kawanishi, Y.; Kitamura, N.; Tazuke, S. *Inorg. Chem.* **1989**, 28 (15), 2968–2975.
- (101) Copley, G.; Hwang, D.; Kim, D.; Osuka, A. *Angew. Chem. Int. Ed.* **2016**, 55 (35), 10287–10291.
- (102) Krivokapic, I.; Zerara, M.; Daku, M. L.; Vargas, A.; Enachescu, C.; Ambrus, C.; Tregenna-Piggott, P.; Amstutz, N.; Krausz, E.; Hauser, A. *Coord. Chem. Rev.* **2007**, 251 (3–4), 364–378.
- (103) Bard, A. J.; Faulkner, L. R. *Electrochemical methods: fundamentals and applications*, 2nd ed.; Wiley: New York, 2001.
- (104) Salim, N. T.; Yang, X.; Zhang, S.; Liu, J.; Islam, A.; Han, L. *J. Mater. Chem. A* **2014**, 2 (27), 10532–10539.
- (105) Boschloo, G.; Häggman, L.; Hagfeldt, A. *J. Phys. Chem. B* **2006**, 110 (26), 13144–13150.
- (106) Simon, S. J. C.; Parlane, F. G. L.; Swords, W. B.; Kellett, C. W.; Du, C.; Lam, B.; Dean, R. K.; Hu, K.; Meyer, G. J.; Berlinguette, C. P. *J. Am. Chem. Soc.* **2016**, 138 (33), 10406–10409.
- (107) Fukui, A.; Komiya, R.; Yamanaka, R.; Islam, A.; Han, L. *Sol. Energy Mater. Sol. Cells* **2006**, 90 (5), 649–658.
- (108) Wu, J.; Lan, Z.; Lin, J.; Huang, M.; Li, P. *J. Power Sources* **2007**, 173 (1), 585–591.
- (109) Nia, N. Y.; Farahani, P.; Sabzyan, H.; Zendehehdel, M.; Oftadeh, M. *Phys. Chem. Chem. Phys.* **2014**, 16 (23), 11481–11491.
- (110) Davies, J. A. *Synthetic Coordination Chemistry: Principles and Practice*; World Scientific, 1996.
- (111) David, S. E.; Timmins, P.; Conway, B. R. *Drug Dev. Ind. Pharm.* **2012**, 38 (1), 93–103.
- (112) Yum, J.-H.; Holcombe, T. W.; Kim, Y.; Rakstys, K.; Moehl, T.; Teuscher, J.; Delcamp, J. H.; Nazeeruddin, M. K.; Grätzel, M. *Sci. Rep.* **2013**, 3 (1).
- (113) Ashbrook, L. N.; Elliott, C. M. *J. Phys. Chem. C* **2014**, 118 (30), 16643–16650.
- (114) Tress, W.; Petrich, A.; Hummert, M.; Hein, M.; Leo, K.; Riede, M. *Appl. Phys. Lett.* **2011**, 98 (6), 063301.
- (115) Hu, L.; Mandelis, A.; Lan, X.; Melnikov, A.; Hoogland, S.; Sargent, E. H. *Sol. Energy Mater. Sol. Cells* **2016**, 155, 155–165.
- (116) Lellig, P.; Niedermeier, M. A.; Rawolle, M.; Meister, M.; Laquai, F.; Müller-Buschbaum, P.; Gutmann, J. S. *Phys. Chem. Chem. Phys.* **2012**, 14 (5), 1607–1613.
- (117) Sundqvist, A.; Sandberg, O. J.; Nyman, M.; Smått, J.-H.; Österbacka, R. *Adv. Energy Mater.* **2016**, 6 (6), 1502265.
- (118) Safdari, M.; Lohse, P. W.; Häggman, L.; Frykstrand, S.; Högberg, D.; Rutland, M.; Asencio, R. A.; Gardner, J.; Kloo, L.; Hagfeldt, A.; Boschloo, G. *RSC Adv.* **2016**, 6 (61), 56580–56588.
- (119) Miller, J. R.; Beitz, J. V.; Huddleston, R. K. *J. Am. Chem. Soc.* **1984**, 106 (18), 5057–5068.
- (120) Memming, R. In *Semiconductor Electrochemistry*; Wiley-VCH Verlag GmbH & Co. KGaA: Weinheim, Germany, 2015; pp 127–168.
- (121) Menteş, A.; Singh, K. *Acta Crystallogr. Sect. E Struct. Rep. Online* **2013**, 69 (1), m58–m58.
- (122) England, J.; Bill, E.; Weyhermüller, T.; Neese, F.; Atanasov, M.; Wieghardt, K. *Inorg. Chem.* **2015**, 54 (24), 12002–12018.
- (123) Wang, Y.; Rogers, E. I.; Compton, R. G. *J. Electroanal. Chem.* **2010**, 648 (1), 15–19.
- (124) Figgis, B. N. *Nature* **1958**, 182 (4649), 1568–1570.
- (125) Braterman, P. S.; Song, J. I.; Peacock, R. D. *Inorg. Chem.* **1992**, 31 (4), 555–559.
- (126) Kao, M. C.; Chen, H. Z.; Young, S. L.; Kung, C. Y.; Lin, C. C. *Thin Solid Films* **2009**, 517 (17), 5096–5099.
- (127) Kim, D. H.; Woodroof, M.; Lee, K.; Parsons, G. N. *ChemSusChem* **2013**, 6 (6), 1014–1020.
- (128) Chandiran, A. K.; Nazeeruddin, M. K.; Grätzel, M. *Adv. Funct. Mater.* **2014**, 24 (11), 1615–1623.
- (129) Li, L.; Xu, C.; Zhao, Y.; Chen, S.; Ziegler, K. J. *ACS Appl. Mater. Interfaces* **2015**, 7 (23), 12824–12831.
- (130) Kakiage, K.; Osada, H.; Aoyama, Y.; Yano, T.; Oya, K.; Iwamoto, S.; Fujisawa, J.-I.; Hanaya, M. *Sci. Rep.* **2016**, 6, 35888.
- (131) Daeneke, T.; Mozer, A. J.; Uemura, Y.; Makuta, S.; Fekete, M.; Tachibana, Y.; Koumura, N.; Bach, U.; Spiccia, L. *J. Am. Chem. Soc.* **2012**, 134 (41), 16925–16928.
- (132) Tsao, H. N.; Burschka, J.; Yi, C.; Kessler, F.; Nazeeruddin, M. K.; Grätzel, M. *Energy Environ. Sci.* **2011**, 4 (12), 4921–4924.
- (133) Ondersma, J. W.; Hamann, T. W. *J. Phys. Chem. C* **2010**, 114 (1), 638–645.

- (134) Li, F.; Jennings, J. R.; Wang, Q. *ACS Nano* **2013**, 7 (9), 8233–8242.
- (135) Sacco, A. *Renewable Sustainable Energy Rev.* **2017**, 79, 814–829.
- (136) Pazoki, M.; Cappel, U. B.; Johansson, E. M. J.; Hagfeldt, A.; Boschloo, G. *Energy Environ. Sci.* **2017**, 10 (3), 672–709.
- (137) Burschka, J.; Dualeh, A.; Kessler, F.; Baranoff, E.; Cevey-Ha, N.-L.; Yi, C.; Nazeeruddin, M. K.; Grätzel, M. *J. Am. Chem. Soc.* **2011**, 133 (45), 18042–18045.
- (138) Dualeh, A.; De Angelis, F.; Fantacci, S.; Moehl, T.; Yi, C.; Kessler, F.; Baranoff, E.; Nazeeruddin, M. K.; Grätzel, M. *J. Phys. Chem. C* **2012**, 116 (1), 1572–1578.
- (139) Dualeh, A.; Moehl, T.; Nazeeruddin, M. K.; Grätzel, M. *ACS Nano* **2013**, 7 (3), 2292–2301.
- (140) Li, H.; Fu, K.; Hagfeldt, A.; Grätzel, M.; Mhaisalkar, S. G.; Grimsdale, A. C. *Angew. Chem. Int. Ed.* **2014**, 53 (16), 4085–4088.
- (141) Koh, T. M.; Dharani, S.; Li, H.; Prabhakar, R. R.; Mathews, N.; Grimsdale, A. C.; Mhaisalkar, S. *G. ChemSusChem* **2014**, 7 (7), 1909–1914.
- (142) Zhou, H.; Chen, Q.; Li, G.; Luo, S.; Song, T.-B.; Duan, H.-S.; Hong, Z.; You, J.; Liu, Y.; Yang, Y. *Science* **2014**, 345 (6196), 542–546.
- (143) Saliba, M.; Orlandi, S.; Matsui, T.; Aghazada, S.; Cavazzini, M.; Correa-Baena, J.-P.; Gao, P.; Scopelliti, R.; Mosconi, E.; Dahmen, K.-H.; De Angelis, F.; Abate, A.; Hagfeldt, A.; Pozzi, G.; Grätzel, M.; Nazeeruddin, M. K. *Nature Energy* **2016**, 1 (2), 15017.
- (144) Burschka, J.; Kessler, F.; Nazeeruddin, M. K.; Grätzel, M. *Chem. Mater.* **2013**, 25 (15), 2986–2990.
- (145) Mai, W.-P.; Sun, B.; You, L.-Q.; Yang, L.-R.; Mao, P.; Yuan, J.-W.; Xiao, Y.-M.; Qu, L.-B. *Org. Biomol. Chem.* **2015**, 13 (9), 2750–2755.
- (146) Nasielski, J.; Standaert, A.; Nasielski-Hinkens, R. *Synth. Commun.* **1991**, 21 (7), 901–906.
- (147) Evans, D. F. *J. Chem. Soc.* **1959**, 2003.
- (148) Bain, G. A.; Berry, J. F. *J. Chem. Educ.* **2008**, 85 (4), 532.
- (149) Hoppe, J. I. *J. Chem. Educ.* **1972**, 49 (7), 505.

Appendix

Table A.1. Crystallographic Data for [Co-bpm](PF₆)₂

Chemical formula	C ₂₆ H ₂₁ CoN ₁₃ F ₁₂ P ₂	Formula weight	864.43
a	10.5717(6) Å	Space group	<i>P</i> -1 (#2)
b	11.7075(7) Å	T	-173 °C
c	14.1419(8) Å	λ	0.71073 Å
α, β, γ	74.819(2)°, 81.5632 °, 75.111(2) °	D _{calcd}	1.765 g/cm ³
V	1626.59(16) Å ³	μ	7.40 cm ⁻¹
Z	2	R ₁ ^a ; wR ₂ (I>2.00σ(I)) ^b	0.046; 0.115
		R ₁ ^a ; wR ₂ (all data) ^b	0.059; 0.121

$$^a R_1 = \sum ||F_o| - |F_c|| / \sum |F_o|, \quad ^b wR_2 = [\sum (w(F_o^2 - F_c^2)^2) / \sum (w(F_o^2)^2)]^{1/2}$$

Table A.2. Selected Bond Lengths [\AA] and Angles [$^\circ$] for **[Co-bpm](PF₆)₂**

Atom	Atom	Bond length	
		\AA	
Co1	N1	2.1281(18)	
Co1	N3	2.1212(17)	
Co1	N5	2.1494(18)	
Co1	N7	2.1486(18)	
Co1	N9	2.1210(18)	
Co1	N11	2.1330(18)	
Atom	Atom	Atom	Bond angle
			$^\circ$
N1	Co1	N5	97.77(7)
N1	Co1	N7	170.53(7)
N1	Co1	N11	95.51(7)
N3	Co1	N1	76.65(7)
N3	Co1	N5	90.42(7)
N3	Co1	N7	95.71(7)
N3	Co1	N11	98.29(7)
N7	Co1	N5	76.46(7)
N9	Co1	N1	97.21(7)
N9	Co1	N3	171.91(7)
N9	Co1	N5	95.68(7)
N9	Co1	N7	90.88(7)
N9	Co1	N11	76.86(7)
N11	Co1	N5	165.50(7)
N11	Co1	N7	91.09(7)

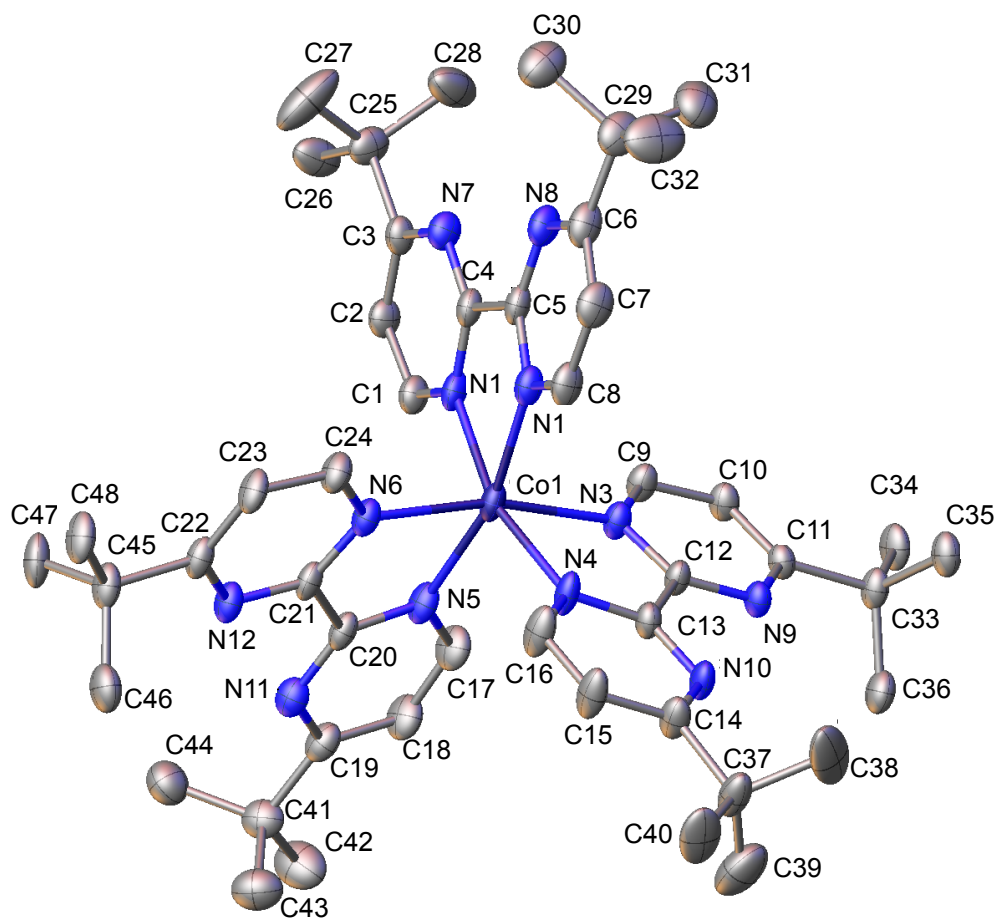


Figure A.1. Thermal ellipsoid plot of **Co-(bpm-DTB)** drawn at the 50% probability level

Table A.3. Crystallographic Data for **[Co-(bpm-DTB)](PF₆)₂**

Chemical formula	C ₅₄ H ₇₅ CoN ₁₅ F ₁₂ P ₂	Formula weight	1279.05
a	10.9787(11) Å	Space group	P2 ₁ /n (#14)
b	21.384(3) Å	T	-173 °C
c	28.322(3) Å	λ	0.71073 Å
α, β, γ	90°, 99.957(5)°, 90°	D _{calcd}	1.297 g/cm ³
V	6551.1(13) Å ³	μ	3.91 cm ⁻¹
Z	4	R ₁ ^a ; wR ₂ (I>2.00σ(I)) ^b	0.0593; 0.1158
		R ₁ ^a ; wR ₂ (all data) ^b	0.0770; 0.1215

$$^a R_1 = \sum ||F_o| - |F_c|| / \sum |F_o|, \quad ^b wR_2 = [\sum (w(F_o^2 - F_c^2)^2) / \sum (w(F_o^2)^2)]^{1/2}$$

Table A.4. Selected Bond Lengths [\AA] and Angles [$^\circ$] for **[Co-(bpm-DTB)]**(PF₆)₂

Atom	Atom	Bond length	
		\AA	
Co1	N1	2.126(3)	
Co1	N2	2.149(3)	
Co1	N3	2.158(3)	
Co1	N4	2.127(3)	
Co1	N5	2.147(3)	
Co1	N6	2.158(3)	
Atom	Atom	Atom	Bond angle
			$^\circ$
N1	Co1	N2	76.48(10)
N1	Co1	N3	92.10(10)
N1	Co1	N4	163.78(11)
N1	Co1	N5	95.86(11)
N1	Co1	N6	97.29(10)
N2	Co1	N3	99.64(10)
N2	Co1	N6	92.00(10)
N3	Co1	N6	166.50(11)
N4	Co1	N2	93.87(11)
N4	Co1	N3	76.49(10)
N4	Co1	N5	96.22(11)
N4	Co1	N6	96.04(10)
N5	Co1	N2	165.38(7)
N5	Co1	N3	93.00(17)
N5	Co1	N6	76.46(7)

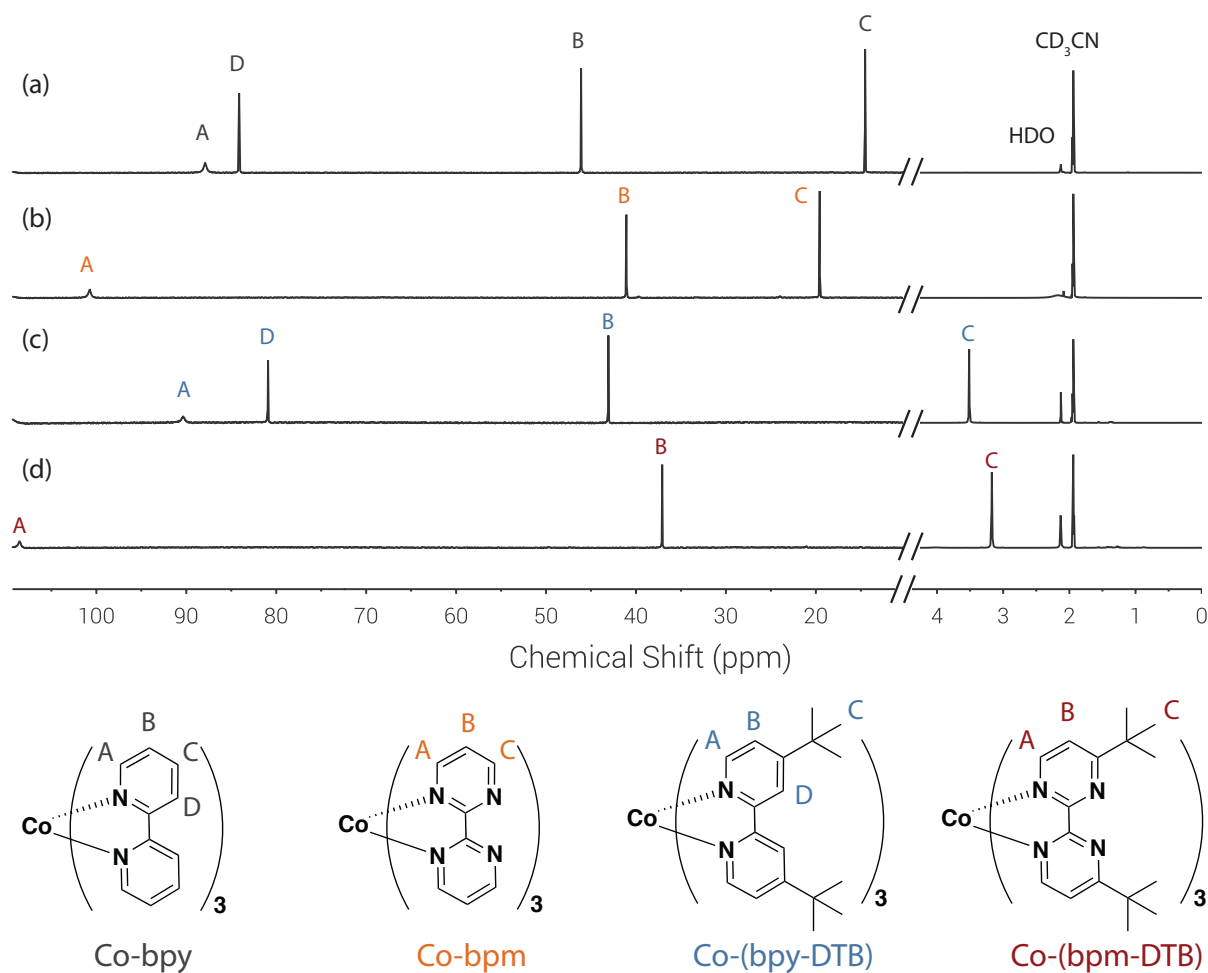
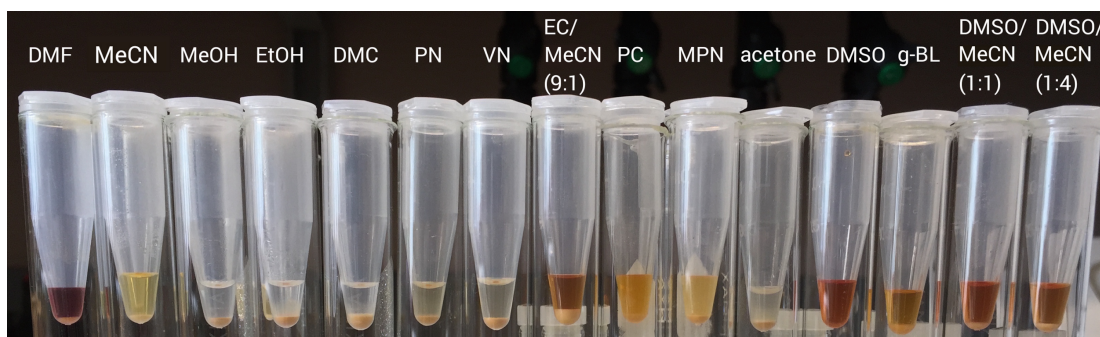


Figure A.2 ^1H NMR spectra of (a) $[\text{Co-bpy}](\text{PF}_6)_2$, (b) $[\text{Co-bpm}](\text{PF}_6)_2$, (c) $[\text{Co-(bpy-DTB)}](\text{PF}_6)_2$, and (d) $[\text{Co-(bpm-DTB)}](\text{PF}_6)_2$. Peaks assigned to the letters A-D correspond to protons on the chemical structures shown below the spectra.

Table A.5. UV-vis Absorption of **Co-bpy**, **Co-bpm**, **Co-(bpy-DTB)**, and **Co-(bpm-DTB)** in MeCN

Compound	$\lambda_{\text{max}1}/\text{nm}$ ($\epsilon/\text{M}^{-1}\text{cm}^{-1}$)	$\lambda_{\text{max}2}/\text{nm}$ ($\epsilon/\text{M}^{-1}\text{cm}^{-1}$)	$\lambda_{\text{max}3}/\text{nm}$ ($\epsilon/\text{M}^{-1}\text{cm}^{-1}$)	$\lambda_{\text{max}4}/\text{nm}$ ($\epsilon/\text{M}^{-1}\text{cm}^{-1}$)	$\lambda_{\text{max}5}/\text{nm}$ ($\epsilon/\text{M}^{-1}\text{cm}^{-1}$)
Co-bpy	245 (2.49×10^4)	295 (2.96×10^4)	305 (2.81×10^4)	440 (1.1×10^2)	901 (6.7)
Co-bpm	243 (4.72×10^4)	-	-	465 (55)	935 (7.5)
Co-(bpy-DTB)	248 (3.51×10^4)	294 (3.91×10^4)	302 (3.71×10^4)	440 (1.5×10^2)	906 (8.8)
Co-(bpm-DTB)	248 (4.78×10^4)	-	-	450 (51)	935 (8.0)

Table A.6. Approximated Saturation Concentration of [Co-bpm](PF₆)₂ in Different Solvents.



Solvents	approximate saturation concentration of [Co-bpm](PF ₆) ₂			
	0.05 M	0.10 M	0.15 M	0.20 M
acetone				
acetonitrile (MeCN)				
dimethyl carbonate (DMC)				
DMF				
DMSO				
1:1 DMSO/MeCN				
1:4 DMSO/MeCN				
ethanol (EtOH)				
9:1 ethylene carbonate (EC)/MeCN				
γ-butyrolactone (g-BL)				
methanol (MeOH)				
3-methoxypropionitrile (MPN)				
propionitrile (PN)				
propylene carbonate (PC)				
pyridine				
THF				
valeronitrile (VN)				
water				



insoluble



partially soluble



fully soluble

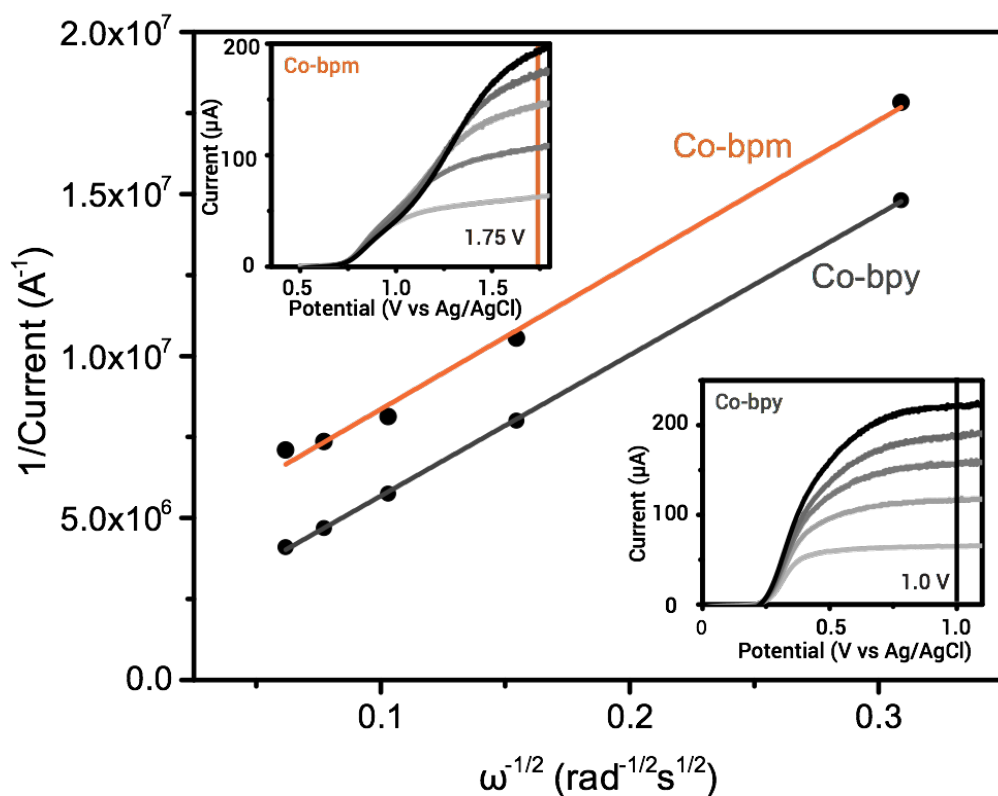


Figure A.3. Koutecky-Levich plot of **Co-bpy** and **Co-bpm** with insets showing the linear sweep voltammetry (LSV) traces. The scan rate was 100 mV/s. The three-electrode system used in the measurement consists of Ag/AgCl reference electrode, rotating GC working electrode, and Pt counter electrode in 0.1 M NBu_4PF_6 dissolved in MeCN. The vertical line in the LSV plot indicates the potential at which the current is taken to construct the Koutecky-Levich plot.

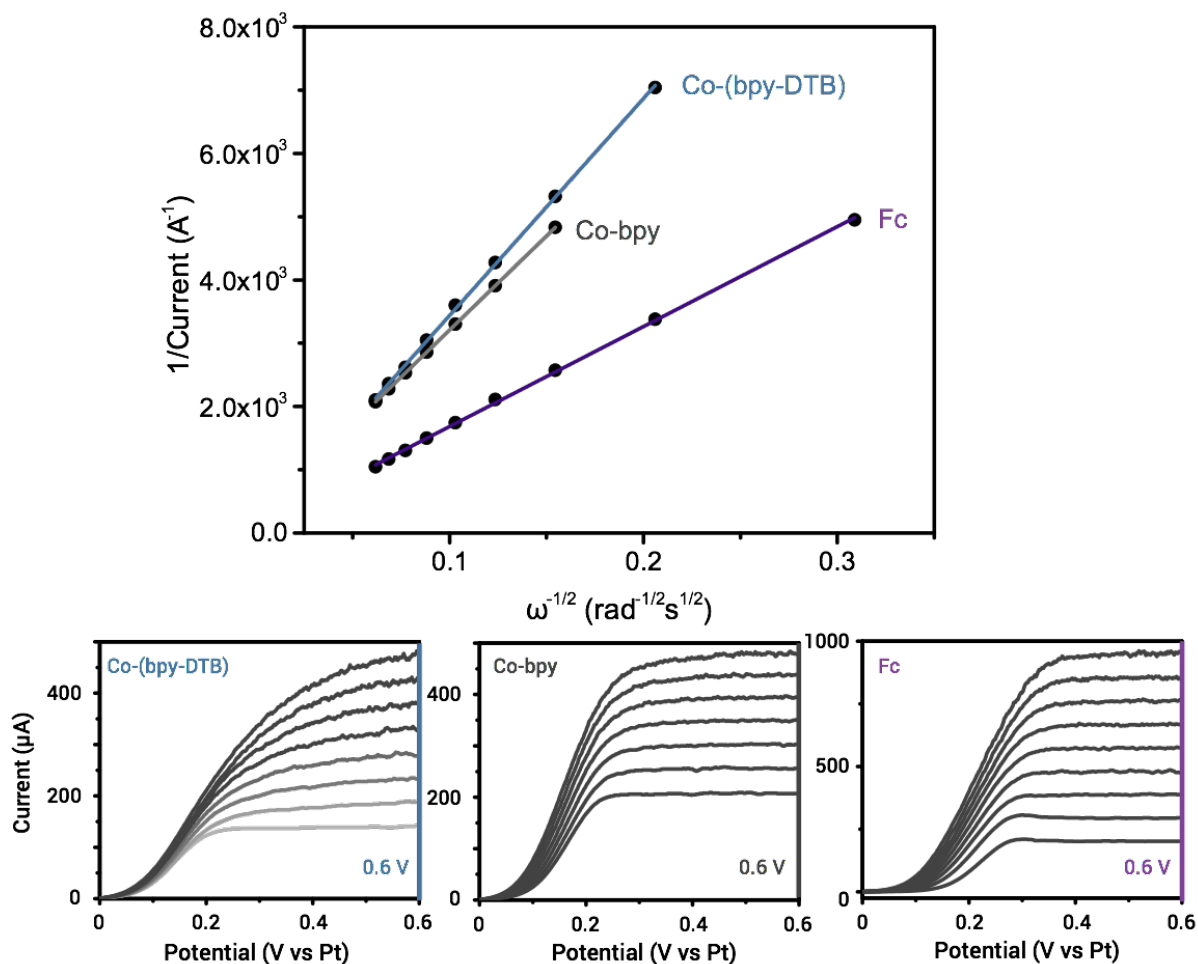
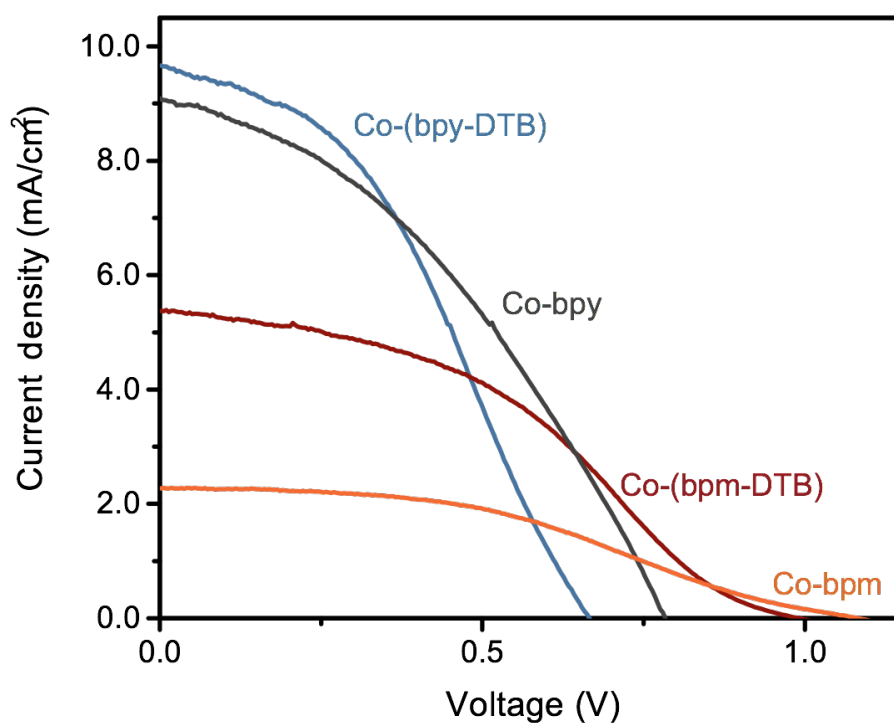


Figure A.4. (top) Koutecky-Levich plot and (bottom) linear sweep voltammetry traces of **Co-(bpy-DTB)**, **Co-bpy**, and **Fc**. The scan rate was 100 mV/s. The three-electrode system used in the measurement consists of Pt quasi-reference electrode, rotating GC working electrode, and Pt counter electrode in 0.1 M NBu_4PF_6 dissolved in MeCN. The vertical line in the LSV plot indicates the potential at which the current is taken to construct the Koutecky-Levich plot.

Table A.7. DSSC Data at Different **Co^{II}-bpm** Concentrations and in Different Solvents

Solvent	Conc.	PCE	V _{oc}	J _{sc}	FF
	M	%	V	mA cm ⁻²	
MeCN	0.025	0.047	0.9016	0.200	0.2591
PC	0.05	0.125	0.9799	0.493	0.2641
g-BL	0.05	0.247	0.9709	1.071	0.2426
1:1 DMSO/MeCN	0.1	0.279	1.02	1.064	0.2665
1:1 DMSO/MeCN	0.15	0.284	0.9769	0.949	0.3004
9:1 EC/MeCN	0.15	0.105	0.9413	0.503	0.2312
DMSO	0.2	0.141	0.9939	0.328	0.4413

**Figure A.5.** J-V curve of best performing cell devices with cobalt mediator (**Co-bpy-DTB**) (blue), **Co-bpy** (grey), **Co-bpm-DTB** (red), and **Co-bpm** (orange). The corresponding data is tabulated in Table 3.3.

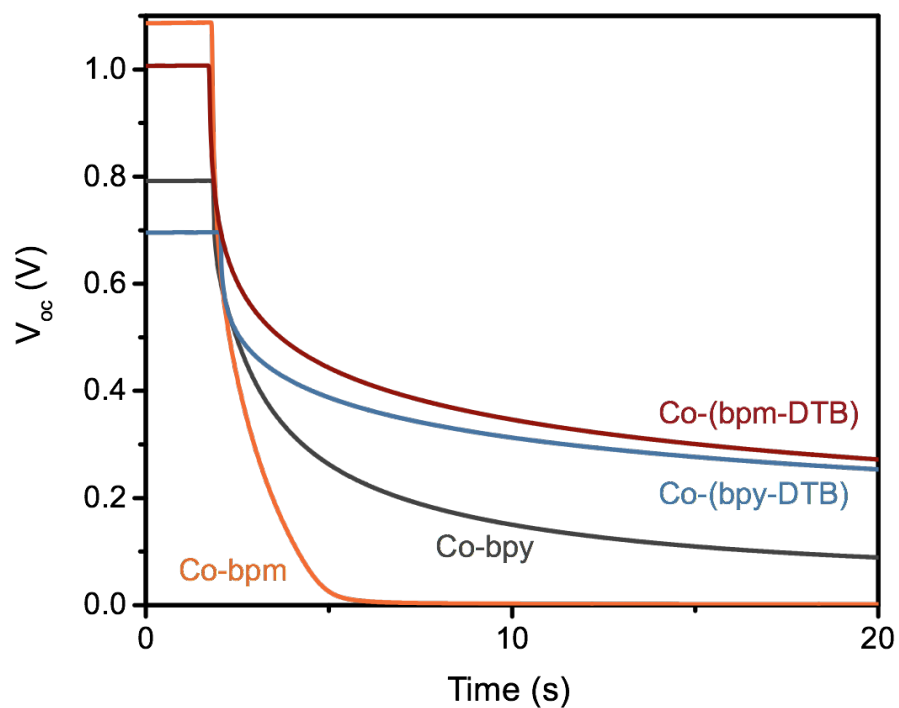


Figure A.6. OCVD decay curve measured in devices containing **Co-bpm** (orange), **Co-bpy** (grey), **Co-(bpm-DTB)** (red) and **Co-(bpy-DTB)** (blue).